UiO : Department of Chemistry
University of Oslo

Alkali and Alkaline Earth Oxoacid Salts; Synthesis, Hydration, Stability, and Electrical Conductivity

Aleksander Andestad Elstad

Thesis for the degree of '**Master of Science**', Spring 2017

Summary

Proton-conducting electrolytes are sough after for use in various applications within the field of electrochemistry. Pure and high proton conductivity has been found in many perovskite-type oxides like $BaZrO_3$ (BZY) and $BaCeO_3$, with $BaCeO_3$-based materials being among the best proton-conducting oxides. In the intermediate temperature range of 400 to $800\,^{\circ}\mathrm{C}$, BZY has been established as one of the most promising materials, exhibiting a protonic conductivity higher than $1 \times 10^{-2}\,\mathrm{S\,cm^{-1}}$ over the whole temperature range. However, it is difficult to process, and the resulting materials are usually grainy and possess highly resistive grain-boundaries [1]. For low-temperature regions, compounds like $CsHSO_4$ and CsH_2PO_4 show great potential with respect to protonic conductivity, even displaying superprotonic transitions that immensely increase their conductivity, however their stability is lacking with respect to temperature and solubility in water [2].

With this project, the aim is to broaden the horizon and investigate compounds that fall outside the common perovskite-definition. In this work, various solid acids (E.g. $KBaPO_4$, $NaCaHSiO_4$ and BaH_2SiO_4), in which the cations are alkali and alkaline earth metals and the anionic groups are separated XO_4 tetrahedra, are synthesized and subsequently characterized by X-Ray Diffraction (XRD), Thermogravimetric Analysis (TG), as well as electrical characterization by Impedance Spectroscopy (IS). The work on $KBaPO_4$ culminated in a submitted paper [3].

$KBaPO_4$ has been proposed to transform into a great protonic conductor upon hydration at low temperatures. Effectively, hydration through steam at $80\,^{\circ}\mathrm{C}$ is said to give the compound a protonic conductivity of $1 \times 10^{-2}\,\mathrm{S\,cm^{-1}}$ just below $100\,^{\circ}\mathrm{C}$ [4]. This is a remarkable result and, if it can be reproduced, it can become a viable rival to BZY. For this reason, $KBaPO_4$ was chosen as a topic for this work. Here, we synthesize $KBaPO_4$ through a high-temperature solid state reaction, and subsequently characterize the system with respect to thermal stability and its inherent electrical conductivity. Through electrical measurements, we found that the conductivity of pure $KBaPO_4$ was very low, around $2 \times 10^{-6}\,\mathrm{S\,cm^{-1}}$ at $600\,^{\circ}\mathrm{C}$, with an activation energy exceeding $1\,\mathrm{eV}$. The compound is indifferent to the presence of humidity, and results indicate that the charge carrier in the compound is not protonic, but rather it is theorized to be potassium ions, with potassium Frenkel defects being the predominating defect, however this has not been explicitly confirmed. All in all, we propose a defect model for $KBaPO_4$ with Frenkel defects as the predominating defects.

Through attempts at hydrating $KBaPO_4$ in accordance to the method proposed by Goodenough, we found that it does not transform into a high-conductivity phase, but rather decomposes into potassium doped $Ba_3(PO_4)_2$, and that the resulting system shows similar

properties, such as thermal stability (Decomposing at $300\,^{\circ}\mathrm{C}$) and protonic conductivity ($1.6 \times 10^{-6}\,\mathrm{S\,cm^{-1}}$ at $250\,^{\circ}\mathrm{C}$), to the system $Ba_{3-x}K_xH_x(PO_4)_2$ previously investigated by Haile et al. [5], albeit with a significantly lower potassium content than the systems they have characterized, possibly indicating that a saturation of K in $Ba_3(PO_4)_2$ has been reached.

By subsequently heating $Ba_{3-x}K_xH_x(PO_4)_2$ to high temperatures, the system is found to expel potassium and form a two-phase system of $Ba_3(PO_4)_2$ and a secondary phase of $KBaPO_4$, showing similarities to the system $Ba_{3(1-x)}K_{3x}(PO_4)_{2-x}$ previously investigated by Iwahara et al. [6]. Through impedance spectroscopy of said system, we found evidence that points toward the system being a protonic conductor, with a bulk conductivity slightly higher than $1 \times 10^{-3}\,\mathrm{S\,cm^{-1}}$ at $600\,^{\circ}\mathrm{C}$, and an activation energy of around $0.67\,\mathrm{eV}$. This is one order of magnitude higher than the one previously reported by Iwahara et al., and only one order of magnitude lower than that of $BaZrO_3$.

Parallelly, $NaCaHSiO_4$ and related compounds $ABHXO_4$ (A=Li, Na or K. B=Ca, Sr or Ba. X=Si, Ge or Sn) were synthesized hydrothermally and subsequently characterized. Electrical characterization of $NaCaHSiO_4$ gave low conductivities, although protonic, of $1.8 \times 10^{-8}\,\mathrm{S\,cm^{-1}}$ at $250\,^{\circ}\mathrm{C}$, with an activation energy of $0.9\,\mathrm{eV}$. Based on the results, we propose a defect model in which interstitial hydroxide ions and interstitial protons str significant defects in the compound.

However, although $NaCaHSiO_4$ could be successfully synthesized and subsequently characterized, the other syntheses did not yield the desired results. In fact, the only synthesis that yielded a pure product was that which gave Sr_2SiO_4, possibly providing a hydrothermal approach to synthesizing a compound previously produced by a high-temperature solid state reaction.

Lastly, the compound BaH_2SiO_4 was synthesized, according to a hydrothermal route, and characterized with respect to thermal stability and electrical conductivity. It was found to exhibit a conductivity of $2.5 \times 10^{-8}\,\mathrm{S\,cm^{-1}}$ at $200\,^{\circ}\mathrm{C}$ with an activation energy of $0.88\,\mathrm{eV}$, comparable to that of $NaCaHSiO_4$. Due to BaH_2SiO_4 showing similar response to various atmospheres as $NaCaHSiO_4$, a defect model containing hydroxide and hydrogen interstitials is proposed for BaH_2SiO_4 as well.

Compared to earlier reports, a discrepancy was found in that the BaH_2SiO_4 decomposes prior to temperature regions in which data on electrical conductivity has been previously reported. Another, separate investigation into BaH_2SiO_4 is therefore recommended.

Acknowledgements

Over the last two years I have had the opportunity to work on a project that was a bit out of the ordinary. It has been two interesting years, with the project continuously evolving as experiments gave unexpected results, and new roads have had to be paved. In the end, I arrived at a goal that was not the one I initially set out for. However, looking back, it has been quite a journey, and I am left with a lot of knowledge and ideas for the future.
I would like to express my gratitude to my supervisors, Truls Norby and Sabrina Sartori, for their continuous support and for their eagerness to help me when I have had questions, at times resulting in a long email dropping into my inbox in the middle of the night.
I would like to thank Reidar, Einar and Ragnar for having the time and patience to assist me with instruments, interpretations, defect chemistry, and everything else I have needed help with. Additionally, I would like to thank all the people in FASE. There was always someone I could ask.
I would also like to give a shout-out to Kevin Nguyen for the many discussions we have had in order to understand what we have been doing.
Lastly, I am very grateful for my family for their love and support, even though they are not entirely sure about what I have been working on during all these years.

Contents

List of Figures

List of Tables

Chapter 1

Introduction

Every year, the U.S. Energy Information Administration release their annual *International Energy Outlook*, a large report in which they attempt to project the world energy consumption in the years to come. In the report released in 2016, it was estimated that the world energy consumption would increase by 48% by 2040 [7]. Additionally, it is generally accepted in the population that climate changes are a fact, and many scientists believe that one of the reasons for this is pollution due to human activities, including energy production. Efforts therefore have to be made to prevent further change in the environment, or find ways to repair some of the damage already done. It is essential that society as a whole comes together to tackle the challenges posed here, with the goal of constructing a bright and sustainable future to ensure that subsequent generations can live and thrive on planet Earth.

All over the world, scientists are investigating different approaches to producing electricity in new, more efficient and environmentally safe ways. A great challenge is to produce huge amounts of electricity, in a way that is both sustainable for the planet and harmless to its inhabitants.

One area of interest for energy production is how various fuel sources, other than gasoline and other hydrocarbons, can be utilized in efficient and environmentally safe techniques to produce clean energy. One promising generator of electricity is the fuel cell; a device that can produce electricity by breaking down hydrogen gas. The advantages of this kind of generator, other than the multitude of possible fuels, is that the chemical reaction taking place yields water as a product. A typical fuel cell utilizes pure hydrogen gas as its fuel source, however other hydrogen-containing fuels, such as methane (CH_4) [8] and ammonia (NH_3) [9] can be used as well.

1.1 Fuel Cells

A fuel cell consists of five parts; two interconnects that allows for connection to other cells, two electrodes to promote reaction and produce the electric current, and an electrolyte to seperate the electrodes. A fuel cell converts, through electrochemical processes, chemical energy stored in hydrogen to electrical energy which can used as seen fit. The overall reaction in a fuel cell is

$$H_2(g) + \frac{1}{2}O_2(g) \rightarrow H_2O(g) \tag{1.1.1}$$

The electrodes do much of the work in the cell. The anode must be stable under reducing conditions, in addition to being catalytic to the oxidation of hydrogen, $H_2(g) \rightarrow 2H^+ + 2\,e^-$, whereas the cathode must be stable under oxidizing conductions and be catalytic to the reduction of oxygen to yield water by $\frac{1}{2}O_2(g) + 2e^- + 2H^+ \rightarrow H_2O(g)$. Additionally, the electrodes and the interconnects need to have high electronic conductivity to facilitate the movement of electrons through an outer circuit.

The electrolyte is a part of the fuel cell that is difficult to create due to the many requirements that are imposed upon it. It is a critical component that separates the two electrodes and compels the electrons from the reaction to travel through the outer circuit, giving useful electricity, while at the same time conducting ions through itself to allow for recombination at the other side. The electrolyte will be in contact with both electrodes and, therefore, it is crucial that the electrolyte is stable under both reducing and oxidizing conditions. This leads to multiple challenges, as a potential electrolyte that is incredibly stable under reducing conditions might be utterly useless in oxidizing conditions. Additionally, the electrolyte is required to have a low or negligible electron conductivity to promote a current through the outer circuit, but at the same be an excellent ionic conductor for ions such as O^{2-}, H^+, OH^-, H_3O^+ or $CO_3{}^{2-}$. The electrolytes can be liquid or solid, with liquid electrolytes comprising aqueous solutions of acids (e.g. H_3PO_4) or bases (e.g. KOH), or molten salts like Li_2CO_3. More recently, ionic liquids, salts with melting temperatures below $100\,^\circ\mathrm{C}$, have been taken into use as electrolytes in Li-ion batteries [10]. Researching and developing new electrolytes for use in fuel cells is a difficult task due to all the factors that need to be considered in order to make them successful.

The variety of fuel sources available for fuel cells implies that fuell cells, and their electrolytes, will have to work in different ways. These days, there is a lot of research being carried out on *Solid Oxide Fuel Cells* (SOFC), *Molten Carbonate Fuel Cells* (MCFC) and *Proton Exchange Membrane Fuel Cells* (PEMFC) [11]. SOFCs and MCFCs are both fuel cells that operate at high temperatures; MCFCs operate at 600 to $700\,^\circ\mathrm{C}$ whereas SOFCs go all the way up to $1000\,^\circ\mathrm{C}$. PEMFCs are so-called low temperature fuel cells and typically operate in the range of 50 to $100\,^\circ\mathrm{C}$.

1.1.1 High Temperature: MOFCs and SOFCs

MCFCs utilize a melt of various carbonates (e.g. M_2CO_3, M=Li, Na, K [12]) in contact with two porous electrodes as the electrolyte. The anode is typically nickel while the cathode is Li-doped NiO. It can use fuel containing carbon monoxide, that would in

other cases be toxic to the fuel cell, and separates the hydrogen from water through the high-temperature water shift reaction $CO(g) + H_2O(g) \rightleftharpoons CO_2(g) + H_2(g)$.

Solid oxide electrolytes comprise ionic conductors, such as Y-stabilized ZrO_2 (YSZ) or Gd-doped GeO_2 (GDC), and are used in SOFCs or *solid oxide electrolyzer cells* (SOECs). In these materials, the acceptor dopants are compensated by oxygen vacancies which enable ionic transport. A difference between SOFCs and other types of cells is that, here, the charge carrier is an oxide ion (O^{2-}), in contrast to it being a proton (H^+), and is transferred from the cathode to the anode through the electrolyte. As it arrives at the anode, it recombines with hydrogen to yield water. The anode is typically a porous Ni+YSZ (Yttrium Stabilized Zirconia) cermet.

The advantages of both SOFCs and MCFCs are that they have, as of 2009, reported efficiencies of 50 to $60\,\%$ [11], and the high operating temperature and their internal steam reforming capabilities imply that they do not require a seperate reformer to extract the hydrogen from the fuel or a metal catalyst (e.g. expensive platinum) in order to promote a reaction. I.e. the high temperature promotes the reforming reaction. However, these types of cells are expensive and and have a relatively long start-up time. Additionally, the Ni-electrode is easily poisoned by hydrogen sulphide [13], and voltage drops in SOFCs are observed to occur even at low H_2S-concentrations of $0.05\,\mathrm{ppm}$ [14].

1.1.2 Low- and Intermediate Temperatures

Whereas the high temperature SOFCs and MCFCs have moderate efficiencies of 50 to $60\,\%$, and a seemingly low cost of $\$0.003$ to $0.001\,\mathrm{kW}^{-1}$ (When considering factors such as their stationary applications, their high capacities, as well as the cogeneration and reuse opportunities of the heat in the system), the low temperature fuel cells have lower efficiencies in the range 10 to $30\,\%$ and cost around $\$3$ to $4\,\mathrm{kW}^{-1}$ [15]. However, SOFCs and MCFCs are, partly due to their high operating temperatures, primarily useful for stationary applications and are poor generators for use in mobile systems. To overcome this obstacle, low temperature fuel cells need to be further researched and developed to increase both efficiency of the cells, and the chemical stability of the materials that make the cell.

Some oxides contain oxygen vacancies created by acceptor doping. In some oxides, these vacancies are readily hydrated in the presence of water vapour, according to $v_O^{\cdot\cdot} + O_O^x + H_2O \rightarrow 2OH_O^{\cdot}$, and the oxides become proton conducting. In this case, the protons are bonded to oxide ions as hydroxide ion defects, but they move around by jumping between oxide ion hosts in a free proton (Grotthuss) mechanism [16]. The protons move with an activation energy lower than that for oxygen vacancies,

and conduction can in principle be achieved at lower temperatures. Acceptor doping and consequent proton conduction has been described for a number of binary (e.g. TiO_2 [17] and Y_2O_3 [18]) and ternary oxides (e.g. Y-doped $BaZrO_3$ [19] and $LaNbO_4$ [20]), but also for oxoacid salts, such as Ca-doped $LaPO_4$ [21] and K-doped $Ba_3(PO_4)_2$ [5]. Additionally, nominally un-doped oxides, and water-free inorganic compounds such as layered phosphates, may in some cases take up water and become proton conducting [22].

An example of a water-free compound is the Nafion® membrane; it is a so-called *Polymer Electrolyte Membrane* (PEM). The electrolyte is a polymer that can absorb water to create liquid-like regions within the memberane. The membrane appears as a solid, but holds a liquid ion conductor in its pores. These "pools" of water promote conductivity because the protons are able to travel through the membrane by attaching themselves to the water molecules and traverse the membrane as H_3O^+ (vehicle mechanism [16]). The operating temperatures of cells utilizing these membranes are usually below $100\,^{\circ}\mathrm{C}$ in order to keep the water content in the membrane sufficient. Unfortunately, energy will be wasted in the cells because of the permeability of the fuel molecules and the drag force caused by the H_3O^+-molecule that has to travel against the stream of H_2O moving the opposite way.

There is one class of solid electrolytes that comprise materials with stoichiometric structural protons, as compared to the previously discussed compounds where a charge carrier (a proton) must be introduced by defects or water absorption. In these compounds, the protons are bonded to oxide ions, but in integer amounts, and they are a part of the structure. A prerequisite for proton transport is the appearance of defecets that the protons can move through. These can be created through thermal disorder, such as in the high temperature forms of solid acids such as $CsHSO_4$ [2], in which the anions are tetrahedral SO_4^{2-} units, and the four oxide ions are randomly occupied by a proton. $CsHSO_4$ shows decent conductivity in the narrow temperature span between the lower limit of the superprotonic state (150 to $200\,^{\circ}\mathrm{C}$) and the melting or decomposition temperature (220 to $300\,^{\circ}\mathrm{C}$). Some problems of this and similar compounds include their solubility in water and their plasticity in the high conductivity phase.

There have been some studies on proton conductivity in barium phosphates. In one study, for instance, released in 2009, a group of scientists synthesised and measured $Ba_{3-x}K_xH_x(PO_4)_2$ and found that with the stoichiometry $x = 0.80$, a conductivitiy that was 3 orders of magnitude higher than for pure $Ba_3(PO_4)_2$ was displayed [5]. At $250\,^{\circ}\mathrm{C}$ the conductivity was found to be about $2.4 \times 10^{-4}\,\mathrm{S\,cm^{-1}}$, a value lower than that of $CsHSO_4$ at the same temperature. However, the compound was found to be highly insoluble in water and possess a relatively high thermal stability. Furthermore, in

march 2015, a group of japanese scientists measured the proton conductivity in phosphate glasses containing large amounts of water [23]. The compound $30\mathrm{BaO}-70\mathrm{P_2O_5}$ was synthesized and measurements performed displayed conductivities slightly below $1 \times 10^{-3}\,\mathrm{S\,cm^{-1}}$ at $250\,^{\circ}\mathrm{C}$. The Ba-compound was found to contain $11\,\mathrm{mol}\,\%$ $\mathrm{H_2O}$. This water incorporated in the structure implies that there may be a large amount of "mobile" protons available for conduction. However, this might turn out to be a composite of a ceramic matrix where phosphoric acid has been absorbed, e.g. from hydration of surplus phosphorous oxide $\mathrm{P_2O_5}$ used during synthesis, and the conduction is therefore not representative of the glass $30\mathrm{BaO}-70\mathrm{P_2O_5}$.

For solid-state materials, the mechanism of free proton jumps appears to dominate the conduction, whereas it for liquid-state conductors is dominated by a vehicle mechanism, often aided by convection. An interesting though to be considered further is if other phosphates can be hydrated and if this hydration will yield more charge carriers and favorable paths for conduction. What about sulphates? To achieve high proton conductivities, a high concentration of protons with high mobility is required. The presence of protons can be achieved by doping, or by using materials with structural protons. In the latter case, defects must be introduced to give a pathway for the protons and to increase their mobility.

1.2 Goal of Project

The goal of this project is to search for and investigate new solid-state proton conductors. More specifically, the project will focus on systems that can be classified as 'Alkali and Alkaline Earth Oxoacid Salts', or 'Solid Acids' for short. In these compounds, the anionic groups are tetrahedral $\mathrm{XO_4}$ units that could, potentially, facilitate the transport of protons through the crystal. For example, $\mathrm{K_2SO_4}$ has been reported to have disordered $\mathrm{SO_4^{2-}}$ groups that are able to reorientate, possibly enhancing the cationic mobility [24]. In contrast to systems with $\mathrm{SO_4^{2-}}$ units, like $\mathrm{CsHSO_4}$, this project will involve systems in which the anionic group is $\mathrm{PO_4^{3-}}$ and even $\mathrm{SiO_4^{4-}}$. Potential new solid acids can be constructed by looking to $\mathrm{CsHSO_4}$ and $\mathrm{CsH_2PO_4}$. Both compounds are very good proton conductors, but they are water soluble and decompose or melt at relatively low temperatures. The increased valency of the anionic groups increases the thermal stability of the compound, in addition to decreasing the solubility of said compound, as indicated by $\mathrm{CsH_2PO_4}$ being overall more stable than $\mathrm{CsHSO_4}$. Therefore, it would be reasonable to assume that going further left in the periodic table, to silicates, one would obtain compounds that are even more stable. If so, then germanates and stannates might also be of interest. Both compounds have metal cation to anion molar ratios of 1:1, and

part of this project will be to investigate the combination of alkaline and alkaline earth cations in order to obtain 1:1 ratio of cations and anions, and to introduce disorder.
In 2015, there were reports that $KBaPO_4$, a previously uncharacterised compound, could be hydrated through steam at $80\,^{\circ}\mathrm{C}$ (i.e. a high water vapour pressure) into a novel low-temperature protonic conductor that would exhibit a significant protonic conductivity of $1 \times 10^{-2}\,\mathrm{S\,cm^{-1}}$ at just below $100\,^{\circ}\mathrm{C}$. A major part of this project will be to synthesize $KBaPO_4$ and characterize it in different ways, as well as investigating the validity of the claim that it can be hydrated with steam.
$NaCaHSiO_4$ and BaH_2SiO_4 have been briefly characterized [25, 26]. In addition to synthesizing and further characterizing these compounds, a group of compounds $ABHXO_4$ (A=Li, Na or K. B=Ca, Sr or Ba. X=Si, Ge or Sn) will be attempted synthesized and, if successful, characterized.

Chapter 2

Theoretical Background

2.1 Ionic Conductivity

Ionic conductivity is an important aspect of a material's electrical properties. Ionic conduction is the term used for when charged species, e.g. ions, move through matter. In an aqueous solution of NaCl, Na^+ and Cl^- exist as ionic species, and are "free"[1] to move through the solution. This movement can be either due to random diffusion due to thermal energy, or by an electrical potential which would cause Na^+ and Cl^- to accumulate at the cathode and anode, respectively.

Protonic Conductivity

Protons, positively charged hydrogen ions, move in very much the same way as other ions, and there are multiple pathways and mechanisms a proton can utilize in order to move through a medium. For one, movement is possible through a lone-migration process, i.e. where the protons move on their own, such as the Grotthuss mechanism, or by a vehicle mechanism in which the proton migrates by attaching to a proton-accepting species such as H_2O or NH_3 and subsequently travels along with it as H_3O^+ or NH_4^+ [16].

2.1.1 Conduction Through Defects in Solids

In a solid, an ionic species has to move through a more constrained pathway, depending on both the symmetry of the solid and the energy barriers it would have to traverse along the way. In a crystal, atoms reside on specific locations known as lattice points. At temperatures above 0 K, a crystal will deviate from its perfect zero-temperature structure and contain defects, e.g. oxygen vacancies $v_O^{\cdot\cdot}$, that will influence the material's properties, and allow for the movement of electrically charged species (Ions, electrons, holes) throughout the crystal. In the case of oxygen vacancies (a point defect), oxide ions (O^{2-}) or hydroxide ions (OH^-) would be able to move through the lattice by jumping between these lattice points, given that there is a driving force, e.g. a concentration gradient. As a rule of thumb, as long as the moving ionic species is of an adequate size and can compensate for the charge of the defect, movement is possible.

[1] Free as in not constrained to one another. A charged species in an aqueous solution will to some extent pull on the polar solvent molecules.

2.1.2 Calculation of Conductivity and Activation Energy

This section is based on theory from [27] and chapter 7 in [28].

In the presence of an electric field, all charged particles will be subjected to a force proportional to the field strength and the charge of the species. This force will cause positive and negative charges to be drawn towards, respectively, the anode and the cathode. Effectively, the resulting current density is given as $j_i = \sigma_i E$, where σ_i denotes the specific conductivity of the species i and E is the electric field strength. σ_i can also be considered the *partial electrical conductivity of the species i*, and can be expressed as a product of the the charge (z_i) of, the concentration (c_i) of, and the mobility (u_i) of the charged species, as well as the elementary charge e. This is summarized in equation 2.1.1. Should the species i be a defect (e.g. an oxygen vacancy $v_O^{\cdot\cdot}$), then c_i would reflect the concentration of the defect, possibly being considered constant due to a dopant, and u_i would be the mobility of the defect itself.

$$\sigma_i = z_i e c_i u_i \tag{2.1.1}$$

If a charged species moves through an activated jump mechanism, diffusion theory can provide a reasonable explanation of the conduction process, and it is then possible to relate the mobility of the species to the diffusion coefficient through the Nerns-Einstein equation [27]

$$D_i = u_i \cdot \frac{RT}{z_i e} = \sigma_i \cdot \frac{k_B T}{c_i z_i^2 e^2} \tag{2.1.2}$$

where D_i denotes the self-diffusion coefficient of the charged species i, R and k_B both denote the Boltzman's constant, and T is the absolute temperature.

Further evaluation of equation 2.1.2 in an Arrhenius plot can be used to extract information regarding the entropies of formation and of mobility, as well as the activation energy for the process. To achieve this, it is necessary to construct a plot of $\ln(\sigma T)$ *vs* $\frac{1}{T}$, according to equation 2.1.3.

$$\sigma_i T = \sigma_0 \cdot \exp(-\frac{\Delta E_a}{k_B T}) \tag{2.1.3}$$

where $E_a = \Delta H_{\text{formation}} + \Delta H_{\text{mobility}}$ is the activation energy, describing the enthalpies of formation and mobility of the charged species. The activation energy describes the barrier that the species must overcome in order to be able to move. σ_0 is the pre-exponential factor, containing the entropies of formation of the charge carrier and its mobility, and it

can be written as in equation 2.1.4 [29].

$$\sigma_0 = Ne^2\alpha^2c(1-c)\gamma k_B^{-1}\omega_0 \exp(\frac{S}{k_B}) \tag{2.1.4}$$

where N is the number of lattice sites available for the mobile ions, e is the electronic charge, α is the jump distance, c is the fractional occupancy of the mobile ion sites, γ is a correlation factor, k_B is the Boltzman's constant, ω_0 is the fundamental vibrational frequency of the mobile ions, and S is the entropy of formation and mobility.

The process for obtaining experimental values for the activation energy is described in section 2.3.3.

2.2 Defects and Structural Considerations

This section is based on [27].

The mobility of a species through a crystal is affected by multiple factors. For instance, how the crystal is constructed and which atomic species are present play a part in forming the energy volume with varying electrical potentials between different locations in the crystal. To have movement throughout a crystalline solid, it is critical that there are defects present. These defects present possible pathways that a charged species will be able to move through.

2.2.1 Defect Chemistry

Defects fall in different categories depending on their dimensionality. 0-dimensional defects include point defects like oxygen vacancies $v_O^{\cdot\cdot}$ or interstitial hydrogen $H_i^{\cdot}$. 1- and 2-dimensional defects include, respectively, line defects, also known as dislocations, and plane defects stemming from grain boundaries and stacking faults. 3-dimensional defects are volume defects, for example areas where a secondary phase has precipitated. All the various defects affect a material's properties.

Kröger and Vink [30] devised a system of notation to describe point- and electronic defects in solid materials. The system allows for describing the equilibrium and concentrations of various defects. A point defect is written as A_p^q, where A is chemical species, p is the lattice location of the defect and q is the effective charge (With "." for positive and "/" for negative charges.). Additionally, electrons and holes are denoted $e^{/}$ and $h^{\cdot}$, respectively.

2.2.2 Defect Models

General Defect Considerations

There is no previous documentation regarding possible defect models for the compounds explored in this project, and the approximation towards models performed here is therefore very general, and the possible defects that could be present in each case are explained and discussed.
The compounds in the project are intended to be stoichiometric, and no foreign dopants are intentionally added. Due to the covalency of the bonds in the tetrahedral XO_4-anion and the bonding scheme in the compounds having an ionic nature, in addition to there not being any transition metals with multiple oxidation states present, it is reasonable to make the assumption that neither electrons nor electron holes will have any significant contribution on the total conductivity of the compounds in this project.
For a compound AXO_4 where the anion is a tetrahedral XO_4 unit, some possible defects are as follows:

- Intrinsic Ionization of electrons:

$$0 = \mathrm{e}^{/} + \mathrm{h}^{\cdot} \tag{2.2.1}$$

- Schottky:

$$0 = \mathrm{v}_{\mathrm{A}}^{\mathrm{a}/} + \mathrm{v}_{\mathrm{XO_4}}^{\mathrm{a}\cdot} \tag{2.2.2}$$

- Frenkel:

$$\mathrm{A}_{\mathrm{A}}^{\mathrm{x}} + \mathrm{v}_{\mathrm{i}}^{\mathrm{x}} = \mathrm{v}_{\mathrm{A}}^{\mathrm{a}/} + \mathrm{A}_{\mathrm{i}}^{\mathrm{a}\cdot} \tag{2.2.3}$$

- Anti-Frenkel:

$$(\mathrm{XO_4})_{\mathrm{XO_4}}^{\mathrm{x}} + \mathrm{v}_{\mathrm{i}}^{\mathrm{x}} = \mathrm{v}_{\mathrm{XO_4}}^{\mathrm{a}\cdot} + (\mathrm{XO_4})_{\mathrm{i}}^{\mathrm{a}/} \tag{2.2.4}$$

- Oxygen-deficiency (The $(\mathrm{X_2O_7})_{\ddot{2}\mathrm{XO_4}}$-group can also be written as $\mathrm{v}_{\ddot{\mathrm{O}}}$):

$$2(\mathrm{XO_4})_{\mathrm{XO_4}}^{x} = (\mathrm{X_2O_7})_{\ddot{2}\mathrm{XO_4}} + 2\mathrm{e}^{/} + \frac{1}{2}\mathrm{O_2(g)} \tag{2.2.5}$$

- Metal-excess:

$$\mathrm{A}_{\mathrm{A}}^{\mathrm{x}} + \mathrm{v}_{\mathrm{i}}^{\mathrm{x}} + \frac{a}{2}\mathrm{O}_{\mathrm{O}}^{\mathrm{x}} = \mathrm{A}_{\mathrm{i}}^{\mathrm{x}} + \frac{a}{4}\mathrm{O_2(g)} \tag{2.2.6}$$

- Oxygen-excess:

$$\frac{a}{2}\mathrm{O_2} + a\mathrm{v}_{\mathrm{i}}^{\mathrm{x}} = a\mathrm{O}_{\mathrm{i}}^{//} + 2a\mathrm{h}^{\cdot} \tag{2.2.7}$$

- Metal-deficiency:

$$\frac{a}{2}\mathrm{O}_2 = \mathrm{v}_\mathrm{i}^{2a/} + a\mathrm{O}_\mathrm{O}^\mathrm{x} + 2a\mathrm{h}^\cdot \tag{2.2.8}$$

Due to the compounds in question being ionic, and there are no atomic species with variable oxidation states present, the likelihood of electronic defects forming is almost non-existing, and the compounds will most likely not be electronic conductors.

Schottky defects would require diffusion of a lattice position accommodating for the XO_4 group, which would realistically have a large activation energy, allowing for neglecting the presence of Schottky defects when considering defect models for this project.

It is very difficult for the big XO_4 group to move to an interstitial site, but there is a possibility of an oxygen atom moving alone: $\mathrm{O}_\mathrm{O}^\mathrm{x} + \mathrm{v}_\mathrm{i}^\mathrm{x} = \mathrm{v}_\mathrm{O}^{\cdot\cdot} + \mathrm{O}_\mathrm{i}^{//}$. The positive oxygen vacancy would interact with the positive X species and the tetrahedra would distort. In the case of PO_4, two groups could interact to form a P_2O_7 chain. Frenkel defects may, to some extent, be present in the structure. However, due to the covalency of the $\mathrm{X}-\mathrm{O}$ bonds in the XO_4 units, the likelihood of an oxygen atom leaving its site and enter an interstitial position is minimal, and Anti-Frenkel defects will not be present.

An oxygen deficiency would effectively give an increased electronic density on the remaining atoms in the XO_4 group as this is where the most electronegative constituents are. Considering the existence of pyrophosphates $P_2O_7^{2-}$ and pyrosilicates $Si_2O_7^{6-}$ and their stabilities, this situation would cause these anionic groups to form in the crystal (As suggested for $LaPO_4$ [31]), effectively locking multiple tetragonal units together and prohibiting movement, including rotation, of the independent groups. Additionally, due to the ionic nature of the compounds investigated in this project (Alkali and alkaline earth cations), and that there are no variable valences on the cations, the potential oxygen vacancies would more realistically be balanced by non-stoichiometric cation deficits.

An oxygen vacancy could, along with an oxygen site, be hydrated through

$$\mathrm{v}_\mathrm{O}^{\cdot\cdot} + \mathrm{O}_\mathrm{O}^\mathrm{x} + \mathrm{H}_2\mathrm{O} \rightleftharpoons 2\mathrm{OH}_\mathrm{O}^\cdot \tag{2.2.9}$$

A metal excess would, effectively, yield electron donors through the interstitial metal species potentially being oxidized. However, the alkali and alkaline earth cations are already fully oxidized, rendering this type of defect unlikely to occur.

Whereas the situation for excess oxygen would predominantly give interstitial oxygen ions that could give electron holes as a potential charge carrier, a metal deficiency would call for the formation of new structural sites of all species. The latter would effectively require there to be both X and O available in the surrounding atmosphere. Oxygen is

plentiful, but the presence of phosphorous and silicon gas is negligible and this type of defect can therefore be considered highly unrealistic.

Model for $KBaPO_4$

The previous discussion implies that electronic defects will not be present in compounds like $KBaPO_4$. Therefore, the normal formation of oxygen vacancies will not be considered, and the reality might be that the oxygen vacancies are balanced by non-stoichiometric defects such as potassium- or barium-vacancies.
Among the cations, K^+ and Ba^{2+} are similar in size and, depending on the relative sizes between the cations and the phosphate group, both barium and potassium could potentially move to interstitial positions as Frenkel defects. Additionally, defects in the structure may also be a result of non-stoichiometry during synthesis and calcination. This could be a result of the weigh-in of and the purities of the reactants used, but also the various processes and temperatures used during synthesis. For instance, barium has the potential to form $Ba(OH)_2$ and evaporate above $780\,^{\circ}\mathrm{C}$.
Altogether, it is reasonable to assume that $KBaPO_4$ contains some inherent potassium and barium vacancies, as well as potential phosphate vacancies. The former two can be balanced by the phosphate vacancies and oxygen vacancies (In the form of pyrophosphate groups ($(P_2O_7)^{\cdot\cdot}_{2PO_4}$).

Seeing as $KBaPO_4$ does not contain any protons initially, protonic species must be introduced somehow.
One way is for the hydration of oxygen vacancies

$$H_2O + v_O^{\cdot\cdot} + O_O^x = 2OH_O^{\cdot} \tag{2.2.10}$$

Additionally, even though oxygen themselves are unable to leave their position and enter interstitial positions, one could imagine an interstitial vacancy being hydrated and accommodating a hydroxide ion. This situation is presented in equation 2.2.11.

$$H_2O + v_i^x + O_O^x = OH_i^{\prime} + OH_O^{\cdot} \tag{2.2.11}$$

It has been reported that Frenkel defects ($K_K^x + v_i^x = v_K^{\prime} + K_i^{\cdot}$) are the predominating defects in K_2SO_4 [24]. Because of $KBaPO_4$ being isostructural with K_2SO_4 [32], it is reasonable to assume that Frenkel defects will be of significance in $KBaPO_4$ as well. In this case, a potassium or a barium ion moves to an interstitial position, leaving corresponding vacancies behind. However, due to Ba^{2+} being divalent, the possibility of barium Frenkel defects being present is neglected here. Additionally, the intuitively low

mobility of the ion, as has been reported for $Ba_3(PO_4)_2$ [33], might render the effect of barium ions on the conductivity to be negligible.
Even though oxygen vacancies do not form along with electronic defects, there could be oxygen vacancies present that are compensated by either potassium or barium vacancies. In this case, due to the possible evaporation of $Ba(OH)_2$ during synthesis, we assume that barium vacancies are present as acceptors, compensated by oxygen vacancies. Subsequently, these oxygen vacancies can be hydrated by equations 2.2.10 or 2.2.11.
Collectively, the defects of importance will have the following defect reactions and corresponding defect equilibrium constants:

- Barium vacancies compensated by oxygen vacancies:

$$[v''_{Ba}] = [v^{\cdot\cdot}_{O}] \tag{2.2.12}$$

- Potassium-Frenkel:

$$K^{x}_{K} + v^{x}_{i} = v'_{K} + K^{\cdot}_{i} \tag{2.2.13}$$

$$K_{F,K} = [v'_{K}] \cdot [K^{\cdot}_{i}] \tag{2.2.14}$$

- Hydration of oxygen vacancies:

$$H_2O + v^{\cdot\cdot}_{O} + O^{x}_{O} = 2OH^{\cdot}_{O} \tag{2.2.15}$$

$$K_{Hyd1} = \frac{[OH^{\cdot}_{O}]^2}{[v^{\cdot\cdot}_{O}] \cdot pH_2O} \tag{2.2.16}$$

- Hydration through hydroxide interstitials:

$$H_2O + v^{x}_{i} + O^{x}_{O} = OH'_{i} + OH^{\cdot}_{O} \tag{2.2.17}$$

$$K_{Hyd2} = [OH'_{i}] \cdot [OH^{\cdot}_{O}] \cdot pH_2O^{-1} \tag{2.2.18}$$

Note that none of the defects show a pO_2-dependency.
An electroneutrality condition containing these defects will then be as in equation 2.2.19.

$$[K^{\cdot}_{i}] + 2[v^{\cdot\cdot}_{O}] + [OH^{\cdot}_{O}] = [v'_{K}] + 2[v''_{Ba}] + [OH'_{i}] \tag{2.2.19}$$

Now, it is possible to investigate situations in which various defects are in the majority.

- **Case 1 - Frenkel defects are minority defects:**

  In this case, the charge neutrality in equation 2.2.19 will be reduced to

$$2[v^{\cdot\cdot}_{O}] + [OH^{\cdot}_{O}] = 2[v''_{Ba}] + [OH'_{i}] \tag{2.2.20}$$

  Following this, we can make the assumption that $2[v''_{Ba}] \gg [OH'_{i}]$ and get

$$2[\mathrm{v}_{\mathrm{O}}^{\cdot\cdot}] + [\mathrm{OH}_{\mathrm{O}}^{\cdot}] = 2[\mathrm{v}_{\mathrm{Ba}}^{//}] \tag{2.2.21}$$

This will lead to:

- $[\mathrm{v}_{\mathrm{Ba}}^{//}] = [\mathrm{v}_{\mathrm{O}}^{\cdot\cdot}] =$ constant, low $\mathrm{pH_2O}$

$$[\mathrm{OH}_{\mathrm{O}}^{\cdot}] = K_{\mathrm{Hyd1}}^{\frac{1}{2}} \cdot [\mathrm{v}_{\mathrm{Ba}}^{\cdot\cdot}]^{\frac{1}{2}} \cdot \mathrm{pH_2O}^{\frac{1}{2}} \tag{2.2.22}$$

$$[\mathrm{OH}_{\mathrm{i}}^{/}] = K_{\mathrm{Hyd2}} \cdot K_{\mathrm{Hyd1}}^{-\frac{1}{2}} \cdot [\mathrm{v}_{\mathrm{Ba}}^{\cdot\cdot}]^{-\frac{1}{2}} \cdot \mathrm{pH_2O}^{\frac{1}{2}} \tag{2.2.23}$$

- $2[\mathrm{v}_{\mathrm{Ba}}^{//}] = [\mathrm{OH}_{\mathrm{O}}^{\cdot}] =$ constant, high $\mathrm{pH_2O}$

$$[\mathrm{v}_{\mathrm{O}}^{\cdot\cdot}] = K_{\mathrm{Hyd1}}^{-1} \cdot 4[\mathrm{v}_{\mathrm{Ba}}^{//}]^2 \cdot \mathrm{pH_2O}^{-1} \tag{2.2.24}$$

$$[\mathrm{OH}_{\mathrm{i}}^{/}] = K_{\mathrm{Hyd2}} \cdot (2[\mathrm{v}_{\mathrm{Ba}}^{\cdot\cdot}])^{-1} \cdot \mathrm{pH_2O} \tag{2.2.25}$$

This case has been drawn up in a Brouwer diagram, and is displayed in figure 2.1.

- **Case 2 - Frenkel defects are majority defects**

  Should $\mathrm{KBaPO_4}$ turn out to be very stoichiometric, the concentration of oxygen vacancies will be small. Additionally, should $\mathrm{KBaPO_4}$ not be susceptible to hydration by either oxygen vacancies or hydroxide interstitials, then, following the earlier discussion, it could be that Frenkel defects (Potassium Frenkel defects, especially) are the predominating defects. In this case, the charge neutrality in equation 2.2.19 will reduce to simply containing the Frenkel defects. They will not have any significant, if any at all, $\mathrm{pO_2}$- nor $\mathrm{pH_2O}$-dependency.

$$[\mathrm{K}_{\mathrm{i}}^{\cdot}] = [\mathrm{v}_{\mathrm{K}}^{/}] \tag{2.2.26}$$

Effectively, the equation for total conductivity of $\mathrm{KBaPO_4}$, based on the discussion of the importance of the inherent defects, will be given as in equation 2.2.27. Each defect can be linked to the concentration and mobility of the defect, according to equation 2.1.1), and in the case that the defects that have $\mathrm{pH_2O}$-dependencies should affect the overall conductivity of $\mathrm{KBaPO_4}$, then this will be observable through electrical measurements with varying $\mathrm{pH_2O}$.

$$\sigma_{\mathrm{tot}} = \sigma_{\mathrm{K_i}} + \sigma_{\mathrm{v_K}} + \sigma_{\mathrm{Ba_i}} + \sigma_{\mathrm{v_{Ba}}} + \sigma_{\mathrm{v_O}} + \sigma_{\mathrm{OH_O}} + \sigma_{\mathrm{OH_i}} \tag{2.2.27}$$

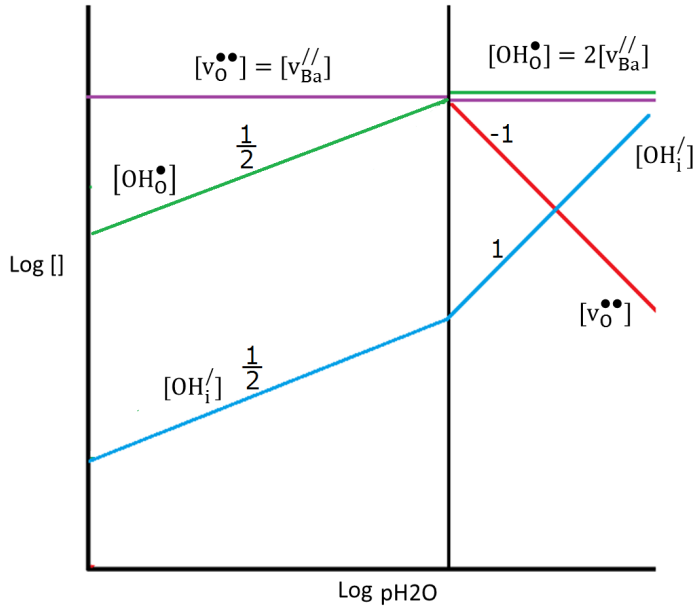

Figure 2.1: Brouwer diagram for the pH_2O-dependency of $KBaPO_4$ in the case of inherent barium vacancies giving rise to oxygen vacancies that are subsequently hydrated according to equation 2.1. Case 1.

Model for $NaCaHSiO_4$

The defect chemistry of orthosilicates has not been thoroughly investigated, however some assumptions can be made and possible defects can be proposed. As is the case for K^+ and Ba^{2+}, Na^+ and Ca^{2+} are also of similar size. In $NaCaHSiO_4$, however, there are structural protons that have the potential to move through the crystal. Similarly to $KBaPO_4$, there is the possibility of oxygen vacancies forming, giving rise to pyrosilicate groups in the same way as for pyrophosphates, although the ionic nature of the compound indicates that they would not give rise to electronic defects, and should oxygen vacancies be present, they would most likely be compensated by other negative defects, like inherent cation vacancies stemming from the synthesis.

The common process for forming oxygen vacancies in orthosilicates is given as

$$2(SiO_4)^x_{SiO_4} = (Si_2O_7)^{\cdot\cdot}_{2SiO_4} + 2e^{/} + \frac{1}{2}O_2(g) \tag{2.2.28}$$

Because a hydrothermal approach is used in order to synthesize this compound, loss of reactants as intermediates during the synthesis process is highly unlikely, due to the reaction taking place in a closed environment without the possibility of gaseous species

escaping. For the derivation of the following defect model, the system will be considered to be stoichiometric. For this reason, the presence of oxygen vacancies according to equation 2.2.28 will not be further considered, seeing as they give rise to electronic defects, unlikely in a stoichiometric phase of this ionic compound.
Seeing as earlier reports indicate that the compound is a protonic conductor, the defects of importance will be defects containing hydrogen. An intuitive defect (Equation 2.2.29) is a hydrogen Frenkel defect in which a hydrogen will leave its position and enter an interstitial, effectively leaving a negative hydrogen vacancy behind. As a proton seldom is alone, the hydrogen interstitials will be considered as $OH_O^{\cdot}$-defects in the following discussion.

$$\begin{aligned} H_H^x + v_i^x &= v_H^{/} + H_i^{\cdot} \\ H_H^x + O_O^x &= v_H^{/} + OH_O^{\cdot} \end{aligned} \tag{2.2.29}$$

With a corresponding equilibrium constant

$$K_{F,H} = [OH_O^{\cdot}] \cdot [v_H^{/}] \tag{2.2.30}$$

Two cases for defects that will have a pH_2O-dependency are presented:

- **Case 1:** A dehydration reaction occurs according to

$$2H_H^x + O_O^x = 2v_H^{/} + v_O^{\cdot\cdot} + H_2O(g) \tag{2.2.31}$$

$$K_{Dehyd} = [v_H^{/}]^2 \cdot [v_O^{\cdot\cdot}] \cdot pH_2O \tag{2.2.32}$$

  The charge neutrality condition will be

$$[OH_O^{\cdot}] + 2[v_O^{\cdot\cdot}] = [v_H^{/}] \tag{2.2.33}$$

  And there will be different pH_2O-dependencies based on what defects are the majority defects.

  In the case of $2[v_O^{\cdot\cdot}] = [v_H^{/}]$, at low pH_2O

$$[v_H^{/}] = (2K_{Dehyd})^{\frac{1}{3}} \cdot pH_2O^{-\frac{1}{3}} \tag{2.2.34}$$

$$[OH_O^{\cdot}] = K_{F,H} \cdot (2K_{Dehyd})^{-\frac{1}{3}} \cdot pH_2O^{\frac{1}{3}} \tag{2.2.35}$$

  In the case of $[OH_O^{\cdot}] = [v_H^{/}] = K_{F,H}^{\frac{1}{2}}$, at high pH_2O

$$[v_O^{\cdot\cdot}] = K_{Dehyd} \cdot K_{F,H}^{-1} \cdot pH_2O^{-1} \tag{2.2.36}$$

- **Case 2:** The compound is hydrated and an interstitial accommodates a hydroxide ion

$$H_2O + v_i^x + O_O^x = OH_i^{/} + OH_O^{\cdot} \tag{2.2.37}$$

$$K_{Hyd} = [OH_i^{/}] \cdot [OH_O^{\cdot}] \cdot pH_2O^{-1} \tag{2.2.38}$$

The charge neutrality condition will be

$$[v_H^{/}] + [OH_i^{/}] = [OH_O^{\cdot}] \tag{2.2.39}$$

And there will be different pH_2O-dependencies based on what defects are the majority defects.

In the case of $[OH_O^{\cdot}] = [v_H^{/}] = K_{F,H}^{\frac{1}{2}}$, at low pH_2O

$$[OH_i^{/}] = K_{Hyd} \cdot K_{F,H}^{\frac{1}{2}} \cdot pH_2O \tag{2.2.40}$$

In the case of $[OH_O^{\cdot}] = [OH_i^{/}]$, at high pH_2O

$$[OH_O^{\cdot}] = K_{Hyd} \cdot pH_2O^{\frac{1}{2}} \tag{2.2.41}$$

$$[v_H^{/}] = K_{F,H} \cdot K_{Hyd}^{-1} \cdot pH_2O^{-\frac{1}{2}} \tag{2.2.42}$$

Brouwer diagrams for Case 1 and Case 2 are shown in figures 2.2 and 2.3, respectively.

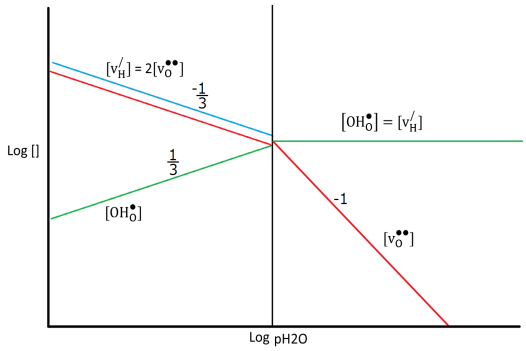

Figure 2.2: Brouwer diagram for the pH_2O-dependency of $NaCaHSiO_4$ in the case of hydrogen Frenkel defects and a dehydration according to equation 2.2.31, Case 1.

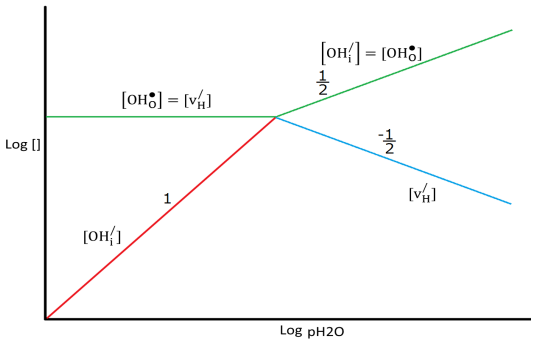

Figure 2.3: Brouwer diagram for the pH_2O-dependency of $NaCaHSiO_4$ in the case of hydrogen Frenkel defects and a hydration according to equation 2.2.37, Case 2.

And the significance of these defects can be investigated by electrical measurements in various pH_2O.

Model for BaH_2SiO_4

Similarly to $NaCaHSiO_4$, pyrosilicate groups can form as the compensating defect due to the formation of oxygen vacancies (Equation 2.2.28). Additionally, water can leave

the structure in the same way as in equation 2.2.31, or it can enter and give interstitial hydroxide groups as in equation 2.2.37. Additonally, the presence of interstitial hydrogen due to equation 2.2.29 could be a possibility.

As for $NaCaHSiO_4$, a hydrothermal approach is used to synthesize BaH_2SiO_4, and earlier reports indicate that it is a protonic conductor. Therefore, the assumptions made for $NaCaHSiO_4$ are made for BaH_2SiO_4 as well, and the defects of importance will again be taken to be oxygen and hydrogen vacancies, as well as hydroxide and hydrogen interstitials.

As for $NaCaHSiO_4$, we can set up three different sets of equations to represent the concentrations of the various species, along with their dependencies on pO_2 and H_2O. In fact, to avoid unnecessary repetition, we simply note that all equations written for $NaCaHSiO_4$ are valid for BaH_2SiO_4 as well.

2.3 Impedance Spectroscopy

This section is based on [34] and [35], as well as chapters 26-27 in [36].

Impedance spectroscopy is a powerful tool allowing one to observe how a physical system reacts to an applied current and investigate various physical processes occurring at different time scales. Effectively, this allows for: estimating rates of processes such as mass transport, interfacial reactions, and diffusion coefficients; determining the conductivity of species through solutions or solids; and other phenomena.

The technique is frequently applied in the field of fuel cell technology in order to study electrical properties of ionic membranes. Samples are then subjected to alternating current which polarizes different areas of the sample depending on the frequency of the current (i.e. the time scale of the process). Doing this, it is possible to get an overview of how the conductivity varies in, for example, bulk and grain boundaries, as these processes respond to the applied current at different frequencies, allowing them to be separated in the resulting impedance spectrum.

2.3.1 The Concept of Impedance

Resistance is the common term used to describe how a direct electric current (DC) is impeded by components in an electrical circuit. Impedance is the more collective term that encompasses how electrical components react to alternating electric currents (AC). For AC, the potential and the current will be out of phase due to inductive and capacitive

effects of the circuit elements. The voltage can be defined by the sinusoidal function

$$V(t) = |\Delta V| \cos(\omega t) \tag{2.3.1}$$

where $|\Delta V|$ is the amplitude of the voltage and ω is the angular frequency of the oscillating voltage. Likewise, the out-of-phase current response arising from this voltage can be written as

$$I(t) = |\Delta I| \cos(\omega t + \phi) \tag{2.3.2}$$

where $|\Delta I|$ is the amplitude of the current and ϕ represents the phase shift offset. The current is a product between a real component and an imaginary component that is $90°$ out of phase. These components are called, respectively, the *resistance* (R) and the *reactance* (X). The two components are included in the general term *impedance* (Z), which can then be represented in the complex plane as

$$Z = \text{Re}\{Z\} + i\text{Im}\{Z\} = R + iX \tag{2.3.3}$$

where Re and Im represent, respectively, the real and imaginary part of the complex number, and i is the imaginary unit.

Additionally, where the inverse property of *resistance* is known as the electrical *conductance* (With the unit Siemens), the inverse property of *impedance* is known as *admittance* and is given as

$$Y = \frac{1}{Z} = G + iB \tag{2.3.4}$$

where G is the *conductance* ($\frac{1}{R}$) and B is the imaginary part of the *admittance* and is labelled the *suseptance*.

2.3.2 Circuit Elements

Passive circuit elements are components that do not generate current or potential. The three components of interest for impedance spectroscopy are the resistor, the capacitor and the inductor. Their functionality and how they react to an alternating current vary, but the impedance can be calculated based on equation 2.3.3 and the relationship between the current and the voltage for the given component.

Resistor

A resistor (e.g. a wire) is an element in which long-range transport of charge carriers occur. In an ideal resistor, an applied AC voltage and current would be in phase, as there

would be no inductive or capacitive losses. The relationship between the current and the voltage for a resistor is given by Ohm's law, $V(t) = RI(t)$, and the impedance is given as the resistance itself

$$Z_{\text{Resistor}} = R = \frac{V}{I} \tag{2.3.5}$$

Capacitor

A capacitor is an ideal insulator placed between two conductors, commonly constructed as two parallel plate conductors separated by a dielectric (i.e. an electric insulator that can be polarized by an electric field). An ideal capacitor is characterized by a constant *capacitance* C, defined as the ratio between a charge Q on each of the conductor plates, and the voltage V between them. The current flowing through the capacitor is then obtained by considering the derivative of the charge with respect to time

$$I(t) = \frac{dQ(t)}{dt} = C\frac{dV(t)}{dt} \tag{2.3.6}$$

and the impedance of the capacitor is then given as

$$Z_{\text{Capacitor}} = \frac{1}{i\omega C} \tag{2.3.7}$$

where ω is the oscillation frequency of the applied voltage, and i is the imaginary unit.

Inductor

An inductor (e.g. a coiled wire) is an element in which the conducting current sets up a magnetic field around the conductor that, in turn, induces an AC voltage back in the conductor. The relationship between the current in and the potential difference for the inductor is given by

$$V(t) = L\frac{dI(t)}{dt} \tag{2.3.8}$$

where L is the *inductance* of the inductor. The impedance of the inductor is then given as

$$Z_{\text{Inductor}} = i\omega L \tag{2.3.9}$$

where ω is the oscillation frequency of the applied voltage, and i is the imaginary unit.

2.3.3 Impedance Sweeps and Modelling

In an impedance sweep, the complex impedance of a system is measured over a large range of frequencies. If the real and imaginary parts of the impedance are plotted against one another, with the real part laying on the x-axis and the imaginary part on the y-axis, a *Nyquist Plot* is created. Figure 2.4 shows an example of such a plot, with two distinct semicircles being visible. For a solid ionic conductor, the half circles that appear in the typical frequency range of $1\,\mathrm{MHz}$ to $0.1\,\mathrm{Hz}$ can be attributed to physical processes such as bulk, grain-boundary or electrode conductivities. The impedance spectrum can then be fitted to an appropriate electrical circuit containing various sub-circuits that would mimic the electric response of the spectrum.
Figure 2.5 shows a sub-circuit consisting of a resistor and a capacitor in parallel. One such sub-circuit can be fitted to mimic the response of one of the half-circles in figure2.4. Due to the frequency dependency on the impedance of the capacitor (Equation 2.3.7), the RQ circuit will have an effective frequency range where it will have a net contribution to the impedance. Outside this range the contribution will be negligible. This translates into a time constant for the RQ circuit which can be translated into the time domain of a physical process.
Effectively, the sub-circuits will represent different physical processes and can be used to estimate the impedances of the various processes taking place, and hence estimate, for instance, ionic conductivity through a compound.

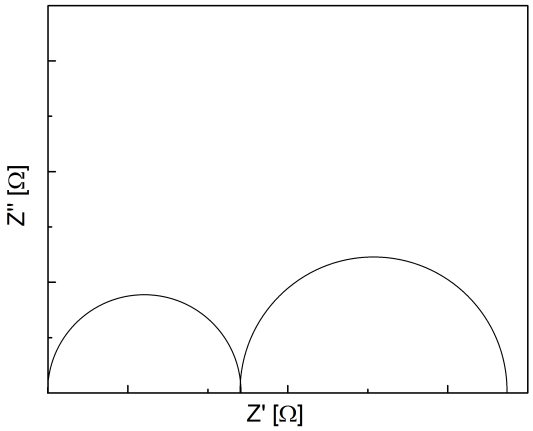

Figure 2.4: Nyquist plot with the imaginary part of the complex impedance *versus* the real part of the complex impedance. The spectrum shows two distinct half circles.

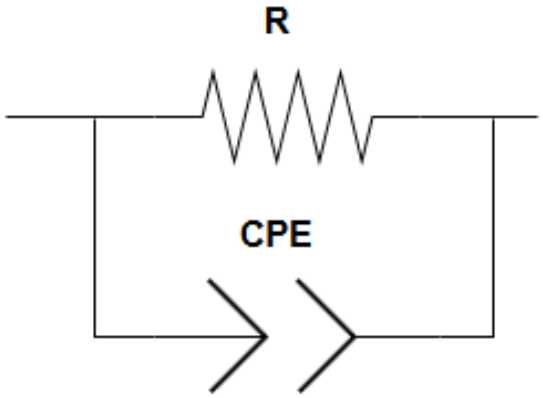

Figure 2.5: Parallel circuit showing a resistor and a constant phase element in parallel; an RQ circuit.

In practice, the half circles are likely to be depressed due to grain geometry and ori-

entation, and a pure capacitor will in many cases not give a proper fit of the spectrum. In these cases, the capacitor can be switched out for a *Constant Phase Element* (CPE), which has a more complex impedance than a pure capacitor. The impedance of a CPE includes a variable n, which is an exponent varying from -1 to 1, with the two limiting cases causing the impedance to reduce to that of an ideal inductor or an ideal capacitor for -1 and 1, respectively. For $n \to 0$, the impedance of the CPE reduces to an ideal resistor. n is estimated by the software used for fitting the spectrum, and the true capacitance C of the CPE is given by

$$C = \frac{1}{R\omega_0} = Q^{\frac{1}{n}} \cdot R^{\frac{1}{n}-1} \tag{2.3.10}$$

where Q is the estimated value of the CPE capacitance, R is the resistance of the resistor in parallel with the CPE, and n is the CPE-specific exponent.

Calculation of Conductivity from Fitting Parameters

Once an impedance spectrum has been modelled with an appropriate electrical circuit and the parameters of the circuit have been fitted to coincide with the spectrum, the calculated resistances can be translated into conductivities for the various processes. When investigating how ionic species travel through a solid compound, two important phenomena are the bulk and grain-boundary conductivities. The conductivities are material specific, and be estimated with the conductance (The ease of movement for a current through a conductor) and the geometry of the sample. Conductance and resistance are related by a simple relation

$$G = \frac{1}{R} \tag{2.3.11}$$

where G is the conductance, and R is the resistance. The units of conductance is Siemens.

Both bulk and grain-boundary resistances can be extracted from the RQ sub-circuits (Figure 2.5) with time constants such that the CPE is in the range of 1 to $100\,\mathrm{pF}$ for bulk and 1 to $100\,\mathrm{nF}$ for grain-boundary. The conductances can be calculated according to equation 2.3.11. In the case of bulk conductivity, the specific conductance, or conductivity σ (With units $\mathrm{S\,m^{-1}}$), can be found by correcting for sample geometry according to $\sigma = G \cdot \frac{l}{A}$ where l is the thickness of the sample and A is the electrode area. For grain-boundary conductivities, a similar method can be used using the brick-layer model. In this model, it is assumed that the grains are tightly packed together. Under the assumption that the grain-boundaries have the same relative dielectric constant as the bulk, and by knowing the average grain size, an effective grain-boundary thickness can

be calculated, from which the specific conductivity can be estimated.
Additionally, the empirical relation $\sigma_{\text{Measured}} = \sigma \cdot \rho_{\text{rel}}^2$ where ρ_{rel} is the relative density of the sample, is known as Archie's Law [37] and can be used to give a reasonable correction for sample porosity [34]. In the case of a sample having a high porosity, a natural question to ask would be how to be certain if the resistance measured actually belongs to the sample and not the atmosphere that infiltrates the porous structure. To determine this, it is possible to calculate the relative permittivity of the various processes based on the specific capacitances of the processes. Should the calculated permittivity exceed the value of of air (1), it is safe to conclude that the conductivity represents the sample itself. For bulk, equation 2.3.12 relates the specific capacitance to the relative permittivity and the porosity [38].

$$C_{\text{Bulk}} = \rho_{\text{rel}}^2 \cdot \epsilon_{\text{Bulk,rel}} \cdot \epsilon_0 \cdot \frac{A}{l} \tag{2.3.12}$$

where $\epsilon_{\text{Bulk,rel}}$ is the relative permittivity of the bulk process and ϵ_0 is the permittivity of free space. For the grain-boundary, an extra factor $d_{\text{g}}/\delta_{\text{gb}}$ is added to the equation. Here, d_{g} denotes the averaged grain size and δ_{gb} is the averaged grain-boundary thickness.
It is important to be careful when performing corrections for porosity, as when the relative densities go below $75\,\%$, the typical correction models start to lose their validity [39] and will in the range 45 to $60\,\%$ converge towards 0. For samples of high porosity, as might be the case for some samples in this project, the simple models can not provide adequate corrections for the conductivities and will therefore not be used to correct should the porosity fall below $70\,\%$.
Following the specific capacitance in equation 2.3.12, the relative permittivity can be incorporated into the equation for conductivity such as equation 2.3.13 and 2.3.14 for bulk and grain-boundary, respectively.

$$\sigma_{\text{Bulk}} = \frac{\epsilon_{\text{Bulk,rel}} \cdot \epsilon_0}{R_{\text{Bulk}} \cdot C_{\text{Bulk}}} = \frac{l}{R_{\text{Bulk}} \cdot A \cdot \rho_{\text{rel}}^2} \tag{2.3.13}$$

$$\sigma_{\text{gb}} = \frac{\epsilon_{\text{gb,rel}} \cdot \epsilon_0}{R_{\text{gb}} \cdot C_{\text{gb}}} = \frac{l \cdot d_{\text{gb}}}{R_{\text{gb}} \cdot A \cdot \rho_{\text{rel}}^2 \cdot \delta_{\text{gb}}} \tag{2.3.14}$$

Chapter 3

Literature Review

3.1 Ionic Conduction in Oxoacid Salts

An oxoacid is an acid that contains oxygen. Phosphoric acid H_3PO_4 and silicic acid H_4SiO_4 are two examples of oxoacids. In this project, work will be done on oxoacid compounds where the cations are alkali and alkaline earth metals, otherwise known as oxoacid salts [40]. The compounds of interest, like $KBaPO_4$ and $NaCaHSiO_4$, contain anionic units that are of a tetrahedral molecular geometry, and it has been suggested that these tetrahedral units are essential for the ionic conductivity in these types of salts. For example, Rong Yu performed DFT calculations on $LaPO_4$ where the result was that intertetrahedral (Jumps between tetrahedral anions) transfer gave the greatest contribution to overall proton conductivity [41]. Lithium sulphates have been suggested to have a superionic phase where a "paddle-wheel" mechanism, meaning that the tetrahedron rotates, facilitates the movement of Li-ions through the structure [42]. CsH_2PO_4, on the other hand, is suggested to have a superionic state caused by partial thermal decomposition where the proton migration occurs from oxygen to oxygen by reorientation of the OH-groups followed by subsequent breaking and formation of the hydrogen bond [43, 44].

3.2 $KBaPO_4$

The literature concerning the compound $KBaPO_4$ and its properties is mostly limited to chemical preparation and crystal structure refinement and characterization. In 1941 its orthorhombic crystal and corresponding lattice parameters were reported by Klement & Uffelmann [32]. In 1961, Klement & Kresse reported that $KBaPO_4$ has a low-temperature and a high-temperature phase, with the transition occuring around 1050°C [45]. The low-temperature phase has been characterized and refined, and the cystal structure is reported to be orthorhombic with lattice parameters $a = 5.66 \pm 0.005$, $b = 9.959 \pm 0.010$ and $c = 7.697 \pm 0.008$ Å [32, 46]. It is isostructural to the orthorhombic β-K_2SO_4, commonly known as arcanite, with the potassium and barium being, respectively, 10- and 9-coordinated with respect to oxygen. The high-temperature phase is not as well documented, however it was reported by Klement & Kresse to be isostructural to the trigonal glaserite ($K_3Na(SO_4)_2$) structure with the lattice parameters $a = b = 5.80$ and $c = 8.15$ Å.

Regarding other physical properties of $KBaPO_4$, Goodenough & Singh reported, in 2015, the discovery that $KBaPO_4$ (Which they refer to as $BaKPO_4$) can be hydrated by exposing the crystalline solid to water vapour at $80\,^{\circ}\mathrm{C}$, and that this would result in a *water-solvated glass/amorphous solid* H^+ *electrolyte/dielectric* displaying a significant protonic conductivity of $\sigma_H \approx 10^{-2}\ \mathrm{S\,cm^{-1}}$ at just below $100\,^{\circ}\mathrm{C}$ [4]. This is the only piece of literature in which the electrical properties of $KBaPO_4$ have been attempted characterized.

3.2.1 Synthesis

Multiple methods have been utilized to synthesize $KBaPO_4$. When they characterized the low-temperature phase of $KBaPO_4$ in 1961, Struck & White mixed KNO_3 or K_2CO_3 with $BaHPO_4$ and fired in an inert atmosphere of N_2 at temperatures between 900 to $1200\,^{\circ}\mathrm{C}$, for durations of 3-24 hours [47]. Masse & Durif refined the crystal structure of $KBaPO_4$ in 1987 by growing single crystals of $KBaPO_4$ at $650\,^{\circ}\mathrm{C}$ through mixing stoichiometric amounts of either K_3PO_4 or $K_4P_2O_7$ with BaF_2. The simplest method was utilized by Klement & Kresse in 1961 when they characterized multiple alkali- and alkaline earth oxoacid compounds of composition $M^{I}M^{II}X^{V}O_4$. They mixed $BaHPO_4$ with K_2CO_3 and calcined the mixture at $1000\,^{\circ}\mathrm{C}$ for a few hours to obtain $KBaPO_4$ [45]. A similar high-temperature synthesis route was selected for this project.
It might be worth mentioning that, in 1998, Iwahara et al. were investigating the possibility of K-doping $Ba_3(PO_4)_2$ in order to improve the ionic conductivity of the compound [6]. They synthesized their goal product $Ba_{3(1-x)}K_{3x}(PO_4)_{2-x}$ by mixing $BaHPO_4$, $BaCO_3$ and K_3PO_4 followed by calcination at $1050\,^{\circ}\mathrm{C}$ for 15 hours. As a result of their process, they found that when increasing the K-content above $x = 0.050$ ($5\,\mathrm{mol\,\%}$) diffraction lines for $KBaPO_4$ begun to appear in their XRD patterns, suggesting that the saturation limit of potassium in $Ba_3(PO_4)_2$ is below $5\,\mathrm{mol\,\%}$, but also providing yet another route to synthesize $KBaPO_4$, although the method would not give a large nor pure yield of $KBaPO_4$.

3.2.2 Acceptor Doping $KBaPO_4$

In parallel to this project, Kevin Nguyen investigated the possibility of acceptor-doping $KBaPO_4$ with excess potassium in order to increase the conductivity of the compound [48]. Some of the results obtained by Nguyen are worth mentioning here to facilitate the understanding of the conductivity taking place in $KBaPO_4$. The formula of the acceptor doped compound is $K_{1+x}Ba_{1-x}PO_{4-\delta}$, and the excess potassium is assumed, based on results, to be compensated by $K_i^{\cdot}$ as resulting from the predominating Frenkel

defects that were previously discussed when introducing a defect model for $KBaPO_4$ in section 2.2.2. Nguyen found that the compound had an increased conductivity as compared to single-phase $KBaPO_4$ ($1 \times 10^{-4}\,\mathrm{S\,cm^{-1}}$ at $700\,^{\circ}\mathrm{C}$) and with similar activation energies as for $KBaPO_4$, however no effect with regards to humidity or pO_2 was observed. As will be clear by the end of this thesis, the results from single-phase $KBaPO_4$ and the results from $K_{1.01}Ba_{0.99}PO_4$ by Nguyen will strengthen the assumption that Frenkel defects are the predominating defects in $KBaPO_4$, and that it is not a protonic conductor.

3.3 Orthosilicates

3.3.1 $NaCaHSiO_4$ and Related Compounds

As the goal of this project was to discover and characterize new ionic conductors, inspiration was drawn from cesium-containing compounds that exhibit protonic conductivity and transitions into so-called superprotonic phases. Compounds like CsH_2PO_4 [43, 44], $CsHSO_4$ and $Rb_3H(SeO_4)_2$ [2].

Sossinha M. Haile presented in 2005 a report that included the results of electrical measurements performed on $NaCaHSiO_4$ [25]. The compound was synthesized by a hydrothermal method in which NaOH, $Ca(OH)_2$ and SiO_2 were placed in a 3:2:2 molar ratio in a thermal bomb and held at $250\,^{\circ}\mathrm{C}$ for 72 hours. The conductivity of $NaCaHSiO_4$ was found, through measurements performed in an argon atmosphere, to be dominated by its grain boundary properties, with larger grained polycrystalline samples resulting in overall higher conductivities. In 2008, Haile et al. published a patent application publication in which the decomposition temperature of $NaCaHSiO_4$ was found to be somewhere just above $400\,^{\circ}\mathrm{C}$, and that its stability in a reducing hydrogen atmosphere was significantly better than for $CsHSO_4$ [26], and that it could possibly be effective in fuel cells.

One of the goals of the this project was to reproduce $NaCaHSiO_4$ according to the hydrothermal method utilized in the report (Originally used by Cooksley and Taylor when they characterized the monoclinic structure of $NaCaHSiO_4$ [49]), and perform conductivity measurements in dry and humidified atmospheres, as well as investigate its reaction towards an atmosphere humidified by D_2O instead of H_2O. In addition, a defect model will be proposed for the compound.

Based on the existence of $NaCaHSiO_4$, and the lack of documentation regarding similar compounds, it was decided to investigate whether or not similar alkali and alkaline earth orthoanionic compounds $ABHXO_4$ (A=Li, Na or K. B=Ca, Sr or Ba. X=Si, Ge or Sn)

could be synthesized by the same method. If so, these products were to be further investigated by electrical measurements to determine whether or not they could be applied as ionic conductors.

3.3.2 BaH_2SiO_4

G. Kruger and W. Wieker synthesized and characterized BaH_2SiO_4 in 1965 [50]. They synthesized the compound according to a precipitation method in which NaOH and Na_2SiO_3 were dissolved in hot deionized water and precipitated by the addition of $BaCl_2$. This method results in the precipitation of amorphous barium silicates, and transforming these into crystalline species depends on solution concentrations, temperatures during precipitation and the time during which the temperatures are maintained. This method was utilized by Haile et al. in order to synthesize BaH_2SiO_4 on which electrical measurements were conducted [26].
Separately, Fälth and Annehed discovered that a hydrothermal approach, in which SiO_2 and BaOH were mixed in a 1:1 molar ratio and heated in a thermal bomb at $160\,^{\circ}\mathrm{C}$ for several hours, yielded a crystalline product that they found to be identical to the BaH_2SiO_4 phase as reported by Kruger and Wieker [51]. They further went on to characterize the crystal structure of BaH_2SiO_4 and found it to have a triclinic structure with the lattice parameters $a = 7.0793$, $b = 7.3585$ and $c = 7.5814$ Å.
In the patent by Haile et al. [26], electrical measurements were performed on BaH_2SiO_4 as synthesized by the precipitation method provided by Kruger and Wieker. The conductivity of BaH_2SiO_4 was found to range between 10^{-8} and $10^{-7}\mathrm{S\,cm^{-1}}$ at temperatures between 250 to $350\,^{\circ}\mathrm{C}$. However, there is a discrepancy due to the patent mentioning that BaH_2SiO_4 decomposes around $320\,^{\circ}\mathrm{C}$, whereas the conductivity plot indicates that measurements were performed on BaH_2SiO_4 above the temperature at which it should decompose. Could the this be a result of an increased stability due to impurities in the synthesized and measured sample?
The BaH_2SiO_4 as synthesized by the hydrothermal method by Fälth and Annehed has not been electrically characterized. However, the product from this synthesis was found to be very pure. Based on this, and the initial goal of this project being the investigation of ionic conductivity in various oxoacid salts, it was decided to include BaH_2SiO_4 in this project, with the goal being to synthesize a pure BaH_2SiO_4 phase according to the hydrothermal method provided by Fälth and Annehed, followed by subsequent electrical measurements in order to confirm or disprove the results provided by Haile et al. Additionally, a defect model will be proposed for the compound.

Chapter 4

Experimental

4.1 Sample Preparation

4.1.1 Synthesis

All products synthesized were analysed by XRD in order to determine if the desired product had been obtained.

Solid State - Combustion Synthesis

To synthesize $KBaPO_4$, the route proposed by Klement & Kresse was utilized [45]. $BaCO_3$ ($99.98\,\%$, Sigma Aldrich) was mixed with KH_2PO_4 (>$99.5\,\%$, Merck) in a 1:1 molar ratio. The reactants were mixed in an agate vial, and agate balls were added in a single layer above the powder, giving a ball to powder weight ratio of 34:2.5. Subsequently, isopropanol was added to the vial until the balls were submerged, and the vial was installed in a ball mill (Retsch Planetary Ball Mill PM 100) and milled at 250RPM for 1 hour to obtain an even mix of reactants. The mixture was then dried in a glass beaker at $110\,^{\circ}\mathrm{C}$ in a heating cabinet to evaporate the isopropanol, followed by calcination in an alumina crucible at $1000\,^{\circ}\mathrm{C}$ for 6 hours in a muffle furnace.

Hydrothermal

A hydrothermal approach was utilized in order to synthesize the orthosilicates that were used in this project. For the synthesis, a teflon vial of approximately $19\,\mathrm{ml}$ was filled so that the amount of water gave an approximate filling degree of $80\,\%$. The teflon vial was installed in an autoclave which was then sealed and placed in a heating cabinet that allowed for temperatures up to $400\,^{\circ}\mathrm{C}$. After the synthesis in the autoclave, the obtained product was poured into a Büchner funnel connected to an aspirator and washed multiple times with purified (Type I) water before being subsequently dried on a watchglass in a heating cabinet at $110\,^{\circ}\mathrm{C}$ for 1 hour. Table 4.1 contains information on the purities and the manufacturer of the reactants used for the various syntheses.

Table 4.1: Information (Trace metal %, producer) on the alkali and alkaline earth hydroxides used for the hydrothermal synthesis of $NaCaHSiO_4$, BaH_2SiO_4, and the various compounds $ABHXO_4$ (A=Li, Na or K. B=Ca, Sr or Ba. X=Si, Ge or Sn).

Compound	Purity %	Producer
$LiOH \cdot H_2O$	>99.0	Fluka Chemika
NaOH	>99.0	Merck
KOH	>90	Sigma-Aldrich
$Ca(OH)_2$	>96	Merck
$Sr(OH)_2$	>95	Sigma-Aldrich
$Ba(OH)_2$	>98	Sigma-Aldrich
SiO_2	NA	Sigma-Aldrich
GeO_2	>99.99	Sigma-Aldrich
SnO_2	>99.9	Alfa Aesar

$NaCaHSiO_4$ and multiple other compounds with the chemical composition $ABHXO_4$ (A=Li, Na or K. B=Ca, Sr or Ba. X=Si, Ge or Sn) were attempted synthesized. Group 14 oxides (SiO_2, GeO_2 or SnO_2) were mixed with the alkali and alkaline earth hydroxides (e.g. NaOH and $Ca(OH)_2$) in a 1:1:1 molar ratio in the teflon vial and water was added to obtain a filling degree of 80 %. The autoclave was then put in the heating cabinet at 250 °C and left for a duration of 72 hours. The product was subsequently treated in the manner described above.

BaH_2SiO_4 was synthesized according to the method described in [51, 52]. Fumed silica (0.007 µm, Sigma-Aldrich) was mixed with NaOH and $Ba(OH)_2 \cdot 8H_2O$, in a 1:1:1 molar ratio in the teflon vial and water was added to obtain a filling degree of 80 %. The autoclave was then put in the heating cabinet at 150 °C and left for a duration of 18 hours. The product was subsequently treated in the manner described above.

Mechanochemical Synthesis

A mechanochemical approach, in which the reactants are subjected to high mechanical energies at room temperature, was utilized in order to investigate whether or not $KBaPO_4$ could be synthesized by such a method. The method is further described in [53].

Similarly to the high temperature combustion method described in section 4.1.1, a planetary ball mill was utilized for the mechanochemical method. $BaCO_3$ was mixed with

KH_2PO_4 in a 1:1 molar ratio. The reactants were mixed in an agate vial, and agate balls were added in a single layer above the powder, giving a ball to powder weight ratio of 34:2.5. Two different synthesis environments were utilized:

1. A dry environment in which there was only dry powder. No water. No isopropanol.
2. A wet environment in which isopropanol was added until the balls were submerged.

Subsequently, the agate vial was installed in the ball mill, and was set to operate at 450RPM for 24 hours, with there being a 5 minute break-interval at the 12 hour mark followed by a change in the direction of rotation. After milling, the collection method varied between the used environments:

1. Dry: The product was scraped out of the vial with a plastic spatula and stored in a sample bottle.
2. Wet: The product was dried in a glass beaker at $110\,^{\circ}\mathrm{C}$ in a heating cabinet to evaporate the isopropanol. The product was then stored in a sample bottle.

The products were then investigated by XRD.

4.1.2 Pellet Preparation

Pellets were pressed using an *Atlas Series Manual Hydraulic Press* manufactured by Specac. The die sizes used were 13, 10 and $6\,\mathrm{mm}$, with the applied pressure ranging from 130 to $170\,\mathrm{MPa}$. Post-pressing, the samples were attempted sintered in a muffle furnace at temperatures lower than the compounds' melting and decomposition temperatures (Typically $\frac{2}{3}T_m$ if possible). In cases where the sample could not be sintered, electrodes were painted on directly after pressing. Post-sintering, the pellets were prepared for impedance spectroscopy by painting on electrodes with either silver or platinum ink for low and high temperature measurements, respectively. For the samples with silver, two layers were applied before firing the electrode in a muffle furnace, whereas for the platinum three layers were applied. The samples made and their respective sintering/electrode-firing temperatures can be seen in Table 4.2. The geometrical details of all the samples on which electrical measurements were conducted can be found in Table 4.3

Table 4.2: Details of the sintering program and the program for firing the electrode for all samples made on which electrical measurements were conducted.

Compound	Sintering		Electrode	
	T [°C]	Duration [h]	Ag/Pt	Firing T [°C]
$KBaPO_4$	1000	8	Pt	900
$Ba_3(PO_4)_2$	1000	8	Pt	900
K-$Ba_3(PO_4)_2$	NA	NA	Ag	NA
Two-phase*	1100	8	Pt	900
$NaCaHSiO_4$	400	24	Ag	400
BaH_2SiO_4	250	24	Ag	250

*Two-phase system of $Ba_3(PO_4)_2$ and $KBaPO_4$

Table 4.3: Details (Sample and electrode geometries, mass, relative densities) of all samples on which electrical measurements were conducted. l is the sample thickness, d is the diameter of the sample, d_{el} is the diameter of the electrode, and m is the sample mass. The uncertainty in the relative density is calculated based on sample dimensions and mass.

Sample	Sample Geometry [mm]			Mass [g]	Relative Density
	l $\delta = \pm 0.01$	d $\delta = \pm 0.01$	d_{el} $\delta = \pm 0.01$	m $\delta = \pm 0.0001$	ρ_{rel}
$KBaPO_4$	2.87	12.68	5.75	1.0933	$0.73 \pm 1\%$
$Ba_3(PO_4)_2$	2.90	9.74	2.40	0.7970	$0.70 \pm 1\%$
K-$Ba_3(PO_4)_2$	1.70	10.00	9.5	0.3900	0.75
Two-phase*	2.35	12.07	5.41	1.1101	0.79
$NaCaHSiO_4$	1.68	6.00	6.00	0.0865	$0.66 \pm 1\%$
BaH_2SiO_4	2.16	10.00	5.35	0.4698	$0.71 \pm 1\%$

*Two-phase system of $Ba_3(PO_4)_2$ and $KBaPO_4$

4.2 Characterization

4.2.1 X-Ray Diffraction - XRD

In order to study the phase-composition of the various synthesized samples, X-Ray diffractograms were obtained by the means of X-Ray Diffraction. For measurements on pellets, the pellet was simply placed in a deep holder and adjusted to keep level across the surface. For powder-samples, glass holders were used. Some powder is mixed in a mortar and a slight amount of isopropanol is added. For investigating potential doping by peak-shift, a silicon standard (NIST 640D) is added to the mixture in 1:2 Si:Sample-volume ratio. The mixture is then dripped by pipette onto a glass holder and

the holder is tilted in order to obtain an even spread. Subsequently, the isopropanol is evaporated in air and a uniform film is left on the holder. Another method is to paint a thin layer of vacuum-grease onto the middle of the holder and pouring some mortared powder on top, proceeded by knocking the holder on the table to get rid of excess powder to avoid height-errors. This method requires less powder and prevents any potential reaction that could otherwise occur with isopropanol.

The instrument employed for this analysis was the *MiniFlex 600 Benchtop XRD* from Rigaku Corporation. The instrument was without a monochromator so both $Cu_{\alpha 1}$ ($1.5406\,\text{Å}$) and $Cu_{\alpha 2}$ ($1.5444\,\text{Å}$) were present, resulting in a slight splitting of the peaks at high values of 2θ. The scanning range was from 10 to $90°$ with a step size of $\Delta 2\theta = 0.1°$. The typical duration of a scan was 90 minutes. The data was processed with DIFFRAC.EVA (Bruker), in which the patterns were compared with the Powder Diffraction File (PDF) database by the International Centre for Diffraction Data (ICDD) in order to determine purity of products and whether or not unwanted phases were present.

4.2.2 Scanning Electron Microscopy - SEM

A *Quanta 200 FEG-ESEM* electron microscope produced by FEI was utilize in order to study the microstructure and the topography of the samples, as well as phase composition by EDS. A high-energy electron beam produced by a field emission gun (FEG) scans the surface of the sample, exciting the atoms and giving rise to multiple signals, including backscattered electrons (BSE), secondary electrons (SE) and X-Rays. SE are low-energy electrons that are detected by an Everhart-Thornley and giving an image of the surface of the sample. The BSE give rise to an image where the brightness of an area is determined by the atomic number of the species present, and was utilized in order to quickly determine whether or not a sample was homogenous (i.e. all areas equally bright) or not.

A high vacuum atmosphere was used and an acceleration voltage of 15 to $25\,\text{kV}$ was typically used to examine the samples. Both SE and BSE signals were used in order to determine if sintering processes were successful, as well as investigating how some samples had chemically decomposed after some experiments. $25\,\text{kV}$ was typically used when performing EDS-analysis of chemical composition, as described in the next section. In some cases ESEM mode (Environmental SEM, allows for low-pressure gaseous environments in the chamber) was used due to some samples being highly insulating and accumulating negative charge on the surface giving rise to charging artifacts on the

collected images. In these cases, water vapour was introduced in a low-pressure environment, allowing for the accumulated charge to migrate away from the surface and hence improving the quality of the images.

4.2.3 Energy Dispersive X-Ray Spectroscopy - EDS

In order to study the phase composition of the samples, an Energy Dispersive X-Ray Spectrometer (EDS) of the type *EDAX Pegasus 2200* produced by EDAX, an attachment to the SEM, was utilized. The incident electron beam causes electrons in the atomic shells to be excited. When these electrons fall back to the ground state, X-Rays are created, the energies of which are unique to the different energy levels of the atoms, and can therefore be collected to give a quantitative mapping of the elemental composition of the sample. However, some atoms have multiple energy levels, giving an overlap in the mapping, resulting in a decrease in the accuracy of the analysis. Despite this, the method is suitable for the characterization purposes of this project and to obtain an adequate chemical composition we can average over scans from multiple areas. EDS was used in this project to analyse various samples in order to determine homogenousity and changes in chemical compositions.

4.2.4 Thermogravimetric Analysis - TGA

For some compounds, thermogravimetric analysis was employed to study decomposition reactions when heated in air, and stability in high water vapour pressures. For the decomposition reactions, a *STA 449 F1 Jupiter* was utilized, whereas the stability in high water vapour pressures was studied in a *STA 449 C Jupiter* equipped with a water vapour generator allowing for water vapour pressures ranging from 0.1 to $1\,\mathrm{atm}$. Both instruments are manufactured by Netsch.

4.3 Impedance Spectroscopy

4.3.1 Setup

Default Setup

The default setup for the impedance (IS) measurements consists of a ProboStat™, manufactured by NorECs, connected to a gas mixer. In the ProboStat (Figure 4.1), the sample is placed between two Pt electrodes, supported by an inner, open alumina tube, fastened by a spring load alumina assembly. The entire setup is covered by a bigger,

open alumina tube which is connected to the stainless steel base, effectively sealing the setup, allowing the user to introduce the desired atmosphere. The temperature inside the cell is measured with an S-type thermocouple that is positioned next to the sample, connected to a temperature controller that is used to regulate the temperature of the external tubular furnace in which the ProboStat is finally installed into.

The atmosphere within the ProboStat cell is controlled by a simple gas mixer (Figure 4.2). Essentially, for this project, the gas mixer allowed for the flow of normal air ($pO_2 \approx 0.21\,\mathrm{atm}$), pure O_2 or pure Ar, directed through either a humidifying stage (Containing a saturated solution of KBr; $pH_2O \approx 0.025\,\mathrm{atm}$ [54]) or a drying stage (Containing P_2O_5(s), yielding around 30 ppm of H_2O in the gas [55]) and into the cell itself.

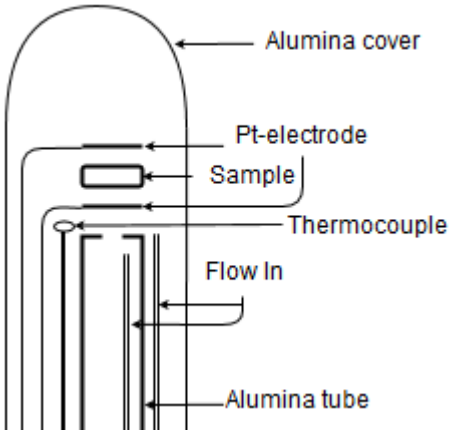

Figure 4.1: Schematic view of the interior of the ProboStat measurement cell.

High-Humidity (Steam) Setup

The setup used for the high-humidity measurements is, essentially, the same as the default setup. However, due to the requirements of a high water vapour pressure (steam) at 80°C (Giving a water vapour pressure of $pH_2O \approx 0.47\,\mathrm{atm}$.), the setup had to be heated to a temperature slightly above that of the steam supply. This modified setup is shown in figure 4.3. A special ProboStat that allows the base to be heated was utilized. A water basin that could be heated was used to accurately supply steam at temperatures up to 80°C. From the water basin, the tubing was wrapped in heating tape and insulated with a glass fiber band, all the way to the base of the ProboStat cell. An S-type thermocouple was placed between the tubing and the heating tape in order to regulate the temperature

with a temperature controller. To heat the cell precisely, a heating mantel was utilized, and the temperature was controlled by a temperature controller connected to the S-type thermocouple placed inside the ProboStat.

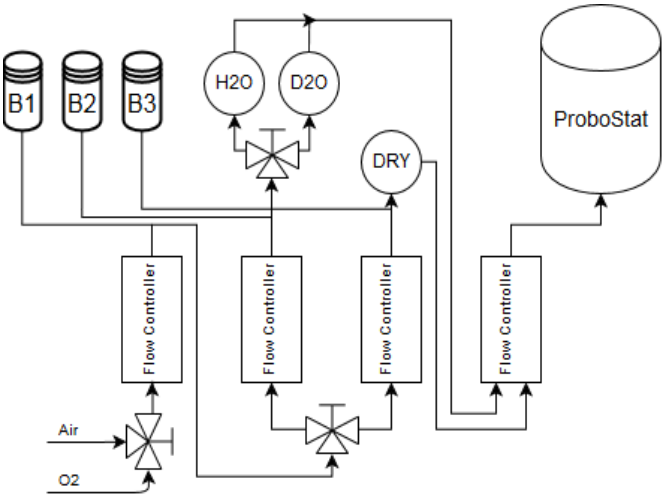

Figure 4.2: Schematic view of the simple gas mixer setup used for controlling the atmosphere inside the ProboStat measurement cell. Air or O_2 is flowed through a humidifier (H_2O or D_2O) or a dryer before flowing into the cell. B1-B3 represent bubblers filled with mineral oil to regulate overpressure and prevent back-mixing of the gas.

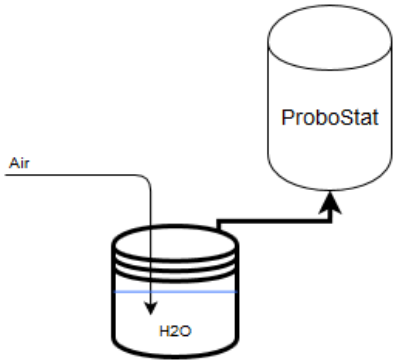

Figure 4.3: Schematic view of the modified setup for supplying a high water vapour pressure to the ProboStat measurement cell. Bold lines signify that the component can be heated.

4.3.2 Electrical Measurements

The impedance measurements were conducted with a Solartron Instruments 1260 Impedance/Gain-phase analyser, connected to the ProboStat through a multiplexer. The software used to perform the measurements was the Omega 2 software supplied by NorECs. The impedance spectra were recorded with 100 measurement points evenly dispersed within the frequency range of $1\,\mathrm{MHz}$ to $1\,\mathrm{Hz}$, with an oscillation voltage of $3\,\mathrm{V}$ RMS to minimize noise, at selected temperatures below the decomposition/melting temperatures of the samples. Spectra were recorded when the system had reached equilibrium, determined by continuously measuring the impedance at $10\,\mathrm{kHz}$ and observing when the change in impedance reached a minimum.

Analysis of Measurement Data

Following data collection, the recorded impedance spectra were analysed using ZView (version 3.5a, Schribner Associates Inc.) and the spectra were fitted to correspond with appropriately defined equivalent circuits, an example of which is shown in figure 4.4.

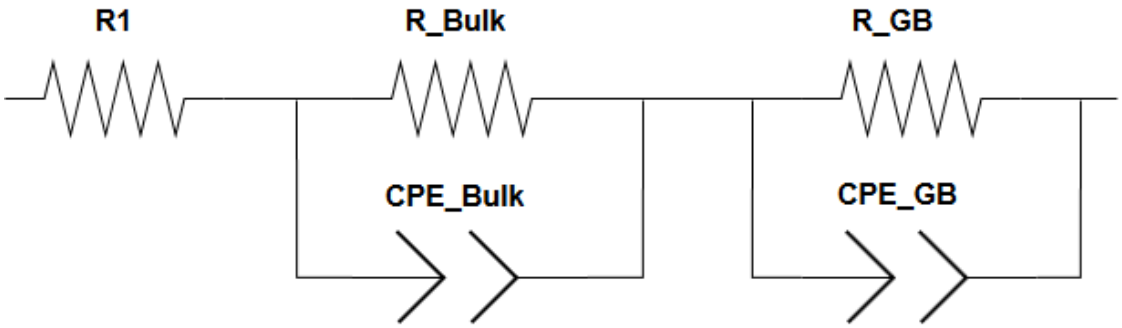

Figure 4.4: Equivalent circuit used for fitting collected impedance spectra. R1 is the ohmic contribution from the wiring and the electrode spreading resistance, the Bulk and GB segments represent the Bulk and Grain-Boundary, respectively.

Following data collection and modelling of spectra, the obtained values for resistance were used to calculate the specific conductivities of the various physical processes according to equation 4.3.1.

$$\sigma_{\text{Process}} = \frac{l}{A \cdot R_{\text{Process}}} \tag{4.3.1}$$

where l is the sample thickness, A is the area of the electrode, and R_{Process} is the value for resistance as obtained by impedance spectroscopy and subsequent spectrum analysis. The specific conductivity has the units $\mathrm{S\,cm^{-1}}$. An explanation of the expression is given in section 2.3.3.

4.4 Other Experimental Methods

4.4.1 Hydration of $KBaPO_4$

$KBaPO_4$ was subjected to liquid water to in order to study its stability and potential hydration. A pellet of KBaPO4 was prepared in the manner previously described (Without electrodes) and installed in the High-Humidity ProboStat setup. It was subjected to steam at $80\,^{\circ}\mathrm{C}$ for 24 hours. The sample was then broken into two pieces, with one piece being reinstalled in the ProboStat setup for further steaming, and the other half being submerged in a sample bottle filled with purified (Type I) water and left at room

temperature. Both pieces were left in their respective setups for a duration of 48 hours before being removed and analysed.

4.5 Sources of Error

There are multiple sources of errors associated with the experimental methods used in this project. Examples include; contamination during synthesis, temperature gradients in muffle furnaces during calcination and sintering, and contamination during the pellet pressing process post-calcination. These errors were reduced by carefully cleaning equipment before use and keeping the samples stored in sealed containers. The samples were placed in the middle of the furnace to minimize the effect of a possible temperature gradient.

The characterization methods used have errors in both the data collecting process and the subsequent analytical step in which external software is used. For EDS, the phase composition can not accurately be determined due to the many factors (peak overlap, interaction volume size, drift during measurement, etc...) that are included, however an adequate estimation can be made by performing scans on multiple areas of the sample.

For the impedance measurements and subsequent data-analysis to calculate conductivities and activation energies, there are multiple error sources that need to be considered through all the steps in process of obtaining and analysing data. The following list contains some sources of error, and how they have been corrected for.

- **Error in Measurement of Sample Geometry, Porosity and Temperature:** A digital caliper was utilized to measure the thickness and diameter of the samples. The documented uncertainty of the caliper is $0.01\,\mathrm{mm}$. The mass was determined by an electronic laboratory balance with a documented uncertainty of $0.1\,\mathrm{mg}$. The mass of the sample is used to correct for sample porosity by the empirical formula $\sigma_{\text{measured}} = \sigma \cdot \rho_{\text{rel}}^2$ [34] (Giving reasonable corrections for fairly low porosities). The uncertainty in the relative density (Used for correcting for porosity) is based on sample geometry and mass. Assuming that the documented uncertainty of the caliper is the absolute uncertainty for all the geometric measurements, i.e. considering sample thickness and sample/electrode dimensions to have the same uncertainty, then the thickness, being significantly lower than the other values, would, according equation 4.5.2, have a bigger impact on the uncertainty than any other measurements. Based on calculations, the term describing the uncertainty due to sample thickness will be approximately 100 times larger than the second largest

contribution, and equation 4.5.2 can be reduced to only take the sample thickness into consideration, as equation 4.5.3.
Due to thermocouple in the measurement cell being in close proximity to the sample, and being a relatively new S-type thermocouple, the uncertainty in the temperature was assumed to be a maximum of $2\,\mathrm{K}$[1].

- **Systematic Error During Impedance Measurement:** A systematic error occurs in the values obtained by the instrument used due to the inherent imperfection in the calibration of the instrument, and the instrument used has a documented accuracy of $0.1\,\%$.

  For samples with a low impedance, a problem with the impedance measurements arises when using a 2-wire setup, i.e. when the source and voltmeter work through the same wiring, is that the results would be heavily influenced by the impedance of the wiring. To prevent this, a 4-wire setup is used instead, where the voltmeter is connected in parallel to the source through different wires and draws a negligible current that effectively results in an insignificant contribution of the wiring and hence a very accurate measurement of the load impedance.

  For samples with very high impedance, there is a risk of conduction across the capacitance of the gas phase around the sample between wires that are close to one another, effectively giving rise to a parallel circuit where the impedance between the two wires will heavily influence the results. However, this would only occur should the impedance of the sample be gigantic, and should not be a problem for this project. Despite this, it has been accounted for by using shielded wiring outside of the cell, and by making sure the wiring inside the cell is distanced sufficiently from one another.

- **Uncertainty in Analysis and Fitting of Impedance Spectra:** The collected impedance spectra were analysed and modelled with an equivalent circuit consisting of an adequate number of (RQ) segments (Figure 4.4). This fitting yielded the resistances and capacitances required for further calculations. Due to the nature of the measurement and the equipment used, each point on the impedance curve would have a slight error, and the resulting fit would contain an error mathematically related to all of these individual errors, and would have an error itself that would slightly change with the number of points used for the fit and other fitting parameters. All the fits were made using the same fitting parameters (# of iterations, data-weighing, etc) and so the fits would contain the same systematic

[1]The thermocouple was not calibrated against a reference thermocouple before measurements were conducted, but it had only been used for a short period of time at moderate temperatures beforehand.

error. The fits were made to closely approximate the collected impedance spectra, but due to the nature of the error, it was subsequently assumed that the error of the resulting values for resistances and capacitances were negligible compared to the errors in the measurements and estimations of sample mass, sample geometry (e.g. thickness, diameter, relative density and porosity), electrode dimensions, and cell temperature. It was further approximated that the major contribution to the uncertainty would be the sample thickness, as seen in equation 4.5.3.

- **Propagation of Uncertainty During Calculations:** The calculated values for conductivities and activation energies will bring with them an uncertainty that arise from the uncertainties in the measurements in sample geometry and mass, and the cell temperature. Based on the statistical view on the propagation of error, the relative uncertainty for the calculated conductivity σ, when corrected for sample geometry is given as.

$$\frac{\delta\sigma}{\sigma} = \sqrt{(\frac{\delta l}{l})^2 + (2\frac{\delta d_{el}}{d_{el}})^2} \tag{4.5.1}$$

where δ denotes the uncertainty of the following parameter, and l and d_{el} represent, respectively, the thickness of the sample and the diameter of the electrode.

By correcting for porosity, by the empirical formula described above, the relative uncertainty for the conductivity σ, corrected for both sample geometry and porosity (i.e. relative density), is given as

$$\frac{\delta\sigma}{\sigma} = \sqrt{(3\frac{\delta l}{l})^2 + (4\frac{\delta d}{d})^2 + (2\frac{\delta d_{el}}{d_{el}})^2 + (2\frac{\delta m}{m})^2} \tag{4.5.2}$$

where the additional parameters d and m represent the diameter, and the mass, of the sample, respectively. In the derivation of the uncertainty in the calculated conductivity, included in appendix A.1, the resistance is considered to be accurate, i.e. without error.

By considering the relative sizes of the various terms in equation 4.5.2 for the samples made for this project, the biggest contribution would be from the measured sample thickness, and the equation would reduce to

$$\frac{\delta\sigma}{\sigma} = \sqrt{(3\frac{\delta l}{l})^2} \tag{4.5.3}$$

Additionally, the relative uncertainty of the activation energy E_a, based on $\ln \sigma T = \ln \sigma_0 - \frac{E_a}{k_B \cdot T}$, is given by

$$\frac{\delta E_a}{E_a} = \sqrt{(\frac{\delta T}{T})^2 + (\frac{\delta A}{A})^2} \tag{4.5.4}$$

where T is the cell temperature at the time of measurement and A is the slope value of the linear fit of $\ln \sigma T$ *vs* $\frac{1}{T}$. Considering the previous discussion of the uncertainty of the thermocouple used during the measurements ($\delta T = 2\,\mathrm{K}$, giving an uncertainty on the scale of $0.1\,\%$ above $300\,^\circ\mathrm{C}$), the estimated uncertainty of the slope value based on the linear regression will be the dominating term in the total uncertainty.

Chapter 5

Results

5.1 $KBaPO_4$

5.1.1 Synthesis & Characterization

$KBaPO_4$ was synthesized according to the solid state method proposed by Klement & Kresse [45], described in section 4.1.1, although it was decided that $BaHPO_4$ and K_2CO_3 could be replaced with $BaCO_3$ and KH_2PO_4, seeing as the reaction called for one carbonate and one phosphate. The product was found by XRD to consist of single-phase $KBaPO_4$ (Figure 5.1). The pellets prepared from the powder resulting from this synthesis had, post-sintering, a surface topography similar to the one shown in figure 5.2, with the elemental composition, determined by EDS, observed in figure 5.3. All pellets had a relative density of around 71 to 74 %, and all geometrical details can be found in table 4.3.

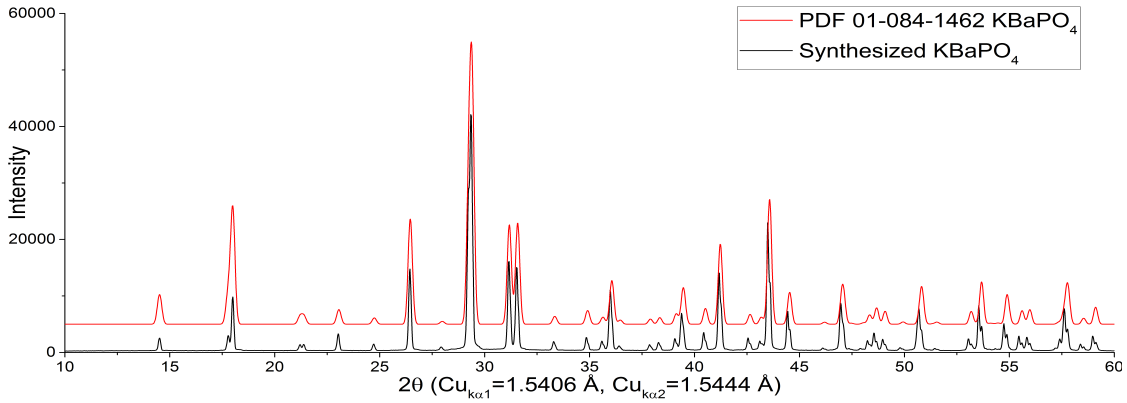

Figure 5.1: XRD-pattern showing the synthesized $KBaPO_4$ compared with the pattern for $KBaPO_4$ as reported by Masse & Durif [46]. It appears to be single-phase.

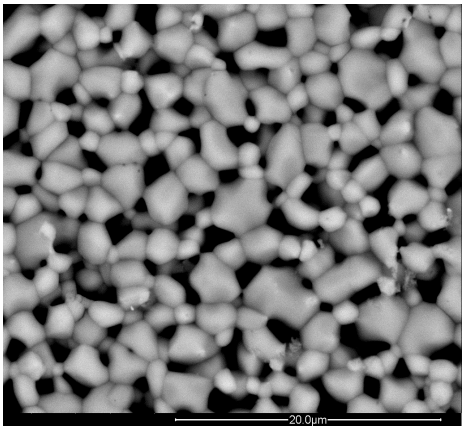

Figure 5.2: SEM-image of a prepared pellet of the synthesized $KBaPO_4$.

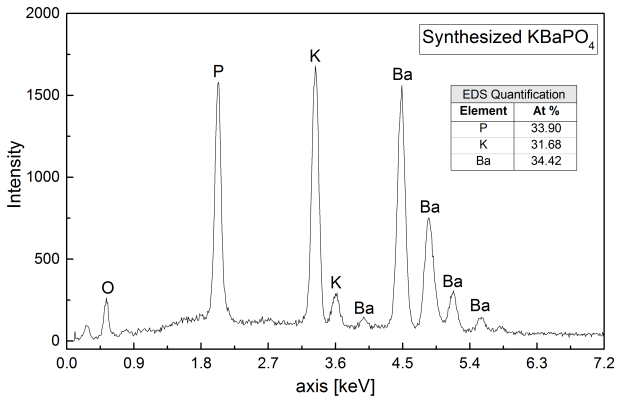

Figure 5.3: EDS spectrum of the surface of the $KBaPO_4$ sample in figure 5.2. Quantification shows, roughly, a 1:1:1 ratio of P:K:Ba.

Mechanochemical Approach

A mechanochemical approach was attempted in order to synthesize $KBaPO_4$, according to section 4.1.1. Figure 5.4 shows the result of two mechanochemical syntheses in the ball mill. Both syntheses were conducted at 450 RPM, however one synthesis was conducted in isopropanol (Wet-milled) whereas the other was dry (Dry-milled). There are clear differences between the two products, but they seem to have some phases in common.

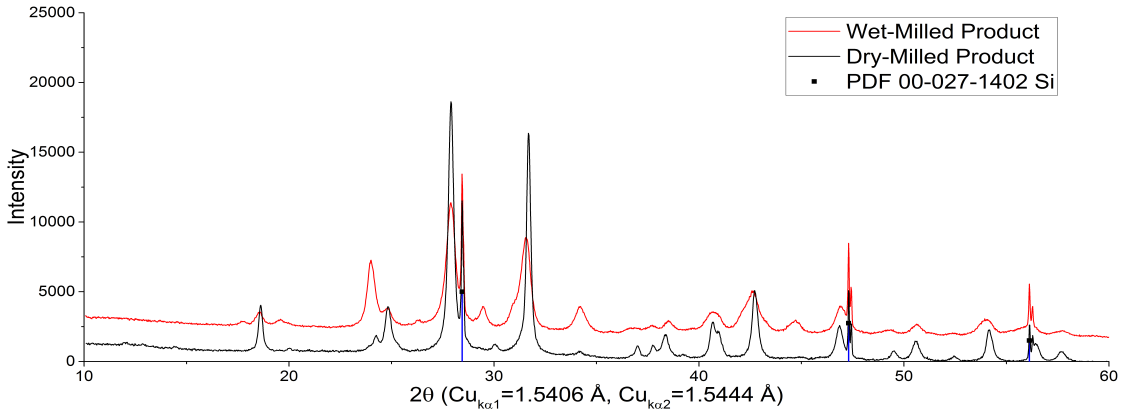

Figure 5.4: XRD-patterns showing the products from the attempts of mechanochemically synthesizing $KBaPO_4$. The patterns show a multitude of different peaks, and there are both similarities and differences between the two.

Thermogravimetric Analysis

Thermogravimetric analysis (Section 4.2.4), was utilized in order investigate the high-temperature decomposition products of $KBaPO_4$. FigureL 5.5 shows a plot of the mass change as a sample was heated to $1400\,^{\circ}C$. It is clear that there is a decomposition, as there is a loss of mass, and there is no sign of the reaction being complete after 6 hours of exposure. However, as soon as the temperature starts decreasing from $1400\,^{\circ}C$, even though it decreases rapidly, the decomposition reaction seems to come to a halt, suggesting that decomposition takes place somewhere between 1300 and $1400\,^{\circ}C$, corresponding with KOH evaporating around $1330\,^{\circ}C$. Figure 5.6 shows the XRD-pattern of the sample after the TG, compared with the patterns for $KBaPO_4$ [46] and $Ba_3(PO_4)_2$ [56]. It is clear that $KBaPO_4$ has decomposed into $Ba_3(PO_4)_2$, although 6 hours was not enough to achieve full decomposition of the sample.

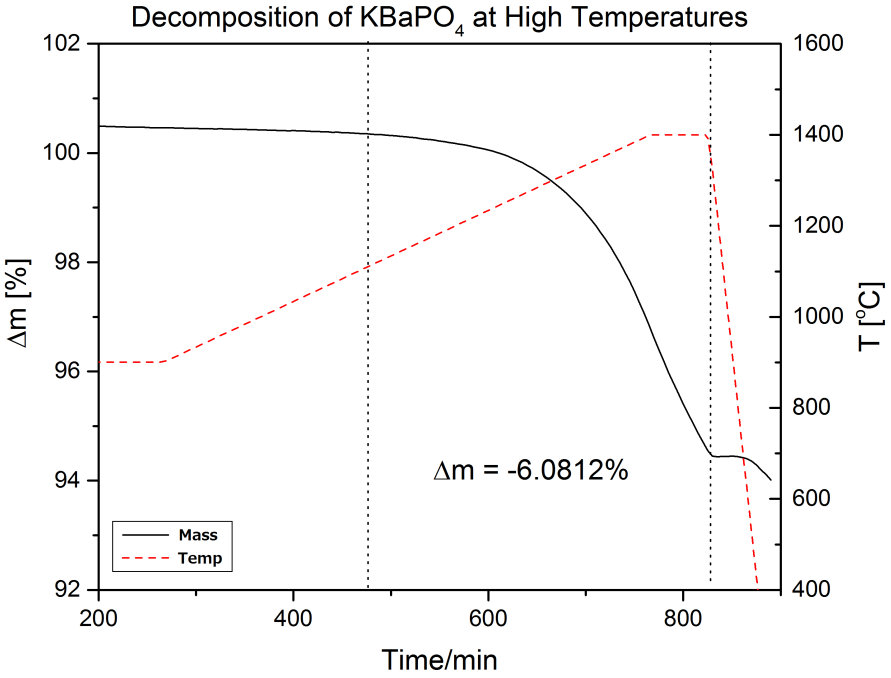

Figure 5.5: Result from TG of $KBaPO_4$. A sample was exposed to $1400\,^{\circ}C$ for 6 hours in order to investigate the high-temperature decomposition products of $KBaPO_4$.

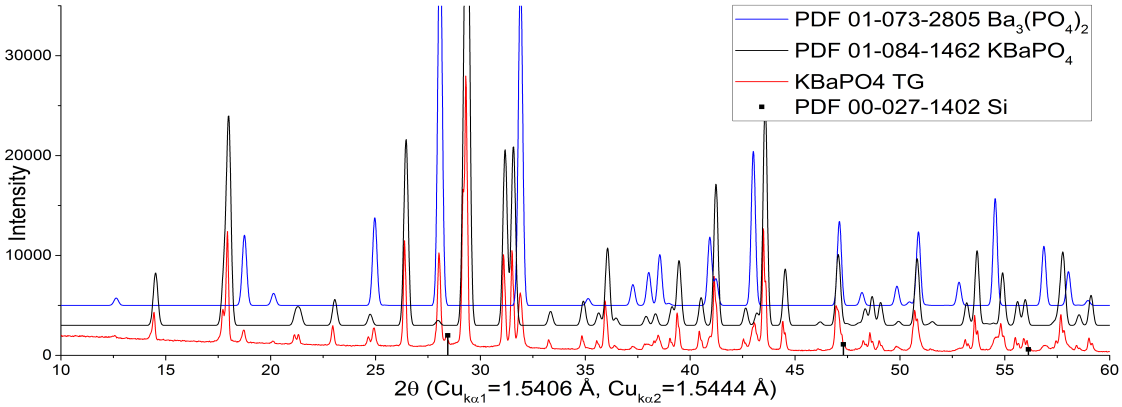

Figure 5.6: XRD-pattern showing $KBaPO_4$ after having been heated to $1400\,^{\circ}C$ for 6 hours, compared with the patterns for $KBaPO_4$ [46] and $Ba_3(PO_4)_2$ [56].

5.1.2 Hydration - $KBaPO_4 \rightarrow Ba_{3-x}K_xH_x(PO_4)_2$

One sample of $KBaPO_4$ underwent the hydration process described in section 4.4.1. After the initial 24 hours of exposure to steam at $80\,^{\circ}C$ in the high-humidity setup, the topography of the sample had changed (From figure 5.2 to figure 5.7) and upon further investigation of the cross section of said sample, figure 5.8, a change was revealed to have occurred in an inwards propagating manner. An investigation of the elemental composition of this changed area yielded the results shown in figure 5.9, where the ratio of P:K:Ba had changed drastically from that of single-phase $KBaPO_4$, from a 1:1:1 K:Ba:P ratio to a, roughly, barium:phosphorous ratio of 1.5:1, along with a very low K-content. Later, EDS was performed on multiple areas of a fully transformed sample, and an average K-content of said sample was found to be close to $6\,\%$. For the second part of the experiment, the two halves of the initial sample were installed in separate configurations (Following the outline described in section 4.4.1) and the following investigations of the cross sections of the two halves gave the images in figure 5.10 and 5.11 for, respectively, the half installed in steam at $80\,^{\circ}C$ and the half submerged in purified (Type I) water at room temperature.

Results indicate that the sample having been steamed for a total of 48 hours had fully transformed, and XRD on this new phase gave the pattern shown in figure 5.12. The pattern shows a great match to $Ba_3(PO_4)_2$, although with a slight shift in peak locations, indicating a deviation from the crystalline structure of pure $Ba_3(PO_4)_2$, possibly due to potassium impurities (Acceptor-doping).

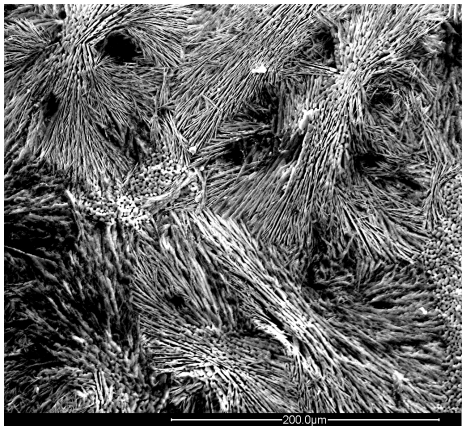

Figure 5.7: SEM-image showing the topography of a prepared pellet of the synthesized $KBaPO_4$ after having been exposed to steam at $80\,^{\circ}\mathrm{C}$ for 24 hours.

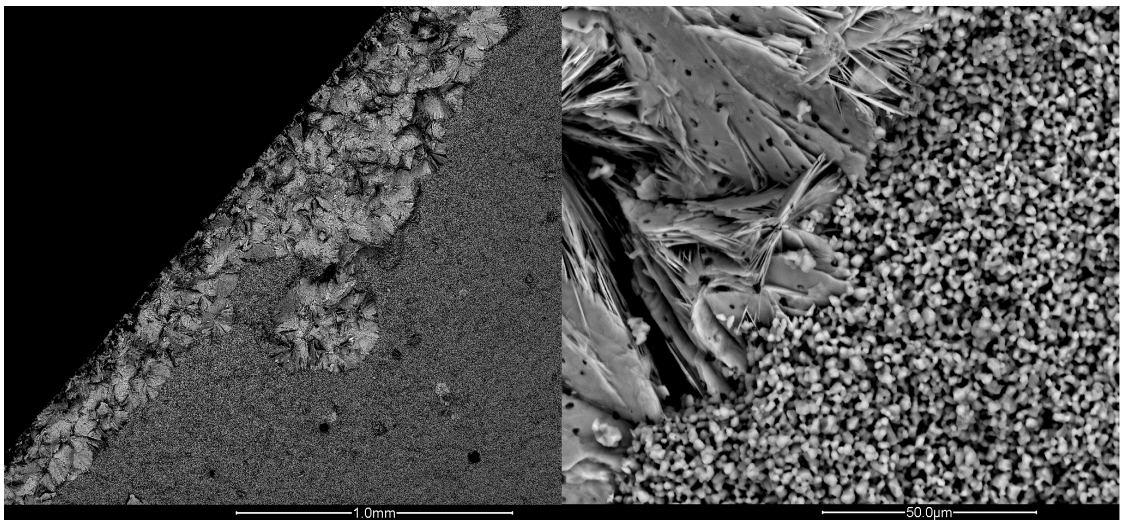

Figure 5.8: SEM-image of the cross section of a prepared $KBaPO_4$ sample after exposure to steam for 24 hours.

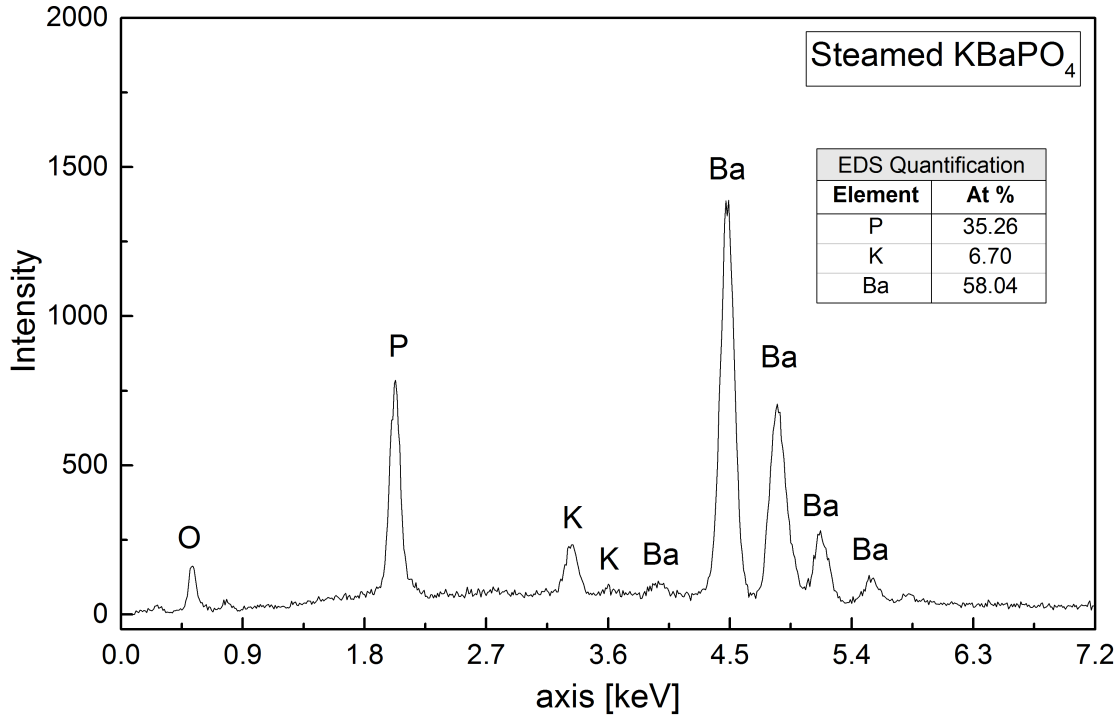

Figure 5.9: EDS spectrum of the surface of the steamed $KBaPO_4$ sample in figure 5.8. Quantification shows a different chemical composition than the 1:1:1 ratio of K:Ba:P found in $KBaPO_4$.

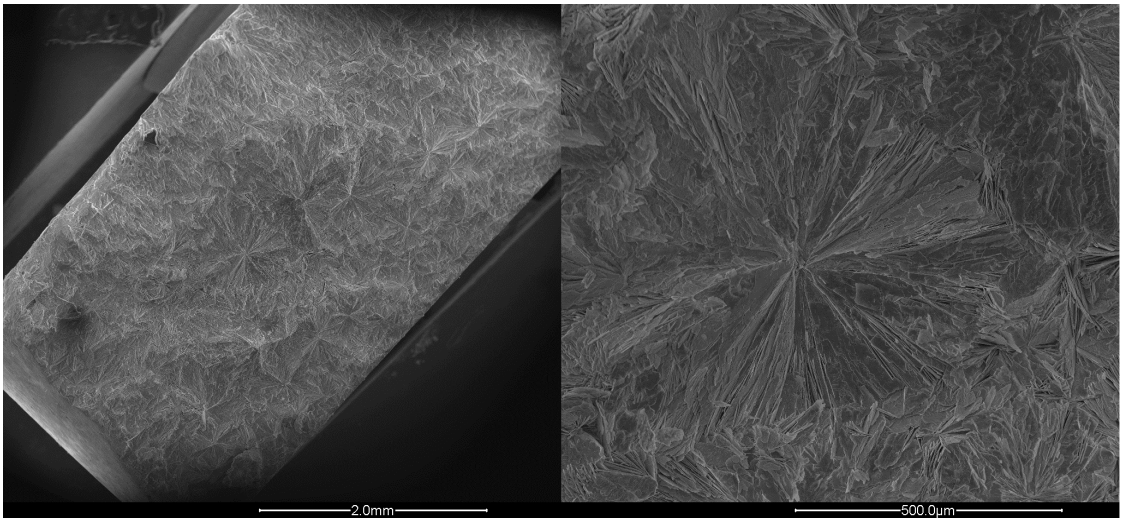

Figure 5.10: SEM-image of the cross section of a prepared $KBaPO_4$ sample after an additional 24 hours of exposure to steam, following the initial exposure to steam for 24 hours.

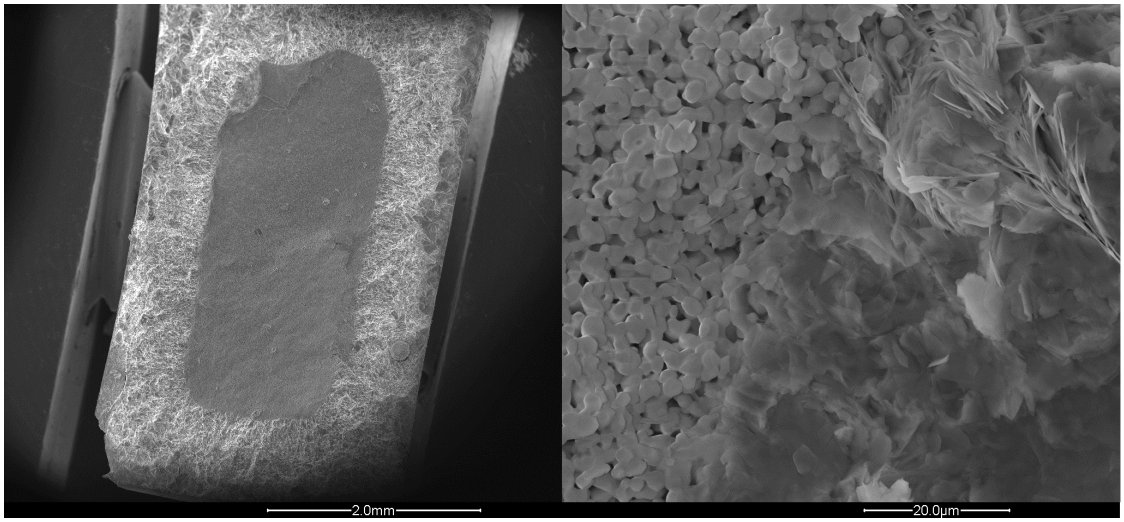

Figure 5.11: SEM-image of the cross section of a prepared $KBaPO_4$ sample after 24 hours of submersion in purified (Type I) water, following the initial exposure to steam for 24 hours.

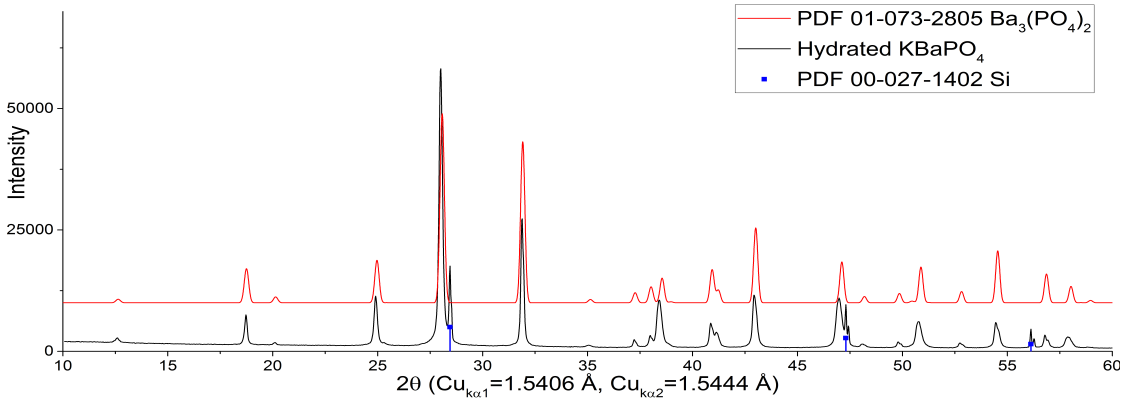

Figure 5.12: XRD-pattern of $KBaPO_4$ after exposure to steam for 48 hours (Figure 5.10), compared with the pattern for $Ba_3(PO_4)_2$ as reported by Manoun et al. [56].

High Temperature Treatment of Hydrated $KBaPO_4$

Subsequent heating of $Ba_{3-x}K_xH_x(PO_4)_2$ ($KBaPO_4$ exposed to water. See section 6.1.3) to 1100 °C yielded the XRD in figure 5.13, showing a mix of un-shifted $Ba_3(PO_4)_2$ and $KBaPO_4$, suggesting a two-phase system where $KBaPO_4$ is the minority phase. Figure 5.14 shows the same pattern compared with the pattern of the compound ($Ba_{3-x}K_xH_x(PO_4)_2$) as it was before heat treatment, and the previous peak-shift seems to have vanished, indicating that the $Ba_3(PO_4)_2$ does not contain as much potassium as it did before heating.

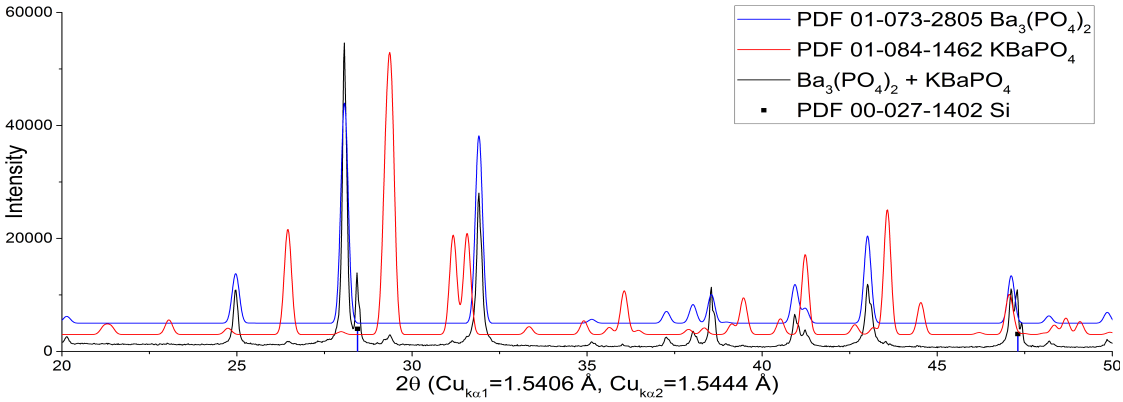

Figure 5.13: XRD-pattern of the compound obtained upon subjecting $KBaPO_4$ to water ($Ba_{3-x}K_xH_x(PO_4)_2$, Section 5.1.2) followed by heating to 1100 °C, compared with the patterns for $KBaPO_4$ [46] and $Ba_3(PO_4)_2$ [56]. There is no longer any apparent peak-shift in the $Ba_3(PO_4)_2$ phase.

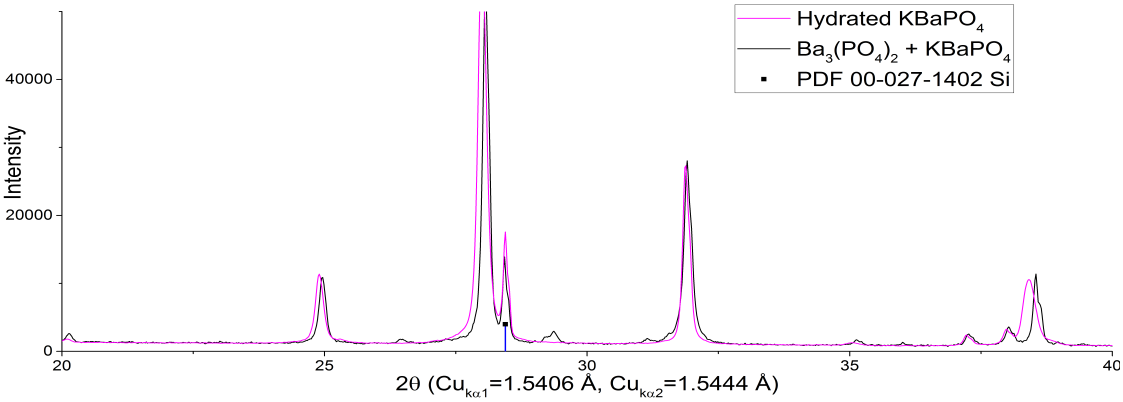

Figure 5.14: XRD-pattern of the compound obtained upon subjecting $KBaPO_4$ to water ($Ba_{3-x}K_xH_x(PO_4)_2$, Section 5.1.2) followed by heating to 1100 °C, compared with the pattern of the compound as it was before heat treatment.

5.1.3 Impedance Spectroscopy

Impedance of Pure $KBaPO_4$

Impedance measurements were performed on a sample of $KBaPO_4$ according to section 4.3.2. Figures 5.15 and 5.16 show the typical shape of the impedance spectra collected for $KBaPO_4$. The two semicircles can be attributed to physical processes in which the specific capacitances can be estimated as $19\,\mathrm{pF}$ for the high-frequency semicircle and $100\,\mathrm{pF}$ for the low-frequency semicircle. The two processes can again be attributed to bulk and grain-boundary conductivities, respectively, due to the latter process having a larger resistance than the former. Other than for the measurements at $500\,^{\circ}\mathrm{C}$ [1], figure 5.16, all other measurements were similar to the one at $400\,^{\circ}\mathrm{C}$ in that there was no significant difference between dry and humidified air. Figure 5.17 shows the typical shape of impedance spectra collected in humidified atmospheres at temperatures below $150\,^{\circ}\mathrm{C}$, and again, the two semicircles can be attributed to bulk and grain-boundary processes with specific capacitances of about $19\,\mathrm{pF}$ and $100\,\mathrm{pF}$, respectively. Figure 5.18 shows how small the difference is between impedance spectra collected for high and low pO_2 at $500\,^{\circ}\mathrm{C}$, and is indicative of oxygen vacancies not contributing to the conductivity of $KBaPO_4$ in any significant manner. Figure 5.19 shows the separated bulk and grain-boundary conductivities of $KBaPO_4$ in dry and humidified air, showing an indifference towards humidity.

Based on the analysis of $\ln(\sigma T)$ *vs* $\frac{1}{T}$ from the plot in figure 5.19, activation energies and pre-exponentials for the conductivity of $KBaPO_4$ at temperatures above $300\,^{\circ}\mathrm{C}$ are displayed in table 5.1. The seemingly constant values for the activation energies and the pre-exponentials indicate, again, that there is no signficiant effect of humidity on the conductivity of $KBaPO_4$.

Table 5.1: Summary of the estimated values for the activation energies and the pre-exponentials from the linear fit of the conductivity of $KBaPO_4$ above $300\,^{\circ}\mathrm{C}$ in dry and humidified air, based on the analysis of $\ln(\sigma T)$ *vs* $\frac{1}{T}$ from the plot in figure 5.19.

	Activation Energy E_a [$\mathrm{kJ\,mol^{-1}}$]			Pre-Exponential $\log(\sigma_0)$ [$\mathrm{S\,cm^{-1}}$]		
	Bulk	GB	Total	Bulk	GB	Total
Wet Air	107 ± 4	125.5 ± 4	110 ± 4	3.7 ± 0.2	4.5 ± 0.3	3.5 ± 0.3
Dry Air	108 ± 6	126.4 ± 0.6	106 ± 6	3.8 ± 0.4	4.4 ± 0.1	3.1 ± 0.5

[1] In retrospect, this measurement should have been redone in order to determine whether this stems from the measurement itself or if there is an effect at this particular temperature. Further discussion of this discrepancy would be speculative because of inconclusive data.

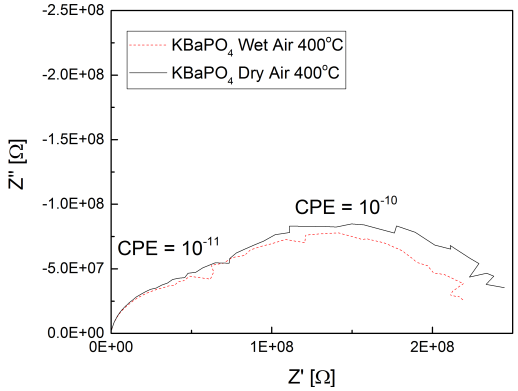

Figure 5.15: Impedance spectra for $KBaPO_4$ in dry and humidified air at $400\,^{\circ}C$. Magnitudes for the process capacitances are displayed.

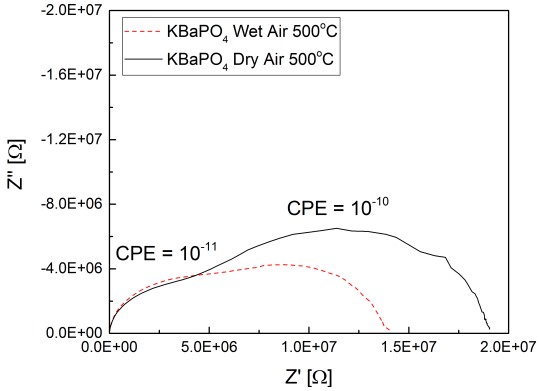

Figure 5.16: Impedance spectra for $KBaPO_4$ in dry and humidified air at $500\,^{\circ}C$. Magnitudes for the process capacitances are displayed.

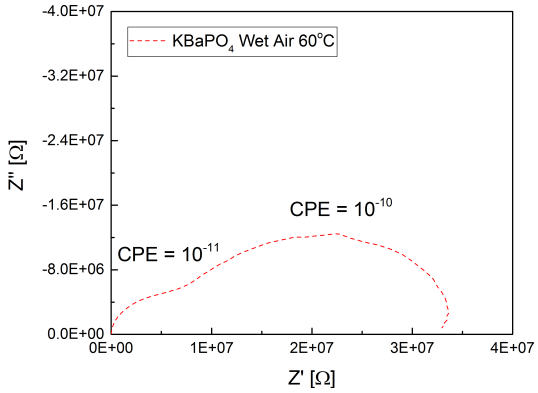

Figure 5.17: Impedance spectrum for $KBaPO_4$ in humidified air at $60\,^{\circ}C$. Magnitudes for the process capacitances are displayed.

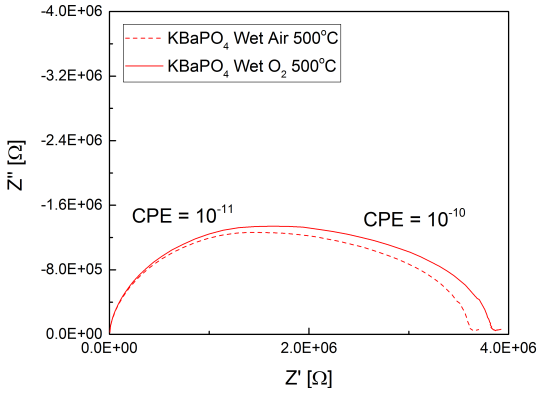

Figure 5.18: Impedance spectra for $KBaPO_4$ in humidified air and O_2 at $500\,^{\circ}C$, effectively comparing low and high pO_2 ($0.21\,\mathrm{atm}$ *vs* $1\,\mathrm{atm}$). The spectra were collected 3 months after previous measurements on the $KBaPO_4$ sample.

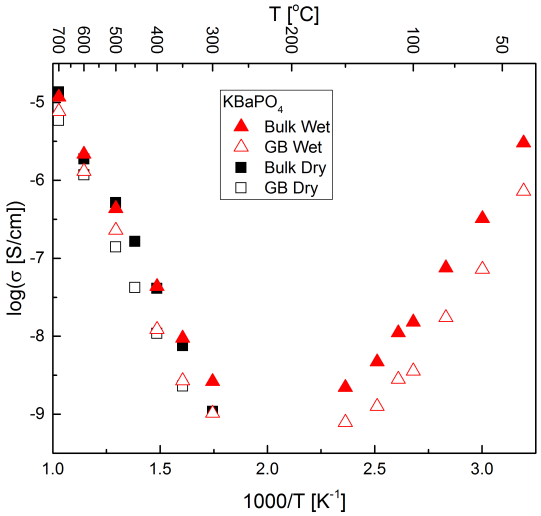

Figure 5.19: Plot of the bulk and grain-boundary conductivities of $KBaPO_4$ in dry and humidified air.

In Situ IS on $KBaPO_4$ in a High-Humidity Atmosphere (Steam)

In situ impedance measurements were conducted on the sample of $KBaPO_4$ (On which the initial electrical measurements were conducted) in the setup for high humidity, as described in section 4.3.1. These measurements were conducted about 3 months after the initial measurements on the sample. The continuous measurements at $1\,\mathrm{kHz}$ can be seen in figure 5.20, and the collected impedance spectra at the end of various cycles can be observed in figure 5.21. The measurement scheme was developed as the measurements were running, and the steps can be summarized as follows:

- Initial measurements were conducted in humidified air to confirm that the initial conductivity was similar to the one previously observed.

  1st cycle: The water basin was heated to $80\,^{\circ}\mathrm{C}$ and the sample was exposed for 4 hours, followed by cooling the water basin down to room temperature.

  2nd cycle: The water basin was heated to $80\,^{\circ}\mathrm{C}$ and the sample was exposed for 6 hours, followed by cooling the water basin down to room temperature.

  3rd cycle: The water basin was heated to $80\,^{\circ}\mathrm{C}$ and the sample was exposed for 6 hours, followed by cooling the water basin down to room temperature.

- The cell was heated to $200\,^{\circ}\mathrm{C}$ in order to dry the sample. The sample was dried for 16 hours before being cooled down to room temperature.

  4th cycle: The water basin was heated to $80\,^{\circ}\mathrm{C}$ and the sample was exposed for 120 hours, followed by cooling the water basin down to room temperature.

- The sample was removed from the ProboStat cell and analysed by SEM. Figure 5.22 shows an area of the surface of the sample, displaying clear signs of a change in topography and composition.

It is clear that, upon steaming, the conductivity increases with exposure time. However, as the heater is switched off, and the water vapour pressure decreases, the increase is not retained, and the results do not mirror those of Sing and Goodenough.

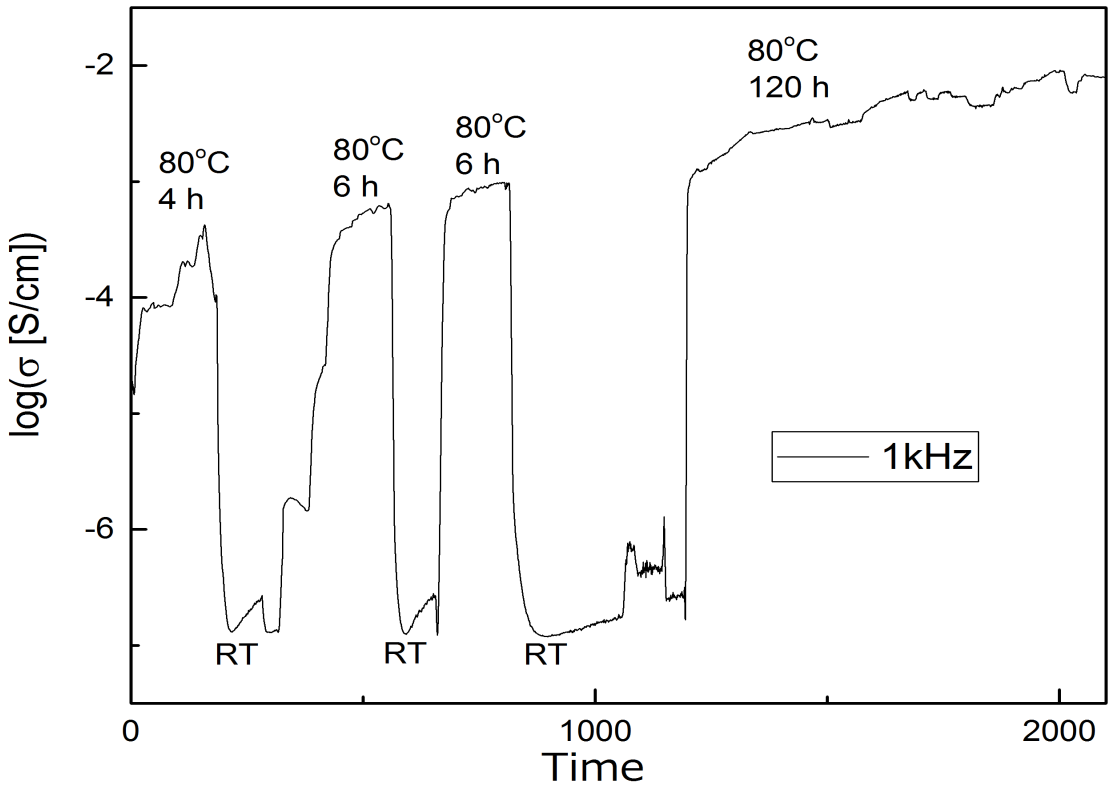

Figure 5.20: Continuous conductivity measurements of $KBaPO_4$ at 1 kHz during cyclic exposure to high water vapour pressures in the High-Humidity Setup. 1) 1st cycle, 4 hours of exposure. 2) 2nd cycle, 6 hours of exposure. 3) 3rd cycle, 6 hours of exposure. 4) 4th cycle, 120 hours of exposure. The conductivity has not been corrected for sample geometry.

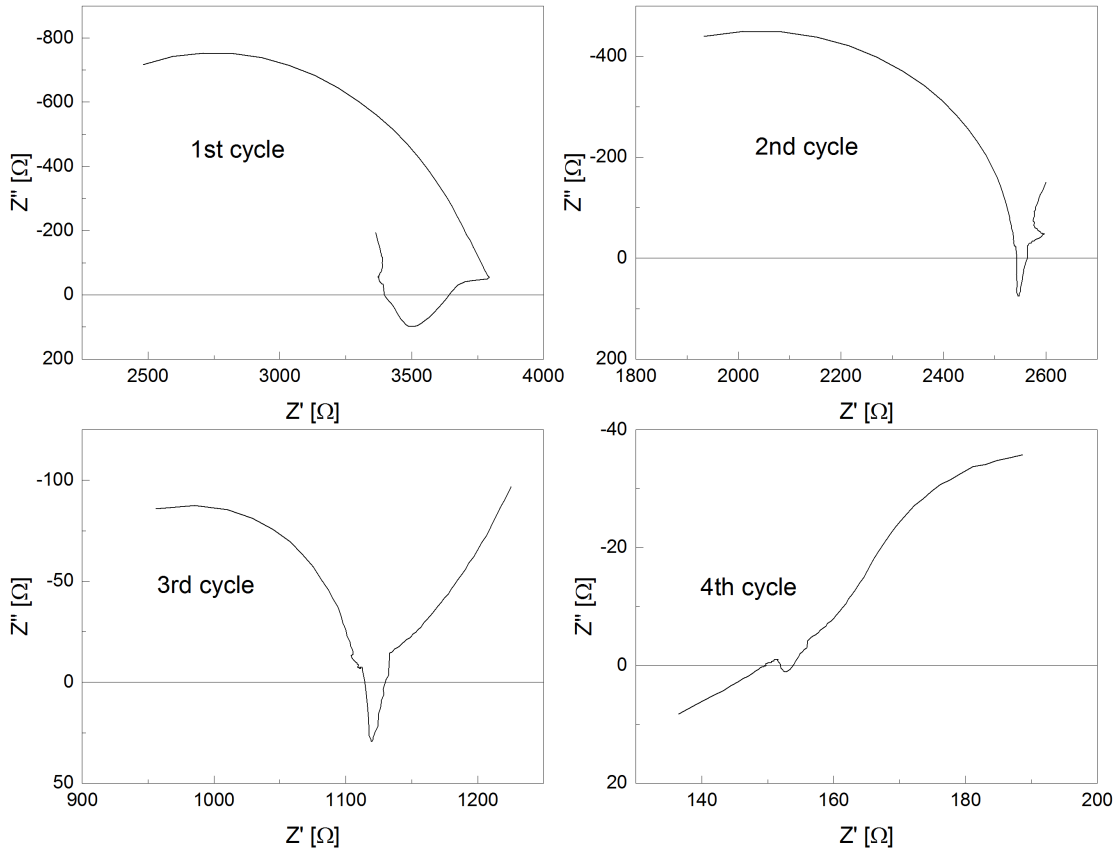

Figure 5.21: Impedance spectra for $KBaPO_4$ during exposure to high water vapour pressures in the High-Humidity Setup. 1) 1st cycle, 4 hours of exposure. 2) 2nd cycle, 6 hours of exposure. 3) 3rd cycle, 6 hours of exposure. 4) 4th cycle, 120 hours of exposure.

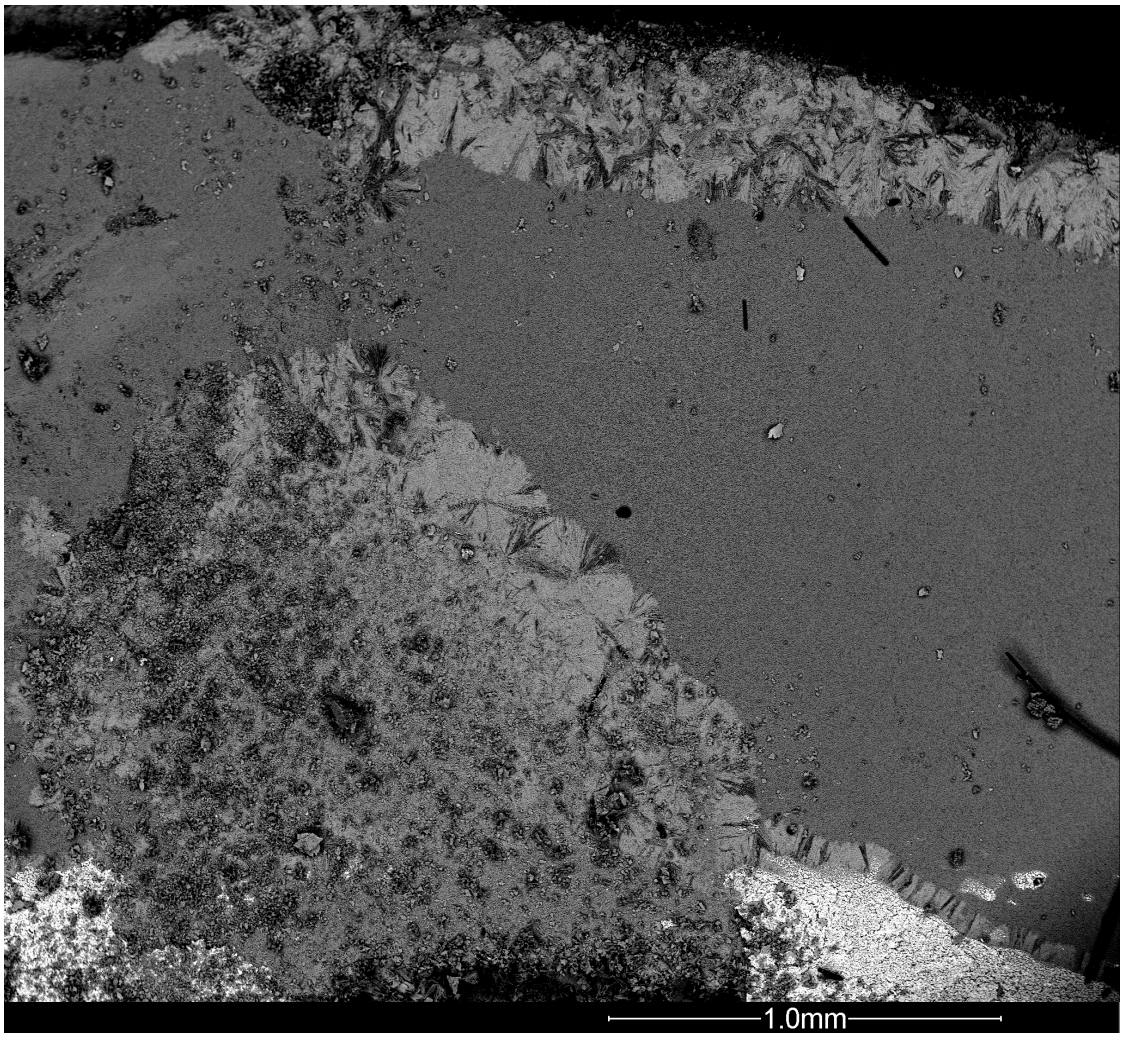

Figure 5.22: SEM-image of an area on the surface of the sample of $KBaPO_4$ measured in the high-humidity setup. The surface shows clear signs of change in topography and in chemical composition (Contrast).

Impedance of $KBaPO_4$ Post-Hydration - $Ba_{3-x}K_xH_x(PO_4)_2$

Impedance measurements were performed on a sample of the new compound resulting from attempts at hydrating $KBaPO_4$. As will be clear from section 6.1.3, this compound will from now on be referred to as $Ba_{3-x}K_xH_x(PO_4)_2$, due to results pointing towards a proton containing compound. Figure 5.23 shows the impedance spectra collected in dry and humidified air at 200 °C, showing a clear difference between the two atmospheres, indicating that humidity does have an effect on the bulk conductivity of the compound. Figure 5.25 shows the bulk conductivities of the compound in dry and humidified air, as estimated by deconvolution and model fitting of the obtained impedance spectra. Due to a theorized decomposition taking place somewhere between 250 to 300 °C in dry air, the measurements were conducted upwards from 100 to 300 °C, starting in wet air. In figure 5.25, the value in dry air at 300 °C not following the linear trend can probably be contributed to decomposition. In fact, as is seen from figure 5.24, switching back to humidified air gives an impedance spectrum almost identical to that of the dry air.
Activation energies and pre-exponentials are displayed in table 5.2. As is the case for the overall conductivity, these values are not greatly affected by humidity, but there is a difference.

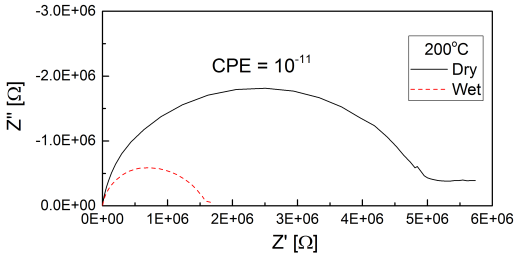

Figure 5.23: Collected impedance spectra for $Ba_{3-x}K_xH_x(PO_4)_2$at 200 °C, as obtained by hydration of $KBaPO_4$, in dry and humidified air. Magnitudes for the process capacitances are displayed.

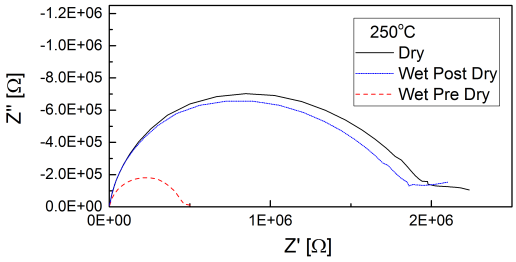

Figure 5.24: Collected impedance spectra for $Ba_{3-x}K_xH_x(PO_4)_2$ at 250 °C, as obtained by hydration of $KBaPO_4$, in dry and humidified air. After having measured the sample in dry air, there is seemingly no change in the impedance upon going back to humidified air, possibly indicating that an irreversible decomposition had occurred.

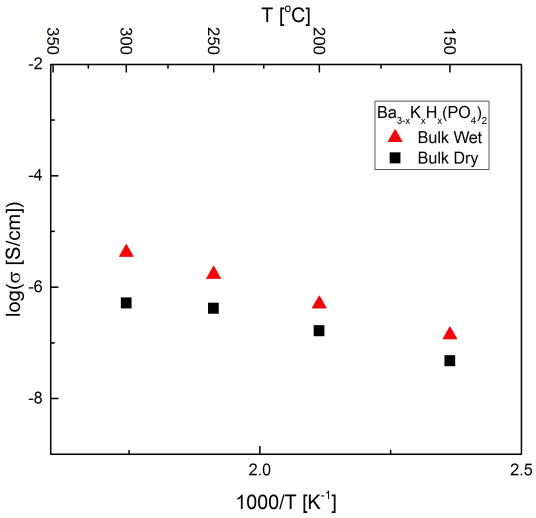

Figure 5.25: Plot of the bulk conductivity in dry and humidified air for the compound $Ba_{3-x}K_xH_x(PO_4)_2$. Note that the temperatures were ramped upwards from 100 to 300 °C.

Table 5.2: Summary of the estimated values for the activation energies and the pre-exponentials from the linear fit of the bulk conductivity of $Ba_{3-x}K_xH_x(PO_4)_2$in dry and humidified air, based on the analysis of $\ln(\sigma T)$ *vs* $\frac{1}{T}$ from the plot in figure 5.25.

	Activation Energy E_a [kJ mol^{-1}]	Pre-Exponential $\log(\sigma_0)$ [S cm^{-1}]
Wet Air	55 ± 1	2.1 ± 0.3
Dry Air*	51 ± 0	1 ± 0

*Linear fit with only two data points, there is no estimated standard deviation

Impedance of the Two-Phase System of $Ba_3(PO_4)_2$ and $KBaPO_4$

Impedance measurements were performed on a sample of the proposed two-phase system of $Ba_3(PO_4)_2$ and $KBaPO_4$ obtained upon heating $Ba_{3-x}K_xH_x(PO_4)_2$ to 1100 °C. Figure 5.26 shows the impedance spectra collected in dry and humidified air at 500 °C, showing a large effect of humidity on the impedance of the bulk and grain-boundary processes. Figure 5.27 shows the impedance spectra in humidified air and humidified O_2 at 500 °C, showing a seemingly insignificant effect of pO_2 on the conductivity of the compound. Additionally, figure 5.28 shows the difference in impedance upon switching between humidifying the air with H_2O and D_2O. Figure 5.29 shows the change in conductance at 10 kHz as the humidifying step is switched between H_2O and D_2O, and a small, but measurable, change is observed. Figure 5.30 shows the bulk conductivity of

this two-phase system, and there is a clear difference between dry and humidified air. Activation energies and pre-exponentials are displayed in table 5.3. The activation energy does not differ much when going from dry to humidified air, but the increase in the pre-exponential could indicate an increase in the fractional occupancy with respect to the charge carrier, from equation 2.1.3.

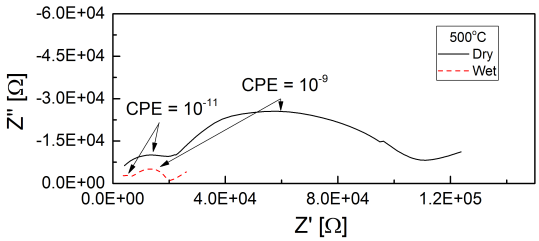

Figure 5.26: Impedance spectra for the two-phase system of $Ba_3(PO_4)_2$ and $KBaPO_4$. The spectra shown were collected at $500\,^{\circ}\mathrm{C}$ in dry air and humidified air. The magnitudes for the process capacitances are displayed. Due to the large differences, arrows have been included to mark the semicircles.

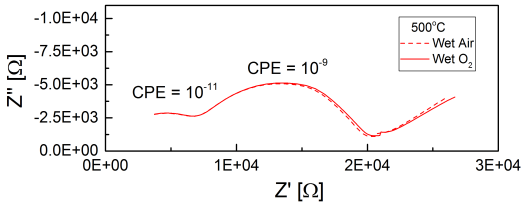

Figure 5.27: Impedance spectra for the two-phase system of $Ba_3(PO_4)_2$ and $KBaPO_4$. The spectra shown were collected at $500\,^{\circ}\mathrm{C}$ in humidified air ($pO_2 = 0.21\,\mathrm{atm}$) and humidified O_2. The magnitudes of the process capacitances are displayed. The two spectra appear to be almost identical.

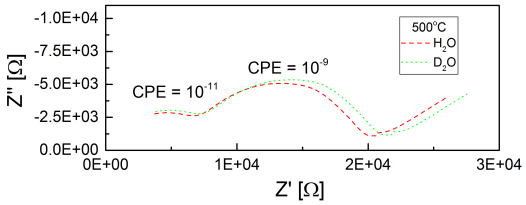

Figure 5.28: Impedance spectra for the two-phase system of $Ba_3(PO_4)_2$ and $KBaPO_4$. The spectra shown were collected at $500\,^{\circ}\mathrm{C}$ in air humidified by H_2O and D_2O. The magnitudes for the process capacitances are displayed. Switching from H_2O to D_2O seems to have had a small, but measurable, effect.

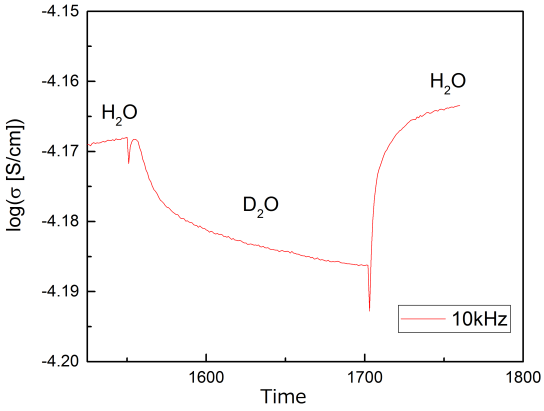

Figure 5.29: Continuous conductivity measurements at $10\,\mathrm{kHz}$ of the two-phase system of $Ba_3(PO_4)_2$ and $KBaPO_4$. The section shows how the conductivity varies as the humidifying step is switched between H_2O and D_2O. There is a small, but measurable, effect.

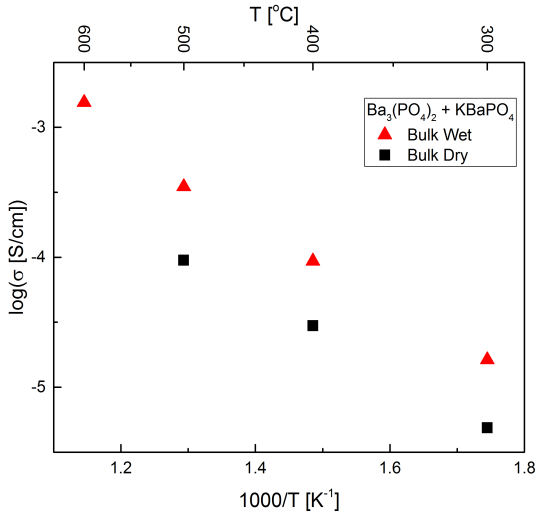

Figure 5.30: Plot of the bulk conductivity in dry and humidified air for the two-phase system of $Ba_3(PO_4)_2$ and $KBaPO_4$.

Table 5.3: Summary of the estimated values for the activation energies and the pre-exponentials from the linear fit of the bulk conductivity of the two-phase system of $Ba_3(PO_4)_2$ and $KBaPO_4$ obtained upon heating $Ba_{3-x}K_xH_x(PO_4)_2$ to 1100 °C, in dry and humidified air, based on the analysis of $\ln(\sigma T)$ *vs* $\frac{1}{T}$ from the plot in figure 5.30.

	Activation Energy E_a [kJ mol^{-1}]	Pre-Exponential $\log(\sigma_0)$ [S cm^{-1}]
Wet Air	65.9 ± 0.4	3.69 ± 0.07
Dry Air	64 ± 2	3.0 ± 0.4

5.2 $NaCaHSiO_4$ and Related Compounds

5.2.1 Synthesis & Characterization

$NaCaHSiO_4$ and related compounds $ABHXO_4$ (A=Li, Na or K. B=Ca, Sr or Ba. X=Si, Ge or Sn) were attempted synthesized according to the hydrothermal method described in section 4.1.1. For $NaCaHSiO_4$, figure 5.31 shows that the resulting product is seemingly single-phase. For the various other syntheses, Table 5.4 summarizes the compounds that were attempted synthesized and the phases that were found in the various XRD patterns of the resulting products. Among these, only $NaCaHSiO_4$ gave the desired product, whereas the only other synthesis that gave a single-phase product (Not the desired product) was from the attempt at synthesizing $NaSrHSiO_4$, giving Sr_2SiO_4.

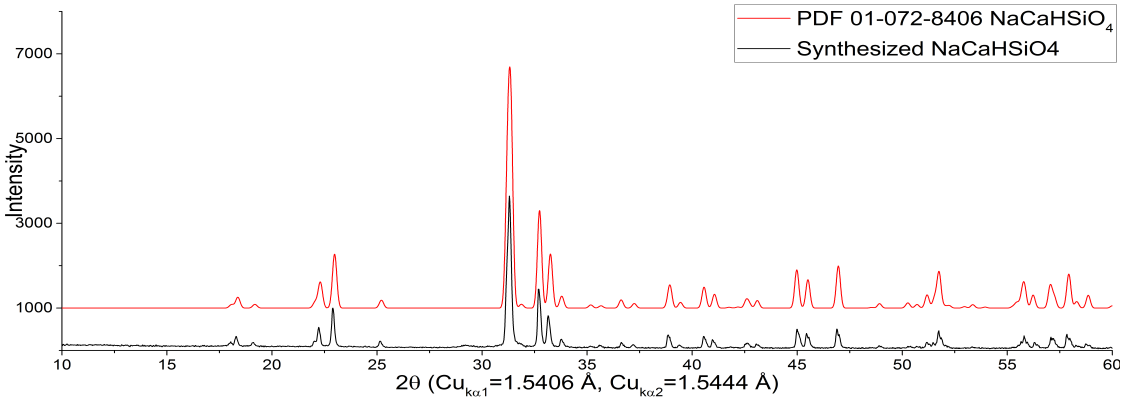

Figure 5.31: XRD-pattern showing the synthesized $NaCaHSiO_4$ compared with the pattern for $NaCaHSiO_4$ as reported by Cooksley & Taylor [49].

Table 5.4: The observed phases in the various products from the multiple syntheses of compounds $ABHXO_4$ (A=Li, Na or K. B=Ca, Sr or Ba. X=Si, Ge or Sn). The XRD patterns from the PDF database of the phases listed have been matched to the XRD spectra collected for the products.

Intended Product	Observed Phases
Silicates	
$LiCaHSiO_4$	Li_2SiO_3, $Ca(OH)_2$, CaO, $CaCO_3$
$NaCaHSiO_4$	Single-phase $NaCaHSiO_4$
$NaSrHSiO_4$	Single-phase Sr_2SiO_4
$KCaHSiO_4$	Ca_2SiO_4 and various calcium silicates
$KSrHSiO_4$	$SrSiO_3$, Sr_2SiO_4
$KBaHSiO_4$	$BaSiO_3$, Ba_2SiO_4
Germanates	
$NaCaHGeO_4$	$CaGe_4O_9$, GeO_2, $Ca(OH)_2$, $NaOH$
$KSrHGeO_4$	$SrGeO_3$, $SrCO_3$, GeO_2
$KBaHGeO_4$	$Ba_3(GeO_3)_3$, $BaCO_3$, $BaHF_3$, $KHCO_3$
Stannates	
$NaCaHSnO_4$	$Ca(OH)_2$, $Na_2Sn(OH)_6$, $CaSn(OH)_6$
$KSrHSnO_4$	$Sr(OH)_2$, $SrSnO_3$

5.2.2 Impedance Spectroscopy

Impedance measurements were conducted on $NaCaHSiO_4$, according to the process described in section 4.3.2. Figures 5.32 and 5.33 show SEM images of the surface of

the pellet on which electrical measurements were conducted. Average grain size is less than $10\,\mu m$ Figure 5.34 shows the collected spectra at $300\,^{\circ}C$ in dry and humidified air, and shows the typical shape of the impedance spectra collected for $NaCaHSiO_4$. Figure 5.36 shows the bulk conductivity of the sample, with a clear difference between dry and humidified atmospheres. Table 5.5 summarizes the activation energies and the pre-exponentials for the linear fits of the conductivity of $NaCaHSiO_4$. Again there is a clear difference between the dry and humidified atmosphere.

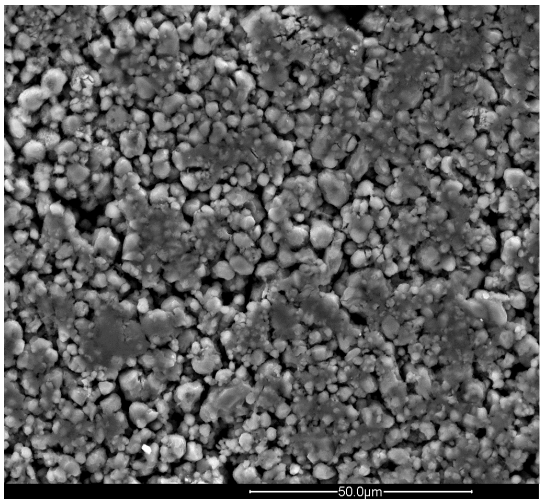

Figure 5.32: SEM-image of the surface of the prepared pellet of the synthesized $NaCaHSiO_4$ on which electrical measurements were conducted.

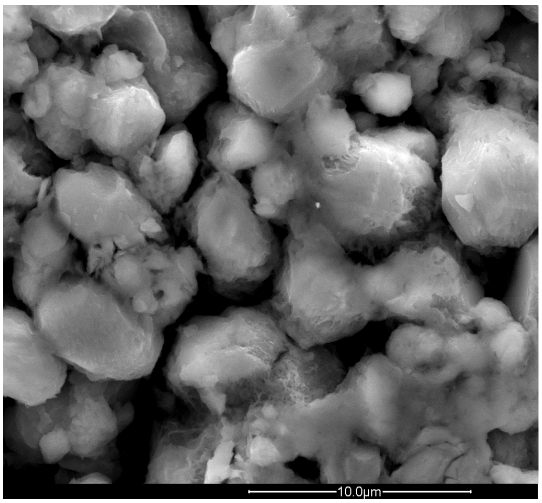

Figure 5.33: SEM-image of the surface of the prepared pellet of the synthesized $NaCaHSiO_4$ on which electrical measurements were conducted. The image is a magnified view of an area in figure 5.32.

Table 5.5: Summary of the estimated values for the activation energies for the conductivity $NaCaHSiO_4$. Data collected in dry air, as well as air humidified by both H_2O and D_2O. Values based on the analysis of $\ln(\sigma T)$ *vs* $\frac{1}{T}$ from the plot in figure 5.36.

	Activation Energy E_a [$\mathrm{kJ\,mol^{-1}}$]	Pre-Exponential ($\ln(\sigma_0)$) [$\mathrm{S\,cm^{-1}}$]
H_2O	74 ± 4	0.75 ± 0.03
D_2O	72 ± 2	0.77 ± 0.05
Dry	84.7 ± 0.9	0.88 ± 0.01

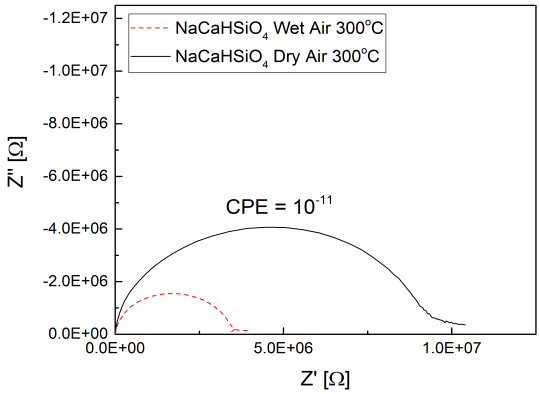

Figure 5.34: Typical shape of the impedace spectra collected for $NaCaHSiO_4$. Magnitudes of the process capacitances are displayed.

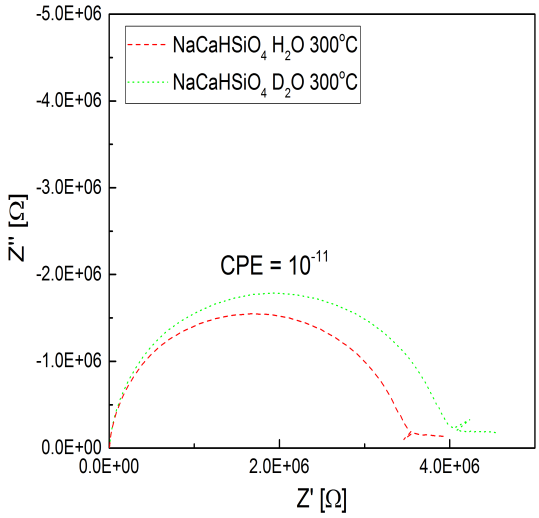

Figure 5.35: Comparison of the impedance spectra collected at 300 °C in air humidified by H_2O and D_2O. Switching from H_2O to D_2O seems to have an effect.

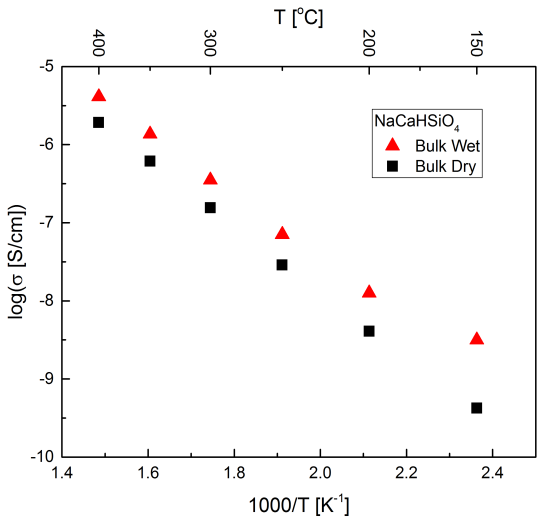

Figure 5.36: Plot of the bulk conductivity in dry and humidified air for $NaCaHSiO_4$.

5.3 BaH_2SiO_4

5.3.1 Synthesis & Characterization

BaH_2SiO_4 was synthesized according to the hydrothermal method described in section 4.1.1. Figure 5.37 shows that the product of the synthesis is single phase BaH_2SiO_4.

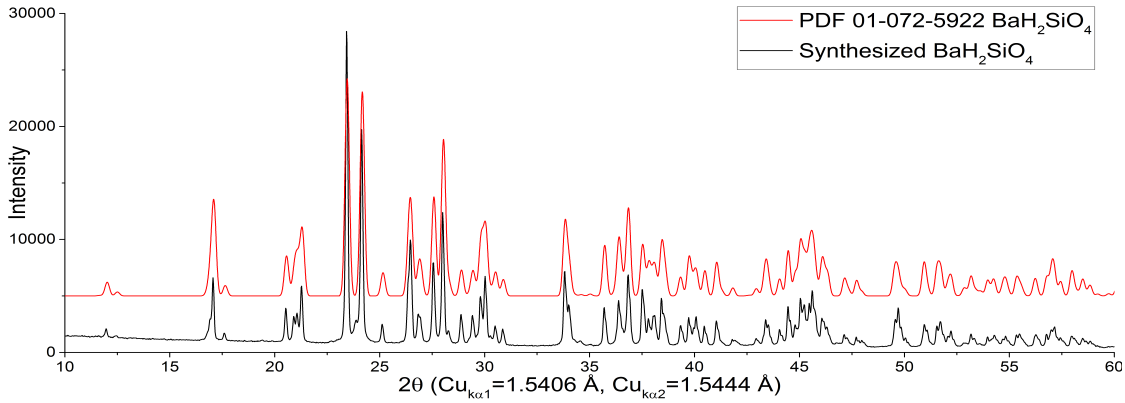

Figure 5.37: XRD-pattern showing the synthesized BaH_2SiO_4 compared with the pattern for BaH_2SiO_4 as reported by Chen et al. [57].

5.3.2 Impedance Spectroscopy

Impedance measurements were performed on a sample of BaH_2SiO_4 according to section 4.3.2. Figure 5.38 shows the typical shape of, and the magnitude of the process capacitances for, the impedance spectra obtained for BaH_2SiO_4. There is an observable effect from humidity, but it is not a large one. The spectra could all be fitted with a depressed semicircle. Figure 5.39 shows the bulk conductivity of BaH_2SiO_4.

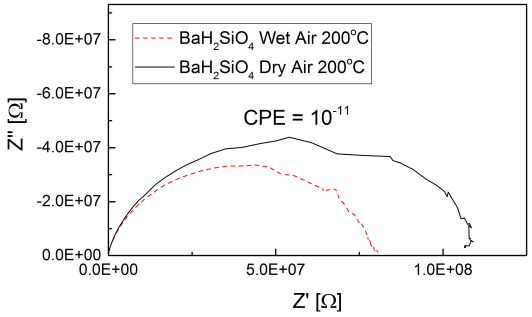

Figure 5.38: Comparison of the impedance spectra collected for BaH_2SiO_4 in dry and humidified air at 200 °C. The magnitudes for the process capacitances are displayed.

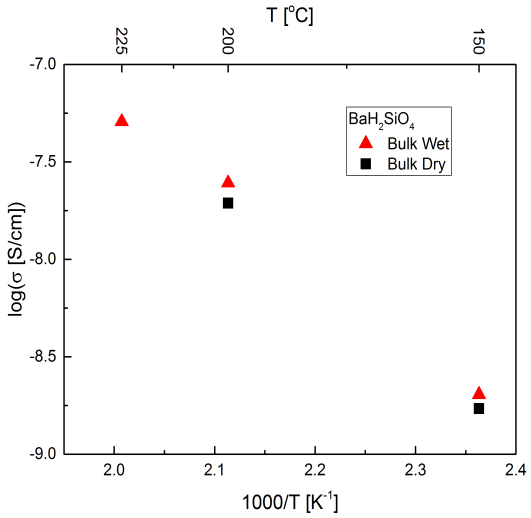

Figure 5.39: Plot of the bulk conductivities in dry and humidified air for BaH_2SiO_4.

Chapter 6

Discussion

6.1 $KBaPO_4$

The main topic of this project was $KBaPO_4$. Initially, the goal was to synthesize $KBaPO_4$ and characterize it by electrical measurements, as well as hydrate it in an attempt at reproducing the results by Goodenough and Singh [4]. Single-phase $KBaPO_4$ was obtained through the solid-state synthesis route, whereas the mechanochemical route (To be discussed) did not give the same result. Subsequent conductivity measurements were conducted on the single-phase $KBaPO_4$ without problems. Attempts at hydrating $KBaPO_4$ did not give the results that were expected at the outset, and $KBaPO_4$ was found to decompose due to water.
In section 6.1.1, the results from the attempt at mechanochemically synthesizing $KBaPO_4$ will be briefly discussed, as well as TG on single-phase $KBaPO_4$. The results of the electrical measurements on single-phase $KBaPO_4$ will be discussed in section 6.1.2, and the validity of the defect model proposed earlier will be investigated. Additionally, subjecting $KBaPO_4$ to water causes a decomposition into a K-containing $Ba_3(PO_4)_2$ phase. This decomposition, as well as *in-situ* impedance measurements on $KBaPO_4$ during steaming, is thoroughly explained in section 6.1.3. Subsequent electrical measurements were performed on this phase, and will be discussed in section 6.2.1. As this K-containing $Ba_3(PO_4)_2$ phase is heated to high temperatures, to be discussed in section 6.2.2, a two-phase system consisting of $Ba_3(PO_4)_2$ and a secondary minority phase $KBaPO_4$ is obtained. Lastly, in section 6.2.3, the three systems are compared with each other, as well as a sample of single-phase $Ba_3(PO_4)_2$.
The work on electrically characterizing and hydrating $KBaPO_4$ has culminated in a submitted paper [3].

6.1.1 Synthesis and Characterization of $KBaPO_4$

Mechanochemical Synthesis

Besides the high-temperature solid state route of synthesizing $KBaPO_4$, attempts were made to synthesize $KBaPO_4$ by high-energy ball milling in a mechanochemical method, as described in section 4.1.1. Two syntheses were conducted, one in a wet environment and one in a dry environment. The products from the syntheses yielded the XRD patterns displayed in figure 5.4. A zoomed view of figure 5.4 is introduced in figure 6.1,

where the PDF patterns for $KBaPO_4$, $Ba_3(PO_4)_2$, and patterns for two different phases of KH_2PO_4 are included for comparison.
Due to the reaction taking place at room temperature and that a successfull combustion reaction was suggested to take place above $1000\,^{\circ}\mathrm{C}$, a reasonable expectation would be that some reactants will be visible in the XRD spectrum of the mixture. No peaks were matched to $BaCO_3$, indicating that most, if not all, of it has reacted to form $Ba_3(PO_4)_2$. Additionally, due to the favourable reaction in which carbonates decompose to give CO_2, there is a possibility for the presence of small quantities of various barium-containing intermediates that are undetectable with the chosen measurement program. It is clear that there is a difference between the products in the wet-milled (The one with isopropanol) and the dry-milled syntheses. There is seemingly a larger amount of the KH_2PO_4 reactant left in the wet-milled synthesis, a result that can likely be contributed to the reactant partially dissolving in the isopropanol solution during milling, followed by subsequent solidification upon drying the mixture post-milling.
The two most intense peaks for $KBaPO_4$ lie between 20 and 30 on the 2θ axis, and judging by these 2θ values in the synthesized products, the wet-milled synthesis have clear peaks at these locations. For the dry-milled product however, at just below 30 on the 2θ axis, where the $KBaPO_4$ peak of highest intensity would be, it is not possible to discern whether or not there is a slight bump in the pattern, either owing to the selected measurement program or that the phase is present in minuscule quantities. By comparing the pattern of $Ba_3(PO_4)_2$ with both syntheses, it is obvious that both products contain this phase, although the peaks are shifted slightly to the left compared to the original peaks. This peak shift is similar to the one that is observed for the decomposed $Ba_3(PO_4)_2$ phase obtained when $KBaPO_4$ is exposed to water (Figure 5.12). This particular situation will be further discussed in section 6.1.3.
Altogether, it is reasonable to conclude that a mechanochemical approach is not an ideal method to use for synthesizing single-phase $KBaPO_4$.

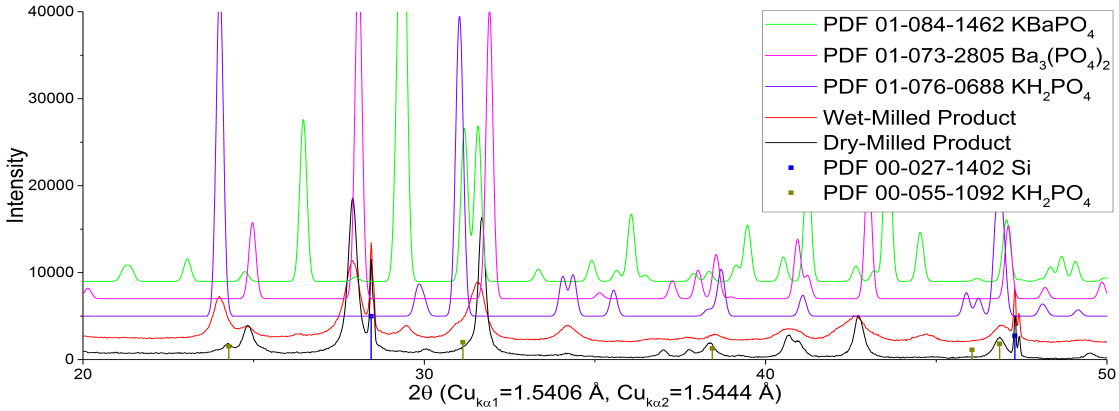

Figure 6.1: A magnified view of the XRD-patterns showing the products from the attempts at mechanochemically synthesizing $KBaPO_4$. Also shown are the patterns for $KBaPO_4$ [46], $Ba_3(PO_4)_2$ [56], and two patterns corresponding to an orthorhombic [58] (01-076-0688) and a tetragonal [59] (00-055-1092) phase of KH_2PO_4.

Thermogravimetric Analysis of the Thermal Decomposition of $KBaPO_4$

A TG analysis was performed on $KBaPO_4$ in order to investigate what compounds would form due to a high-temperature decomposition. Figure 5.5 shows that mass has been lost, and figure 5.6 shows that $Ba_3(PO_4)_2$ has formed during heating at $1400\,^{\circ}C$. Besides the remnants of the $KBaPO_4$ phase that has not had the time to decompose, there are no clear peaks that match any potassium-containing compounds.
Unfortunately, the exhaust from the TG was not analyzed in any way, and any by-products that could have formed and been gasified during decomposition have not been investigated. However, by looking into various species that have the potential to form and be gasified at $1400\,^{\circ}C$, it was found that KOH and P_2O_5, with boiling points of approximately $1300\,^{\circ}C$ and $360\,^{\circ}C$, respectively, were chosen as potential candidates. The decomposition would then occur as the following reaction:

$$6KBaPO_4(s) + 3H_2O(g) \rightleftharpoons 2Ba_3(PO_4)_2(s) + P_2O_5(g) + 6KOH(g) \qquad (6.1.1)$$

6.1.2 Conductivity of $KBaPO_4$

Conductivity Below $200\,^{\circ}C$

Going below $200\,^{\circ}C$, the conductivity starts to increase in humidified air, and the shape of the collected impedance spectra assume a form similar to the ones previously obtained. The increase in conductivity with decreasing temperatures in humidified atmospheres is a behaviour that has previously been observed in porous ceramic samples in

which physisorbed water affects the conductivity [60, 61]. It is believed that this sudden increase in conductivity, and with the further increase upon decreasing the temperature, can be contributed to protonic transport across the surface, as pure surface transport in the adsorbed water layer, and one-dimensional transport between the surface layer and the grain-boundaries [62]. This theory is reinforced by studies of this phenomenon performed on nanocrystalline YSZ [63, 64]. Despite this sudden increase in conductivity in humidified air at low temperatures, this does not mirror the results obtained by Good-enough & Singh in their attempt at hydrating $KBaPO_4$ in steam as they reported. In addition to the observation of an even higher increase in the conductivity, there was an opposite trend where the conductivity would increase with increasing temperatures from 40 to $90\,^{\circ}\mathrm{C}$ with a maximum at $97\,^{\circ}\mathrm{C}$.

Conductivity Above $300\,^{\circ}\mathrm{C}$

Above $300\,^{\circ}\mathrm{C}$, in contrast to the previous section, humidity appears to have no significant effect on the conductivity of $KBaPO_4$. Neither does pO_2.
Figure 5.19 shows a logarithmic plot of the bulk and grain-boundary conductivities for $KBaPO_4$ in dry and humidified air. It is clear that there is no significant difference between dry and humidified air above $300\,^{\circ}\mathrm{C}$ and, due to the low-temperature region being a result of surface transport, only the high-temperature region will be discussed further.
Analysis of $\ln(\sigma T)$ *vs* $\frac{1}{T}$ allows for the estimation of activation energies and pre-exponentials for the conductivities above $300\,^{\circ}\mathrm{C}$. These estimations are summarized in table 5.1. Seeing as both the activation energies and the pre-exponentials are the same in dry and humidified air, humidity seems to have zero effect on the charge carrier in $KBaPO_4$. Additionally, as figure 5.19 indicates that there is also no significant difference in the conductivity when switching from dry to humidified air, the charge carrier in $KBaPO_4$ does not seem to be protonic in nature.
The activation energy for the grain-boundary conductivity is slightly higher than that for bulk, but this behaviour is expected and is a common phenomenon that occurs in materials in which the resistance of the grain-boundary can be attributed to charge carriers being depleted from a space charge region that is adjacent to a grain-boundary core that possesses a net charge [65, 66].
The pre-exponentials in table 5.1 are built up from multiple components, such as site occupancy and vibrational frequency of the mobile ions. By equation 2.1.4, the pre-exponential also contains an entropic factor related to the formation and mobility of the charge carrier [29]. However, delving too deep into the meaning of this value at this stage opens for the possibility of reaching multiple erroneous conclusions.

Conductivity and Defect Model of $KBaPO_4$

According to the defect model proposed, in which protonic species were introduced by hydration, varying the pH_2O should have had an effect on the conductivity. Seeing as there was no significant effect of humidification, a pO_2-dependency was performed in order to investigate whether or not the conductivity of $KBaPO_4$ might be affected by oxygen vacancies. Effectively, this would mean that, by varying the partial pressure of oxygen, the concentration of electronic charge carriers would also increase, and $KBaPO_4$ might have shown signs of being an electronic conductor. Figure 5.18 shows impedance spectra collected for humidified air and humidified oxygen, with pO_2 varying from 0.21 to $1\,\mathrm{atm}$, at $800\,^{\circ}\mathrm{C}$. The spectra show that there is no significant effect of varying pO_2, suggesting that neither oxygen vacancies nor electrons contribute to the conductivity of $KBaPO_4$ in any significant amount, in accordance with initial assumptions

Hence, the results point towards the nature of the conductivity in $KBaPO_4$ being largely ionic.

In $Ba_3(PO_4)_2$, the mobile species is reported to be the Ba^{2+} ion at high temperatures, whereas it at low temperatures and for high pO_2 displays partial electronic conductivity [33]. The crystal structure of $KBaPO_4$ is isostructural to the arcanite structure of β-K_2SO_4 [47], and the predominating defects in K_2SO_4 are said to be potassium Frenkel defects along with the charge carriers reportedly being potassium ions [24]. There is therefore a possibility that the mobile species in $KBaPO_4$ are either potassium or barium defects. The activation energy for bulk conductivity is higher for $KBaPO_4$ ($107\,\mathrm{kJ\,mol^{-1}}$) than for β-K_2SO_4 ($72\,\mathrm{kJ\,mol^{-1}}$), likely owing to the phosphate group being more negatively charged than the sulphate group and thus inhibiting movement of the two cations, but also because of an interaction effect between potassium and the divalent barium

An interesting phenomenon in K_2SO_4 is that the sulphate groups are disordered [67]. Supposedly, these groups rotate and 'slingshot' the cations, thus increasing the mobility. $KBaPO_4$ could possibly exhibit similar properties, however with the PO_4^{3-} groups being larger than and more negatively charged than SO_4^{2-} groups, this effect would intuitively be lower than for K_2SO_4. Consider also that this type of mobility facilitation would depend on the tetrahedral units not being constricted due to the formation of oxygen vacancies because these would exist as pyrophosphates. Despite this, the effect of a similar 'slingshot' effect as in K_2SO_4 could be a topic worth investigating further.

Based on the results of the electrical measurements performed on $KBaPO_4$, the evidence points towards the predominating charge carrier in $KBaPO_4$ being neither protonic nor an oxygen species. Consider the equation for the total conductivity of $KBaPO_4$, as proposed in equation 2.2.27. Based on assumptions regarding the insignificant presence

of defects due to synthesis and sample preparation, the final expression for the total conductivity contained seven terms following from the proposed defects for this compound. These terms corresponded to potassium and barium interstitials and vacancies, oxygen vacancies, hydrated oxygen vacancies ($OH_O^{\cdot}$), and hydroxide interstitials ($OH_i^{/}$). The results point towards the latter three terms not having any significant effect on the conductivity, and the total conductivity of $KBaPO_4$ is therefore assumed to be as in equation 6.1.2, with the only significant terms being those of the Frenkel defects.

$$\sigma_{\text{tot}} = ec_{\text{K}_\text{i}}u_{\text{K}_\text{i}} + ec_{\text{v}_\text{K}}u_{\text{v}_\text{K}} + 2ec_{\text{Ba}_\text{i}}u_{\text{Ba}_\text{i}} + 2ec_{\text{v}_\text{Ba}}u_{\text{v}_\text{Ba}} \tag{6.1.2}$$

The initial defect model for $KBaPO_4$ was proposed in section 2.2.2. Due to the low mobility and high valence of Ba^{2+}, we propose a condensed defect model that only considers potassium Frenkel defects for $KBaPO_4$. The work on acceptor-doped $KBaPO_4$ with additional potassium ($K_{1.01}Ba_{0.99}PO_{4-\delta}$) performed in co-operation with Kevin Nguyen in parallel with this project indicates that the charge carrier in $KBaPO_4$ is the K^+ ion, and that the proposed model of potassium Frenkel defects is a valid model for $KBaPO_4$.

6.1.3 Hydration and Decomposition of $KBaPO_4$

One fascinating idea with $KBaPO_4$ was that it could be hydrated through steaming at $80\,^{\circ}\text{C}$, transforming the crystalline compound into an amorphous phase, and that it would subsequently exhibit a proton conductivity of $1 \times 10^{-2}\,\text{S}\,\text{cm}^{-1}$ below $100\,^{\circ}\text{C}$ [4]. As previously discussed, the inherent conductivity of $KBaPO_4$ is seemingly not of a protonic nature, and the magnitude of the conductivity at $100\,^{\circ}\text{C}$ is immeasurably small. Hydrating $KBaPO_4$ would therefore, potentially, correspond to an immense increase in the conductivity.

Initial Attempts at Hydration

Summarized from the results in section 5.1.2, $KBaPO_4$ was found to, upon exposure to water, decompose into a $Ba_3(PO_4)_2$ phase that contains some potassium. A zoomed view of figure 5.12 is presented in figure 6.2, clearly showing how the peaks are shifted slightly to the left, indicating a cell expansion, as compared with pure $Ba_3(PO_4)_2$. Besides XRD, however, no additional crystallographic analysis was performed on this compound. Therefore, assumptions regarding the incorporation of protons in this compound are based on the results of electrical measurements.
Figure 5.11 shows the cross section of the half that was submerged and left at room temperature. It displays only a partial transformation, however in the same inwards propagating manner as initially discovered upon exposure. Note, however, that prolonged

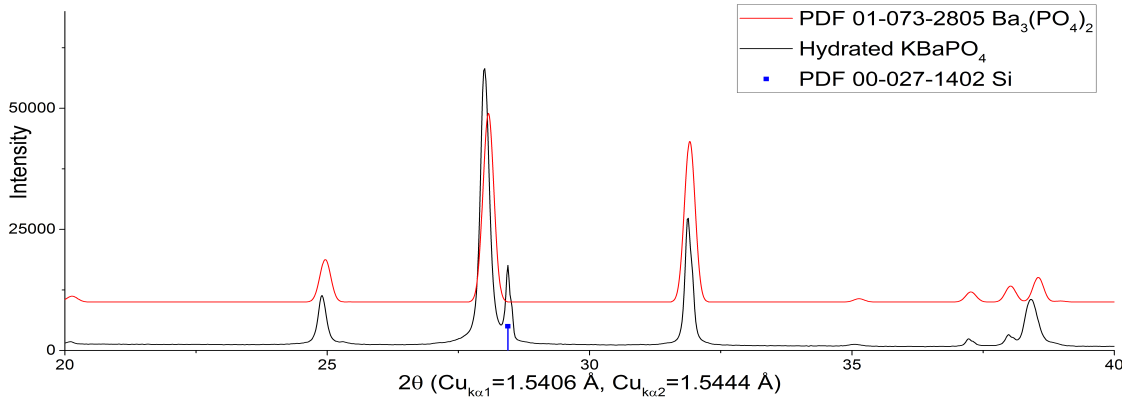

Figure 6.2: A magnified view of the XRD-pattern in figure 5.12, showing the K-containing $Ba_3(PO_4)_2$ phase obtained from the decomposition of $KBaPO_4$ upon exposure to water. The XRD pattern for $Ba_3(PO_4)_2$ [56] is included for comparison in order to display the peak-shift that is observed in the obtained pattern.

exposure to water caused a full transformation even at ambient temperatures, as was seen in a sample that had been left in a sample glass for multiple weeks. How long this process takes at ambient temperatures is unknown. Considering the porosity of the sample, the decomposition reaction could be expected to occur at various locations within the sample as long as water manages to reach the target location. However, the inwards propagation might indicate that the by-product hydrates immediately upon formation, and that it is subsequently dissolved and has to be washed away towards the surface of the sample.

Decomposition of $KBaPO_4$ in Water

The results of hydrating $KBaPO_4$ have now been presented. The evidence indicates that $KBaPO_4$ decomposes into a $Ba_3(PO_4)_2$ phase which is believed to be effectively acceptor doped with potassium, and where the compensating resulting negative charge is compensated by the incorporation of protons. As figure 6.2 shows, there is a shift in the peak-locations for the obtained $Ba_3(PO_4)_2$ phase as compared to pure $Ba_3(PO_4)_2$. However, where the potassium resides in the crystal of $Ba_3(PO_4)_2$ was not further investigated, and could be a topic for further work.

The water for the various hydration attempts was analysed by simple pH paper, and in all cases the water was found to have become more basic after the decomposition process. Based on earlier investigations into K-doped $Ba_3(PO_4)_2$ with the chemical formula $Ba_{3-x}K_xH_x(PO_4)_2$ performed by Haile et al. [5], it is theorized that $KBaPO_4$ decomposes into a similar system, with the decomposition reaction occurring according to equa-

tion 6.1.3.

$$\begin{aligned} &3\mathrm{KBaPO_4(s)} + 2x\mathrm{H_2O(l)} \\ &\qquad \rightleftharpoons \mathrm{K_{3\text{-}x}H_xPO_4(aq)} + \mathrm{Ba_{3\text{-}x}K_xH_x(PO_4)_2(s)} + x\mathrm{Ba(OH)_2(aq)} \end{aligned} \tag{6.1.3}$$

Here, water catalyses the decomposition reaction by providing a medium in which the K_3PO_4 and $Ba(OH)_2$ can dissolve, and be subsequently removed from the reaction site as aqueous species. Because $Ba(OH_2)$ and K_3PO_4 are basic compounds, with the latter reacting with water according to reaction 6.1.4, an explanation is provided as to why the medium in which the decomposition took place had become basic.

$$\mathrm{PO_4^{3-}(aq)} + \mathrm{H_2O(l)} \leftrightarrow \mathrm{HPO_4^{2-}(aq)} + \mathrm{OH^-(aq)} \tag{6.1.4}$$

The decomposition of $KBaPO_4$ depends on the availability of water in the surrounding atmosphere. The sample on which the initial electrical measurements were conducted, showed no signs of any topographical change (By SEM) after prolonged exposure to humidified air ($\approx 3\,\%$ H_2O), suggesting that this low water vapour pressure was not adequate to facilitate decomposition into $Ba_3(PO_4)_2$. The decomposition process requires rearrangement of the ions in order to go from the orthorhombic structure of $KBaPO_4$ to the trigonal $Ba_3(PO_4)_2$. The process requires considerable amounts of water in order to leach out the potassium, and therefore takes place from the external surface and moves inward.

At elevated temperatures, water is evaporated and no liquid phase is present, resulting in $KBaPO_4$ being the stable product at high temperatures. At low temperatures, however, the solvation of K^+ and PO_4^{3-} ions provide the energy required in order to decompose the compound into $Ba_3(PO_4)_2$ in addition to an aqueous solution of K_3PO_4. In steam at $80\,^\circ\mathrm{C}$, the presence of a liquid phase is less pronounced due to the system being equally heated and cold zones in which water could condense are not present. However, the existence of solid hydrates of potassium phosphates provide a way for a liquid phase to form by allowing $K_3PO_4 \cdot xH_2O$ to melt and subsequently dissolve in its own crystal water. Due to the high concentration of potassium inside and the high concentration of water outside, it is reasonable to believe that the interdiffusivity through the pores takes some time, perhaps explaining why the decomposition does not occur on all internal surfaces despite the sample being quite porous.

As previously mentioned, Haile et al. [5] have investigated various K-doped $Ba_3(PO_4)_2$ systems with the general formula $Ba_{3\text{-}x}K_xH_x(PO_4)_2$, synthesized by a co-precipitation method. In this system, the oxygen vacancies that stem from the potassium being an acceptor dopant are hydrated and so the compound effectively contains protons. Due to

$KBaPO_4$ decomposing in water, it is natural to believe that the same situation occurs, and that the compound obtained upon decomposition contains protons.

In Situ Electrical Measurements on $KBaPO_4$ During Steaming

In situ electrical measurements were performed on a sample of $KBaPO_4$ as it was exposed to steam in a cyclic experiment, as described in section 5.1.3. The results of these continuous AC measurements at $1\,\mathrm{kHz}$ are displayed in figure 5.20. Upon steaming, an increase in conductivity was observed, and it kept increasing as the exposure time increased. Upon steaming, the increase could probably be contributed to $KBaPO_4$ decomposing into liquid hydrated K_3PO_4, providing the system with a pathway for protons to move, whereas the sudden drop that occurs upon cooling the water bath back to room temperature can be considered to reflect the dehydration and solidification of K_3PO_4.
The *in situ* electrical measurements did not yield the same results as proposed by Goodenough and Singh [4], and $KBaPO_4$ does in fact decompose upon exposure to water. However, the high conductivity they observed could possibly be contributed to the presence of K^+, OH^- and PO_4^{3-} ions that reside in the molten hydrate of K_3PO_4. Their claim of $KBaPO_4$ transforming into an amorphous phase might be explained by the hydrated K_3PO_4 phase solidifying with an amorphous structure upon cooling down to room temperature. Unfortunately, no such structural investigation was performed for this project.

6.2 Hydrated $KBaPO_4$ - $Ba_{3-x}K_xH_x(PO_4)_2$

6.2.1 Conductivity of K-containing $Ba_3(PO_4)_2$-phase

After making the discovery that $KBaPO_4$ decomposes when it is exposed to water, further investigation was performed on the K-containing $Ba_3(PO_4)_2$ phase that was obtained as the product of this decomposition. Mainly, it would be interesting to investigate the ionic conductivity of this compound and how it varied from previous attempts at acceptor doping $Ba_3(PO_4)_2$ with potassium. A batch of $KBaPO_4$ was prepared according to the normal synthesis route, and subseqeuently steamed at $80\,^\circ\mathrm{C}$. XRD confirmed that the same K-containing $Ba_3(PO_4)_2$ phase as previously discussed had been obtained.
These measurements were conducted upwards from 100 to $300\,^\circ\mathrm{C}$, starting in wet air. This route was chosen due to a theorized decomposition occuring somewhere around $300\,^\circ\mathrm{C}$. Figure 5.23 shows the impedance spectra collected at $200\,^\circ\mathrm{C}$ for $Ba_{3-x}K_xH_x(PO_4)_2$, and there is a clear difference between dry and humidified air and the trend is the same for other temperatures. However, as observed in figure 5.25, a change occurs somewhere between 250 to $300\,^\circ\mathrm{C}$ in dry air, resulting in an increase

in the impedance that does not follow the trend. Most likely, this can be contributed to an irreversible decomposition in which water leaves and the potassium is forced out of the $Ba_3(PO_4)_2$-phase. In fact, as will be clear from section 6.2.2, upon heating $Ba_{3-x}K_xH_x(PO_4)_2$ to high temperatures, it decomposes into a two-phase system consisting of $Ba_3(PO_4)_2$ and $KBaPO_4$. A proposed decomposition reaction is seen in equation 6.2.1.

Upon cooling the system down to $250\,^{\circ}\mathrm{C}$ and switching back to humidified air, an equilibrium similar to that of dry air is instilled, shown in figure 5.24, strengthening the assumption that the dehydration is irreversible. This behaviour is similar to that observed by Haile et al. [26], who reported that $Ba_{3-x}K_xH_x(PO_4)_2$ would initiate a decomposition into $Ba_3(PO_4)_2$ and $KBaPO_4$ somewhere between 100 to $300\,^{\circ}\mathrm{C}$, depending on the potassium content. Their decomposition analysis justifies a potential decomposition taking place somewhere between 250 to $300\,^{\circ}\mathrm{C}$ in dry air. Unfortunately, due to this decomposition having occurred, there was no attempt at looking into a possible isotope effect when switching from H_2O to D_2O, but judging by the previous discussion, protonic charge carriers are highly likely in this compound.

Further analysis of the chemical composition of the compound by EDS, figure 5.9, gave an estimated potassium content of $6\,\mathrm{At}\%$. Compared to the compounds investigated by Haile et al., this was significantly lower than their lowest value of $22\,\mathrm{At}\%$. An interesting note, however, is that they used a synthesis method that required water. Due to the nature of the process used to obtain $Ba_{3-x}K_xH_x(PO_4)_2$ from $KBaPO_4$, it could be that the compound obtained here is the most stable of them all and that it is a K-saturated $Ba_3(PO_4)_2$ phase in the sense that it is not possible for water to leach out any more potassium from it. This could possibly provide an explanation to the seemingly random K-content that they had in their various compounds, and that water used both during synthesis and to subsequently wash the products could have leached out potassium from their compounds. Analysis of $\ln(\sigma T)$ *vs* $\frac{1}{T}$ for our compound gives an activation energy of around $0.57\,\mathrm{eV}$, corresponding very well to the activation energies obtained by Haile et al, again symbolizing that the compound obtained from hydrating $KBaPO_4$ is a variant of $Ba_{3-x}K_xH_x(PO_4)_2$.

Overall, it might seem that exposing $KBaPO_4$ to water provides an easy route to synthesize K-doped $Ba_3(PO_4)_2$, and multiple attempts show similar chemical compositions, indicating the possibility that a stoichiometry of $Ba_{3-x}K_xH_x(PO_4)_2$, for which water is unable to further leach potassium, has been obtained.

6.2.2 Two-Phase System of $Ba_3(PO_4)_2$ and $KBaPO_4$

By heating $Ba_{3-x}K_xH_x(PO_4)_2$ to high temperatures (e.g. $1100\,^{\circ}C$), the result was, as seen in the XRD patterns in figure 5.13, that the compound would decompose into a mixture of $Ba_3(PO_4)_2$ and $KBaPO_4$, possibly according to the decomposition reaction in equation 6.2.1. Note that this reaction assumes a complete decomposition and expulsion of potassium and hydrogen from $Ba_3(PO_4)_2$, although this might not be the case in reality. In this case, the acceptor dopant, the potassium, would go from being compensated by incorporated protons, to being compensated by phosphate vacancies. By comparing the XRD of the compound before and after this heat treatment, figures 5.13 and 5.14, it is clear that the previously observed peak-shift has vanished. This could indicate that there is no potassium in the $Ba_3(PO_4)_2$ phase, however this could also be because the potassium content is so small that it is, effectively, undetectable by the instruments used. Nonetheless, at the temperature used ($1100\,^{\circ}C$), it is reasonable to assume that the product of the decomposition reaction does not contain any protons, although the increased number of oxygen vacancies, as seen by equation 6.2.1, could possibly allow for hydration and proton conductivity.

$$Ba_{3-x}K_xH_x(PO_4)_2 \rightleftharpoons Ba_{3-2x}P_{2-x}O_{8-4.5x} + xKBaPO_4 + xH_2O \tag{6.2.1}$$

The initial potassium content of the $Ba_{3-x}K_xH_x(PO_4)_2$ compound obtained by subjecting $KBaPO_4$ to water was estimated, by EDS, to be around $6\,At\%$. Iwahara et al. attempted to synthesize K-doped $Ba_3(PO_4)_2$ according to a high-temperature synthesis route [6]. They denoted their composition as $Ba_{3(1-x)}K_{3x}(PO_4)_{2-x}$, without inherent protons as compared to $Ba_{3-x}K_xH_x(PO_4)_2$. They found that when attempting to incorporate too much potassium, some of it would emigrate and form $KBaPO_4$. They reached the conclusion that the solubility limit of potassium in $Ba_3(PO_4)_2$ is below $3\,At\%$. By subjecting $KBaPO_4$ to water, the resulting compound contains more potassium than Iwahara et al. managed to incorporate, possibly owing to the high temperatures that they used for their synthesis route, and that this would facilitate the transport of potassium out of the $Ba_3(PO_4)_2$ phase.

It might be that the product obtained by the decomposition reaction in equation 6.2.1 is in fact a mix of $Ba_{3(1-x)}K_{3x}(PO_4)_{2-x}$ and $KBaPO_4$. Comparing $Ba_{3(1-x)}K_{3x}(PO_4)_{2-x}$ and $Ba_{3-2x}P_{2-x}O_{8-4.5x}$, the former is acceptor doped with potassium and the latter contains only barium vacancies. In both cases, however, the compensating defect is thought to be phosphate vacancies. As phosphate defects intuitively indicate that there are oxygen vacancies in the compound, it might be possible that these can be hydrated in humidified atmospheres, thus giving protons.,

Despite the product of equation 6.2.1 being a two-phase system consisting of $Ba_3(PO_4)_2$ and a minor secondary $KBaPO_4$ phase, and not the single-phase $Ba_{3(1-x)}K_{3x}(PO_4)_{2-x}$ phase, it would be interesting to see if this compound shows similar conductivities as $Ba_{3(1-x)}K_{3x}(PO_4)_{2-x}$, and to see how the electrical conductivity of the system would be compared to the system investigated by Iwahara et al.

The Conductivity of The Two-Phase System of $Ba_3(PO_4)_2$ and $KBaPO_4$

Iwahara et al. performed electrical measurements on $Ba_{3(1-x)}K_{3x}(PO_4)_{2-x}$. Their results gave conductivities between 1×10^{-4} and $1 \times 10^{-3}\,\mathrm{S\,cm^{-1}}$ in humidified air between 500 to $1000\,^{\circ}\mathrm{C}$.

As is clear from the impedance spectra in figure 5.26, humidification has a large effect on the impedance of the sample. Even though they are not shown here, at $600\,^{\circ}\mathrm{C}$, the bulk contribution starts to become so small that it effectively disappears from the impedance spectra. At $700\,^{\circ}\mathrm{C}$, the first part of the impedance spectra corresponds to a grain-boundary process, and the values for the bulk conductivity are therefore extracted from fits of spectra collected below $600\,^{\circ}\mathrm{C}$. By investigating the impedance spectra collected in humidified air and humidified O_2 (E.g. figure 5.27 collected at $500\,^{\circ}\mathrm{C}$), it is clear that pO_2 shows an insignificant effect on the conductivity of the sample, both in the bulk and the grain-boundary. This does not indicate that oxygen vacancies are not present, but rather that they themselves are not the predominating charge carriers in the compound, perhaps due to their mobility. In fact, as previously stated, the predominating charge carrier in $Ba_3(PO_4)_2$ is the barium ion [33], and it is therefore reasonable to assume that oxygen vacancies will not be the predominating defect in our compound either. As was discussed regarding equation 6.2.1, there is an increased number of oxygen vacancies after decomposition of $Ba_{3-x}K_xH_x(PO_4)_2$. These might be available for hydration, and might explain the increased conductivity in humidified air. To determine whether or not the charge carrier might be protonic, in addition to observing the difference in dry and humidified atmospheres, an isotope exchange was performed. The impedance spectra in figure 5.28 shows that there is a slight difference in the bulk impedance when switching from H_2O to D_2O. Compared with the effect of pO_2 (Figure 5.27), the difference due to the isotope exchange is much more significant. Figure 5.29 shows the result of the continuous measurements at $10\,\mathrm{kHz}$ as the humidifying step is switched from H_2O to D_2O. The change is small, but measurable, and it is possible that the charge carrier in the two-phase system is protonic.

The grain-boundaries are significant in the measured sample. Iwahara et al. sintered their sample at $1350\,^{\circ}\mathrm{C}$ for 15 to 24 hours. Comparing this to the process used here, $1100\,^{\circ}\mathrm{C}$ for 8 hours, it is reasonable to assume that they achieved a denser sample with

less contributions from grain-boundaries. Therefore, the grain-boundary conductivity is not discussed in depth here. However, the increase in the conductivity of the grain-boundary due to humidity could possibly be explained by considering the concept of space charge [68, 69]. An oxygen vacancy is hydrated according to equation 2.2.9, with the protons preferably dissolving in the grain-boundary core and the oxide ions annihilating oxygen vacancies in the bulk [70]. Due to oxygen vacancies effectively depleting more than protons (Because they possess a double effective charge), the protons being light and therefore move more easily than oxide ions, and due to the grain-boundaries being more easily accessible for infiltrating water, the conductivity of the grain-boundary is thus expected to increase.

Figure 5.30 shows the bulk conductivity of the two-phase system. The magnitudes of the conductivity are very high and, considering that this system is stable to very high temperatures, as compared to $Ba_{3-x}K_xH_x(PO_4)_2$ that decomposes around $300\,^{\circ}\mathrm{C}$, the system in question is very promising. In fact, at $600\,^{\circ}\mathrm{C}$, the bulk conductivity is slightly higher than $1 \times 10^{-3}\,\mathrm{S\,cm^{-1}}$, which is more than one order of magnitude larger than the $Ba_{3(1-x)}K_{3x}(PO_4)_{2-x}$ system on which Iwahara et al. did their measurements, and only one order of magnitude lower than that of $BaZrO_3$.

The synthesis route for this system is very simple: Synthesize $KBaPO_4$ and boil it in water to obtain $Ba_{3-x}K_xH_x(PO_4)_2$ saturated with potassium, then heat the product to high temperatures and obtain a two-phase mixture of $Ba_3(PO_4)_2$ and $KBaPO_4$. However, whether or not the presence of the $KBaPO_4$ phase affects the conductivity positively or negatively needs to be further investigated. It might be that the dispersed $KBaPO_4$ phase actually promotes the conductivity of the $Ba_3(PO_4)_2$ phase, but at this point in time this would just be speculation.

Iwahara et al. do not specify any values for the activation energy for the conduction process in their work. From the measurements performed here, however, the activation energy was found to be about $0.66\,\mathrm{kJ\,mol^{-1}}$ in both dry and humidified air. These values are shown in table 5.3

6.2.3 Comparison of $KBaPO_4$, $Ba_{3-x}K_xH_x(PO_4)_2$, Two-Phase System of $Ba_3(PO_4)_2$ and $KBaPO_4$, and Pure $Ba_3(PO_4)_2$

Figure 6.3 shows the conductivities of $KBaPO_4$, $Ba_{3-x}K_xH_x(PO_4)_2$, the composite of $Ba_3(PO_4)_2$ and $KBaPO_4$, and single-phase $Ba_3(PO_4)_2$[1], in dry and humidified air. From the plot, it is clear that $Ba_3(PO_4)_2$ and $KBaPO_4$ are very poor conductors, with $KBaPO_4$ not displaying any reaction towards humidification, thus indicating that $KBaPO_4$ is not a

[1]The sample of $Ba_3(PO_4)_2$ was made with powder of $Ba_3(PO_4)_2$ bought from Sigma-Aldrich.

protonic conductor. It is clear that the hydrogen containing compound $Ba_{3-x}K_xH_x(PO_4)_2$, as obtained from exposing $KBaPO_4$ to water, displays ionic (protonic) conductivity significantly higher than either $Ba_3(PO_4)_2$ or $KBaPO_4$. Furthermore, the two-phase system consisting of $Ba_3(PO_4)_2$ and $KBaPO_4$, obtained when heating $Ba_{3-x}K_xH_x(PO_4)_2$ to high temperatures, also displays higher conductivities than $KBaPO_4$ or $Ba_3(PO_4)_2$. The latter system is stable to much higher temperatures than $Ba_{3-x}K_xH_x(PO_4)_2$ and is a much more viable electrolyte. Table 6.1 shows the activation energies for the compounds measured in-house, as well as some values found in literature. Unfortunately, Iwahara et al. did not provide any values for the activation energy for their compound $Ba_{3(1-x)}K_{3x}(PO_4)_{2-x}$. $KBaPO_4$ was found to have a very large activation energy compared to the other compounds. If, as has been thoroughly discussed, the charge carrier in this compound is the potassium ion, then the large activation energy can be taken to reflect just that; it is more difficult to activate and move the potassium ions. Following this argument, it is unlikely that the charge carrier in the two-phase system of $Ba_3(PO_4)_2$ and $KBaPO_4$ is potassium due to the activation energy being significantly lower than for pure $KBaPO_4$. The value is somewhat larger than for $Ba_{3-x}K_xH_x(PO_4)_2$, but due to the nature of the charge carrier in $Ba_{3-x}K_xH_x(PO_4)_2$ having been investigated and is believed to be protonic [5], it is reasonable to assume that the charge carrier in our two-phase system is also protonic. However, this topic requires further investigation.

Table 6.1: Comparison of the estimated values for the activation energies for the bulk conductivities, obtained from the analysis of $\ln(\sigma T)$ *vs* $\frac{1}{T}$ on the conductivity data for the various compounds in this project, as well as values found in literature. $Ba_3(PO_4)_2$-in-house stems from a sample produced with $Ba_3(PO_4)_2$ bought from Sigma-Aldrich.

	Atmosphere (Wet/Dry)	Activation Energy E_a [eV]
$KBaPO_4$	Wet	1.10 ± 0.04
$Ba_{3-x}K_xH_x(PO_4)_2$ [5]	Dry	0.53 to 0.58
$Ba_{3-x}K_xH_x(PO_4)_2$	Dry	0.53 ± 0.01
$Ba_3(PO_4)_2$ [5]	Dry	0.36
$Ba_3(PO_4)_2$-in-house	Wet	0.48 ± 0.03
$Ba_3(PO_4)_2$ + $KBaPO_4$	Wet	0.67 ± 0.01

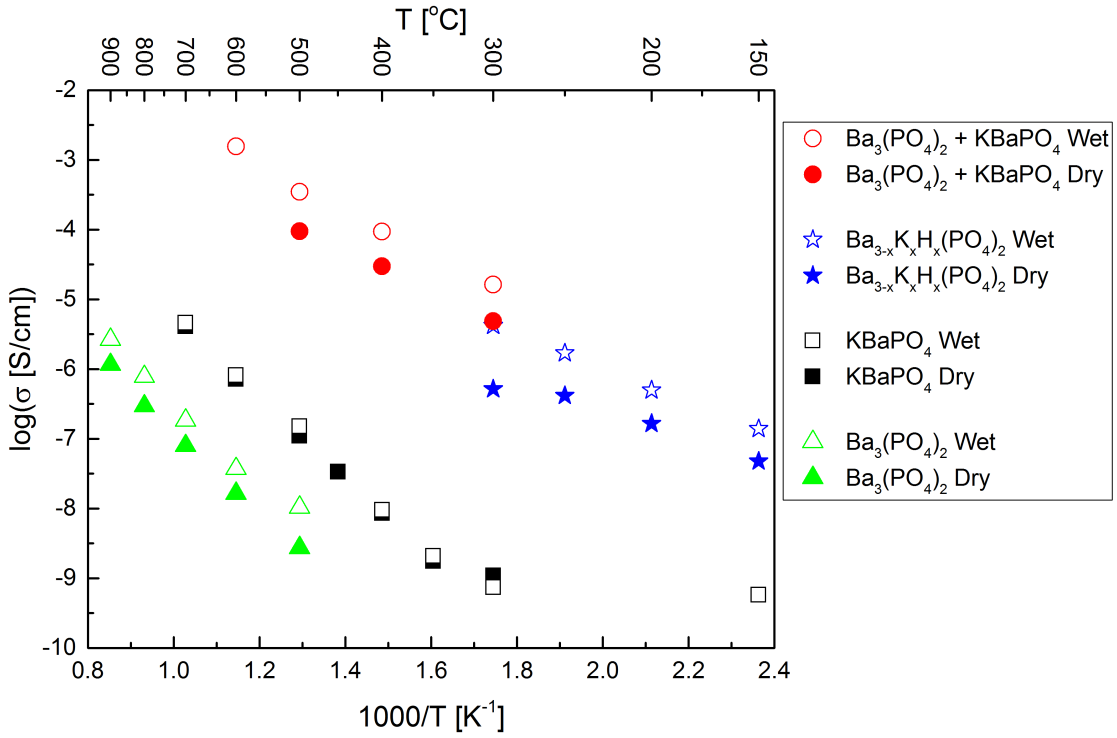

Figure 6.3: A plot comparing the total conductivities of $KBaPO_4$, $Ba_{3-x}K_xH_x(PO_4)_2$, the two-phase system of $Ba_3(PO_4)_2$ and $KBaPO_4$, and single-phase $Ba_3(PO_4)_2$, in dry and humidified air.

6.3 Silicates and Related Compounds ($ABHXO_4$)

The goal of this project was to discover and characterize new ionic conductors. In addition to investigating $KBaPO_4$ based on Goodenough and Singh's' claim [4], a secondary approach was to be found in the world of the orthosilicates. As for other compounds exhibiting superprotonic transitions (E.g. CsH_2PO_4), orthosilicates also possess a variety of the XO_4 group which seems to be a requirement for these transitions to occur. Inspiration was drawn from $NaCaHSiO_4$ and the reports by Haile [25], and a series of similar syntheses were attempted in order to obtain new compounds on the form $ABHXO_4$ (A=Li, Na or K. B=Ca, Sr or Ba. X=Si, Ge or Sn).

6.3.1 Synthesis of $NaCaHSiO_4$ and Other Orthosilicates

$NaCaHSiO_4$ was synthesized successfully according to [25], with the XRD pattern in figure 5.31 showing a seemingly pure phase. However, as indicated by table 5.4, all other syntheses attempted in the same manner as $NaCaHSiO_4$ with only the reactants varying

between different alkali and alkaline earth hydroxides, as well as GeO_2 and SnO_2, turned out to be unsuccessful. The data in the table stems from XRD of the washed products of the syntheses. Therefore, in the cases where alkali and alkaline earth hydroxides are present, this is due to the remaining hydroxides not being fully removed upon washing the products.
Other than $NaCaHSiO_4$, the only synthesis that yielded a seemingly pure product was from the attempt at synthesizing $NaSrHSiO_4$, with the product being Sr_2SiO_4. Conventional methods of synthesizing Sr_2SiO_4 utilize stoichiometric mixtures of $SrCO_3$ and SiO_2, followed by calcination at temperatures around $1300\,°C$ for 30 hours [71]. So even though the desired product was not obtained, a hydrothermal approach of synthesizing Sr_2SiO_4 has been found.
Nonetheless, none of these syntheses resulted in single phase products containing hydrogen, and so only $NaCaHSiO_4$ was characterized by impedance spectroscopy.
BaH_2SiO_4 was synthesized according to [50], with the XRD pattern in figure 5.37 showing a single phase. Collectively, both of $NaCaHSiO_4$ and BaH_2SiO_4 were easily synthesized.

6.3.2 Conductivities and Defect Models of Orthosilicates

$NaCaHSiO_4$

The impedance spectra in figure 5.34 show slightly depressed semicirlces that could be fitted to equivalent circuits consisting of single RQ sub-circuits, yielding specific capacitances of around $15\,pF$, indicating that the measured conductivity belongs to the bulk. Figures 5.32 and 5.33 show the surface of the sample that was measured. This image was collected after treating the sample at $400\,°C$ for several hours in hopes of densifying the sample. Unfortunately, the sample was very porous and the relative density was estimated to be around $65\,\%$, with an average grain size of less than $10\,\mu m$.
As seen in the conductivity plot in figure 5.36 (And the impedance spectra in figure 5.34), there is a clear difference between the conductivity in dry and humidified air, and a closer investigation of the difference between H_2O and D_2O (Figure 5.35) suggests that the conductivity is protonic in nature. In contrast to the report by Haile, the conductivity of $NaCaHSiO_4$ was measured above $260\,°C$ and up to a temperature of $400\,°C$ (Above which the compound is reported to decompose), in order to investigate whether or not any sudden changes in conductivity would occur. The conductivity of the sample is estimated to be $1.2 \times 10^{-8}\,S\,cm^{-1}$ at $250\,°C$ in dry air, one order of magnitude lower than that of the as-synthesized sample measured by Haile. This is in accordance

with their results where they found that larger grained polycrystalline samples exhibited higher conductivities, as their sample had larger grains. The conductivity plot in figure 5.36 shows no sudden change in the conductivity in the measured temperature range, and hence it is safe to conclude that $NaCaHSiO_4$ does not undergo a transition into a superprotonic state.

As has just been discussed, the conductivity increases in humidified air, and there is a positive dependency of pH_2O. Combined with the effect seen when switching to D_2O, it is safe to say that the charge carrier in $NaCaHSiO_4$ is a protonic species. However, with measurements of only two different pH_2O-values, it is not possible to discern which of the two models proposed in the theory section that are most likely to be valid. In fact, it is not possible to determine which region of the Brouwer diagrams we are in. However, considering that the conductivity increases due to humidity, we can possibly disregard $v_H^{/}$ as being the charge carrier, as its concentration decreases in both models. The same can be said for $v_O^{\cdot\cdot}$. Both models indicate that the concentration of both $OH_i^{/}$ and $OH_O^{\cdot}$ increase with increasing pH_2O, so these are both viable candidates. An effect of pO_2 might have indicated that the first model was a good choice, due to it containing oxygen vacancies that might have been affected. In this case, the evidence would point towards $OH_O^{\cdot}$ being the predominating charge carrier. However, this measurement was not performed. One possibility is that the increase in conductivity can simply be contributed to chemisorbed water.

Table 5.5 summarizes the estimations of the activation energies for the conductivities of $NaCaHSiO_4$. The value in dry air, $0.88\mathrm{eV}$, coincides with the average value of $0.9\mathrm{eV}$ obtained by Haile et al. when performing measurements in Argon. The activation energy was found to be being lower in the humidified atmosphere ($0.77\,\mathrm{eV}$), possibly caused by hydration of oxygen vacancies, effectively giving more potential charge carriers in the structure thus decreasing the overall energy required to form and transport said charge carriers. Additionally, the pre-exponential was found to be lower in humidified air, a result that could be taken to reflect that the inclusion of more charge carriers through humidification increases the fractional occupancy of the mobile ion sites, according to equation 2.1.4. If this is the case, then perhaps the hydroxide interstitials due to equation 2.2.37 have some significance.

BaH_2SiO_4

The impedance spectra in figure 5.38 show slightly depressed semicirlces that could be fitted to equivalent circuits consisting of single RQ sub-circuits, yielding specific capacitances of around $17\,\mathrm{pF}$, indicating that the measured conductivity belongs to the bulk. Due to BaH_2SiO_4 decomposing at relatively low temperatures (Around $320\,^{\circ}\mathrm{C}$ [50]),

the sample could not be effectively sintered and the relative density was estimated to be around $71\,\%$.

The conductivity plot in figure 5.39 shows the bulk-conductivity of BaH_2SiO_4. The magnitude of the conductivity of BaH_2SiO_4 ($1 \times 10^{-8}\,\mathrm{S\,cm^{-1}}$ at $250\,^{\circ}\mathrm{C}$) was found to slightly larger than previous reports by Haile et al. [26], with an estimated activation energy of about $0.88\,\mathrm{eV}$ in humidified air, although the overall conductivity of the compound is low compared to other solid acids (Table 6.2). The activation energy for BaH_2SiO_4 in humidified air is almost the same as the value for $NaCaHSiO_4$ in dry air. Although the effect of humidity was less pronounced for BaH_2SiO_4 than for $NaCaHSiO_4$, a conductivity-enhancing effect was observed, and the discussion presented for $NaCaHSiO_4$ is also valid for BaH_2SiO_4. Seeing as BaH_2SiO_4 has a hydrogen content that is double that of $NaCaHSiO_4$, the low increase could reflect that the concentration of charge carriers is not drastically affected by humidity, although there is some effect.

Peculiarly, Haile et al. reported conductivity values of BaH_2SiO_4 up to $400\,^{\circ}\mathrm{C}$ despite stating, in the same report, that the decomposition temperature of BaH_2SiO_4 is around $320\,^{\circ}\mathrm{C}$. TG measurements performed on BaH_2SiO_4 as part of this project indicate that BaH_2SiO_4 decomposes irreversibly to $BaSiO_3$ at slightly lower temperatures (Initiating between 280 to $300\,^{\circ}\mathrm{C}$). Additionally, TG analysis was performed in high water vapour pressures to investigate whether the compound would be more stable under these conditions. Unfortunately, the compound decomposed at the same temperature as for the measurements conducted in an ambient atmosphere.

Unfortunately, due to lack of information regarding sample preparation and measurements conditions used by Haile et al., it is difficult to conclude what set of results provide the most accurate results regarding the conductivity of BaH_2SiO_4. Therefore another separate investigation into the system is recommended.

Comparison With Other Solid Acids

In table 6.2 there is a list of various solid acids and their magnitudes of conductivities and their activation energies for formation and transport of charge carriers. In all compounds, the charge carrier is reported to be protonic, and the transport mechanism is defect-based. Note that, overall, the conductivities of all the compounds are very low. $CsHSO_4$ has a superprotonic phase in which the conductivity increases tremendously, however that is not the topic of this discussion.

By the data in the table, it would appear that compounds with large cations have low activation energies. It would also seem as the size of the anionic group has an effect, with a larger anionic group giving a larger activation energy, as is seen when comparing

$CsHSO_4$ and BaH_2SiO_4, or even KH_2PO_4 and KH_2AsO_4. Thus, the increase in stability that is gained upon switching to a larger and more attracting anionic group is somewhat lost due to the increase in the activation energy of the compound.
The data in the table support the assumption that smaller cations and increased electrostatic bonding seems to inhibit proton conduction. However, note that $NaCaHSiO_4$ has a higher conductivity than BaH_2SiO_4, despite the activation energy being roughly the same. As $NaCaHSiO_4$ was earlier found to exhibit a conductivity of $1.3 \times 10^{-7}\,\mathrm{S\,cm^{-1}}$ at $250\,^{\circ}\mathrm{C}$, one order of magnitude lower than the room-temperature conductivity of $CsHSO_4$, further investigations into solid acid silicates analogous to $NaCaHSiO_4$ are recommended.

Table 6.2: Comparison of the magnitudes of the conductivities and activation energies for some solid acids. 'RT' denotes room-temperature ($\approx 25\,^{\circ}\mathrm{C}$). Measurements conducted in dry atmospheres.

	σ [$\mathrm{S\,cm^{-1}}$]	T [°C]	E_a [eV]	Reference
From this project				
$NaCaHSiO_4$	$1.2 \cdot 10^{-8}$	250	0.9	
BaH_2SiO_4	$1 \cdot 10^{-8}$	250	0.88	
Other Sources				
$KHSO_4$	$1 \cdot 10^{-8}$	RT	0.64	[72]
$CsHSO_4$	$1 \cdot 10^{-6}$	RT	0.3	[73]
KH_2PO_4	$1 \cdot 10^{-8}$	RT	0.55	[74]
KH_2AsO_4	$1 \cdot 10^{-8}$	RT	0.66	[75]
$NaCaHSiO_4$	$1.3 \cdot 10^{-7}$	250	0.9	[25]

Chapter 7

Conclusions and Further Work

7.1 $KBaPO_4$

$KBaPO_4$ was successfully synthesized through a high-temperature solid state reaction between KH_2PO_4 and $BaCO_3$. An alternative mechanochemical route with the same reactants gave instead a product consisting of multiple phases, and a poor yield of $KBaPO_4$. Decomposition of the compound at $1400\,^{\circ}\mathrm{C}$, according to equation 6.1.1, resulted in a mixture of $Ba_3(PO_4)_2$ and $KBaPO_4$, with phosphorous and potassium most likely having decomposed to P_2O_5 and KOH, and subsequently evaporated.

7.1.1 Ionic Conductivity of $KBaPO_4$

Judging by the impedance spectra obtained for $KBaPO_4$ in dry and humidified atmospheres, in addition to seeing the lack of effect of varying the pO_2, the natural conclusion to draw would be that the nature of the conductivity in $KBaPO_4$ is neither protonic nor electronic. The conductivity was overall found to be very low; $2 \times 10^{-6}\,\mathrm{S\,cm^{-1}}$ at $600\,^{\circ}\mathrm{C}$ in both dry and humidified air, with an activation energy exceeding $1\,\mathrm{eV}$. Based on the initial assumption that Frenkel defects were the predominating defects in $KBaPO_4$, a condensed defect model was proposed to only contain potassium Frenkel defects. The parallel project on acceptor doping $KBaPO_4$ with excess potassium by Nguyen strengthens the assumption that the mobile species in $KBaPO_4$ are K^+ ions.

7.1.2 Hydration of $KBaPO_4$

Attempts at hydrating $KBaPO_4$ in steam did not yield an amorphous phase displaying great protonic conductivity, as proposed by Goodenough & Singh. In fact, exposing $KBaPO_4$ to water, even at room temperature, promoted a decomposition (Equation 6.1.3) in which potassium was cast out from the system, yielding a $Ba_3(PO_4)_2$ phase containing a low amount of potassium, as seen by a peak-shift in the $Ba_3(PO_4)_2$ peaks in figure 6.2. Electrical measurements and other characterization methods led to the belief that the system obtained was similar to $Ba_{3-x}K_xH_x(PO_4)_2$, formerly investigated by Haile et al. [5], and the charge carrier in this system is believed to be a protonic species, with an activation energy of about $0.57\,\mathrm{eV}$. The conductivity of the compound is higher than that of $KBaPO_4$, $1.6 \times 10^{-6}\,\mathrm{S\,cm^{-1}}$ at $250\,^{\circ}\mathrm{C}$ in humidified air, yet due to the instability of the compound with respect to temperature, it is a poor choice compared to other materials.

Two-Phase System of $Ba_3(PO_4)_2$ and $KBaPO_4$

Upon heating $Ba_{3-x}K_xH_x(PO_4)_2$ to high temperatures, a decomposition, possibly according to equation 6.2.1, was found to take place. The result was the formation of a two-phase system consisting of $Ba_3(PO_4)_2$ and $KBaPO_4$, with $KBaPO_4$ being in the minority. Electrical measurements on this phase gave indications that the charge carrier is protonic, with an activation energy of $0.67\,\mathrm{eV}$, and a bulk conductivity slightly higher than $1 \times 10^{-3}\,\mathrm{S\,cm^{-1}}$ at $600\,^{\circ}\mathrm{C}$ in humidified air. This was found to be one order of magnitude higher than the system $Ba_{3(1-x)}K_{3x}(PO_4)_{2-x}$ investigated by Iwahara et al., and one order of magnitude lower than for the well-known $BaZrO_3$.

7.2 Silicates and Related Compounds

7.2.1 $NaCaHSiO_4$ and $ABHXO_4$

$NaCaHSiO_4$ was successfully synthesized and subsequently characterized. Its conductivity displayed a linear trend up to a temperature of $400\,^{\circ}\mathrm{C}$, over which it would decompose. With a conductivity of about $1.2 \times 10^{-8}\,\mathrm{S\,cm^{-1}}$ at $250\,^{\circ}\mathrm{C}$, and an activation energy of $0.9\,\mathrm{eV}$, the results correspond well with earlier reports by Haile et al. For $NaCaHSiO_4$, we propose a defect model in which hydroxide and hydrogen interstitials are the predominating defects.

Unfortunately, none of the other $ABHXO_4$ systems could be synthesized by the same method (Table 5.4), however a hydrothermal route of synthesizing Sr_2SiO_4 has been found.

7.2.2 BaH_2SiO_4

The BaH_2SiO_4 synthesized by a hydrothermal approach for this project was found to exhibit a conductivity of $2.5 \times 10^{-8}\,\mathrm{S\,cm^{-1}}$ at $200\,^{\circ}\mathrm{C}$ in humidified air, with an activation energy of $0.88\,\mathrm{eV}$, similar to that of $NaCaHSiO_4$. This conductivity is one order of magnitude larger than that reported by Haile et al. The compound was found to initiate a decomposition around $300\,^{\circ}\mathrm{C}$, independent of whether or not the surrounding atmosphere contained a high water vapour pressure. This investigation led to a discrepancy due to Haile et al. reporting values for the conductivity above $300\,^{\circ}\mathrm{C}$.

As for $NaCaHSiO_4$, we propose a defect model in which hydroxide and hydrogen interstitials are the predominating defects.

7.3 Further Work

In contrast to acceptor doping $KBaPO_4$ with excess potassium, it could be worth investigating the possibility of donor doping the system with excess barium in order to further investigate the likelihood of potassium ions being the predominating charge carrier in the compound. Additionally, diffusion studies could be performed in order to determine the mobility of the potassium ions.
Additionally, further investigations of the $Ba_{3-x}K_xH_x(PO_4)_2$ system obtained upon exposure of $KBaPO_4$ to water is recommended. This could include a proper determination of the potassium content and subsequent comparison to the results by Haile et al.
The two-phase system obtained upon heating $Ba_{3-x}K_xH_x(PO_4)_2$ to high temperatures should be investigated further, as it displays great thermal stability, a high conductivity of a protonic species, and because the system is easy to obtain. Particularly, the potassium content of the $Ba_3(PO_4)_2$ phase should be properly determined, and the results compared with those by Iwahara et al. A structural investigation should be performed in order to determine the location and transport mechanism of the protonic species. Additionally, the effect, whether positive or negative, of the minority $KBaPO_4$ phase should be studied. Seeing as the conductivity appears to reside slightly more than one order of magnitude lower than for $BaZrO_3$, attempts at refining the system should be attempted as to obtain even higher conductivities.
With respect to $NaCaHSiO_4$ and BaH_2SiO_4, their defect chemistries should be investigated further, and both the mobility and the transport mechanisms of the protonic species should be characterized in order for develop a better understanding of these types of materials.
Additionally, due to BaH_2SiO_4 decomposing around $300\,^{\circ}\mathrm{C}$, and earlier reports contain conductivity data above this temperature, we recommend yet another, separate investigation into the thermal stability of BaH_2SiO_4, as well as the electrical conductivity of the compound.

Appendix A

Appendix

A.1 Derivation of Relative Uncertainties

We start with this simple expression for error propagation through a product of factors with individual uncertainties:

$$R = a \cdot x^n \cdot y^m \cdot z^{-k}$$

where a is a constant value without any error. The relative uncertainty of this expression will then be given as

$$\frac{\delta R}{R} = \sqrt{(n\frac{\delta x}{x})^2 + (m\frac{\delta y}{y})^2 + (k\frac{\delta z}{z})^2}$$

where δR denotes the error of the value R.

The specific conductivity of a material can be calculated by $\sigma = \frac{l}{A_{\text{el}} \cdot R}$ where l, A_{el} and R represent the thickness of the sample, the area of the electrode, and the resistance of the material, respectively. If the resistance is considered to be accurate (i.e. without any error), the relative uncertainty of this expression can be estimated based on l and A_{el}:

$$\sigma = \frac{l}{R \cdot A_{\text{el}}} = \frac{l}{R \cdot 2\pi \cdot (\frac{d_{\text{el}}}{2})^2} = \frac{2}{R \cdot \pi} \cdot \frac{l}{d_{\text{el}}^2} = C \cdot l^1 \cdot d_{\text{el}}^{-2}$$

and the relative uncertainty will be given as

$$\frac{\delta \sigma}{\sigma} = \sqrt{(\frac{\delta l}{l})^2 + (\frac{\delta d_{\text{el}}}{d_{\text{el}}})^2}$$

When correcting for the porosity of the sample (by considering the relative density), the error in the relative density must be included in the calculations. The relative density is

given as

$$\rho_{\text{rel}} = \frac{\rho_{\text{calc}}}{\rho_{\text{theory}}} = \frac{\frac{m}{V}}{\rho_{\text{theory}}} = D \cdot \frac{m}{2\pi \cdot (\frac{d}{2})^2 \cdot l} = D \cdot \frac{2m}{\pi \cdot d^2 \cdot l} = \frac{2D}{\pi} \cdot \frac{m}{d^2 \cdot l} = E \cdot m^1 \cdot d^{-2} \cdot l^{-1}$$

where m, d and l represent the mass, the diameter and the thickness of the sample, respectively. In this case, the relative uncertainty will be given as

$$\frac{\delta\rho_{\text{rel}}}{\rho_{\text{rel}}} = \sqrt{(\frac{\delta m}{m})^2 + (\frac{\delta l}{l})^2 + (2\frac{\delta d}{d})^2}$$

The specific conductivity can be corrected for porosity by

$$\sigma_{\text{corrected}} = \frac{\sigma}{\rho_{\text{rel}}^2} = \frac{C \cdot l^1 \cdot d_{\text{el}}^{-2}}{(E \cdot m^1 \cdot d^{-2} \cdot l^{-1})^2} = \frac{C}{E^2} \cdot \frac{l^1 \cdot d_{\text{el}}^{-2}}{m^2 \cdot d^{-4} \cdot l^{-2}} = F \cdot l^3 \cdot d_{\text{el}}^{-2} \cdot m^{-2} \cdot d^4$$

and the relative uncertainty will be given as

$$\frac{\delta\sigma_{\text{corrected}}}{\sigma_{\text{corrected}}} = \sqrt{(3\frac{\delta l}{l})^2 + (2\frac{\delta d_{\text{el}}}{d_{\text{el}}})^2 + (2\frac{\delta m}{m})^2 + (4\frac{\delta d}{d})^2}$$

By comparing the magnitudes of the various terms, it is possible to reduce this expression. Generally, if one value is 100 times lower than another, it is discarded from the expression.

Bibliography

1. Kreuer, K. D. Proton-Conducting Oxides. *Annual Review of Materials Research* **33,** 333–359 (2003).
2. Haile, S. M., Boysen, D. A., Chisholm, C. R. I. & Merle, R. B. Solid acids as fuel cell electrolytes. *Nature* **410,** 910–913 (2001).
3. Elstad, A. A., Nguyen, K., Sartori, S. & Norby, T. *On the conductivity of KBaPO4 and its decomposition in steam and water* Submitted.
4. Goodenough, J. B. & Singh, P. Review - Solid Electrolytes in Rechargeable Electrochemical Cells. *Journal of The Electrochemical Society* **162,** A2387–A2392 (2015).
5. Chisholm, C. R., Toberer, E. S., Louie, M. W. & Haile, S. M. Engineering the Next Generation of Solid State Proton Conductors: Synthesis and Properties of Ba3-xKxHx(PO4)2. *Chemistry of Materials* **22,** 1186–1194 (2010).
6. Iwahara, H., Warashina, K., Shimura, T. & Matsumoto, H. Proton Conduction In The Sintered Phosphate Based On Ba3(PO4)2. *Journal of The Electrochemical Society* **97,** 1–7 (1998).
7. U.S. Energy Information Administration. *International Energy Outlook 2016* Analysis & Projections (U.S. Energy Information Administration, May 11, 2016).
8. Murray, E. P., Tsai, T. & Barnett, S. A. A direct-methane fuel cell with a ceria-based anode. *Nature* **400,** 649,651 (1999).
9. Afif, A. *et al.* Ammonia-fed fuel cells: a comprehensive review. *Renewable and Sustainable Energy Reviews* **60,** 822 –835 (2016).
10. Lewandowski, A. & Świderska Mocek, A. Ionic liquids as electrolytes for Li-ion batteries—An overview of electrochemical studies. *Journal of Power Sources* **194,** 601 –609 (2009).
11. Kirubakaran, A., Jain, S. & Nema, R. A review on fuel cell technologies and power electronic interface. *Renewable and Sustainable Energy Reviews* **13,** 2430 –2440 (2009).
12. Norby, T. *KJM3120 Inorganic Chemistry - Electrochemistry: Fuel Cells and Electrolysers* 2015.
13. Rexed, I., Lagergren, C. & Lindbergh, G. Effect of sulfur contaminants on {MCFC} performance. *International Journal of Hydrogen Energy* **39,** 12242 –12250 (2014).

14. Matsuzaki, Y. & Yasuda, I. The poisoning effect of sulfur-containing impurity gas on a {SOFC} anode: Part I. Dependence on temperature, time, and impurity concentration. *Solid State Ionics* **132.** Solid Oxide Fuel Cells dedicated to Prof. H. Tagawa, 261 –269 (2000).

15. Mert, S. O., Ozcelik, Z. & Dincer, I. Comparative assessment and optimization of fuel cells. *International Journal of Hydrogen Energy* **40.** Hydrogen and Fuel Cell Systems for Clean Energy Applications, 7835 –7845 (2015).

16. Kreuer, K.-D., Rabenau, A. & Weppner, W. Vehicle Mechanism, A New Model for the Interpretation of the Conductivity of Fast Proton Conductors. *Angewandte Chemie International Edition in English* **21,** 208–209 (1982).

17. Araki, T. *et al.* First-Principles Calculation and Proton Transfer in TiO2-Modified Porous Glass. *Journal of the American Ceramic Society* **93,** 127–131 (2010).

18. Norby, T. & Kofstad, P. Electrical Conductivity and Defect Structure of Y2O3 as a Function of Water Vapor Pressure. *Journal of the American Ceramic Society* **67,** 786–792 (12 1984).

19. Pornprasertsuk, R. *et al.* Proton conductivity of Y-doped BaZrO3: Pellets and thin films. *Solid State Sciences* **13,** 1429 –1437 (2011).

20. Haugsrud, R. & Norby, T. High-temperature proton conductivity in acceptor-doped LaNbO4. *Solid State Ionics* **177,** 1129 –1135 (2006).

21. Haugsrud, R. & Norby, T. Proton conduction in rare-earth ortho-niobates and ortho-tantalates. *Nature Materials* **5,** 193–196 (2006).

22. Kawakami, Y. & Miyayama, M. Proton Conducting Properties of Layered Metal Phosphate Hydrates. *Key Engineering Materials* **320,** 267–270 (2006).

23. Sumi, H., Nakano, Y., Fujishiro, Y. & Kasuga, T. Proton conduction of MO-P2O5 glasses (M = Zn, Ba) containing a large amount of water. *Solid State Sciences* **45,** 5 –8 (2015).

24. Choi, B.-K., Cho, Y.-H. & Lee, H.-K. Electrical conductivity and phase transition studies on K2SO4 crystals. *Journal of Physics and Chemistry of Solids* **54,** 197 –201 (1993).

25. Haile, S. M. *Solid Acid Based Fuel Cells* (California Institute of Technology, 2005).

26. Haile, S., Chisholm, C., Merle, R., Boysen, D. & Narayanan, S. *Solid acid electrolytes for electrochemical devices* US Patent 7,416,803. 2008.

27. Norby, T. *Defects and Transport in Crystalline Materials* 2015.

28. Tilley, R. J. D. *Understanding Solids: The Science of Materials* (John Wiley & Sons, Ltd, 2005).

29. Almond, D. & West, A. The activation entropy for transport in ionic conductors. *Solid State Ionics* **23,** 27 –35 (1987).

30. Kröger, F. & Vink, H. Relations between concentrations of imperfections in crystalline solids. *Solid State Physics* **3,** 307–435 (1956).

31. K. AMezawa H. Maekawa, Y. T. & Yamamoto, N. Protonic conduction and defect structures in Sr-doped LaPO4. *Solid State Ionics* **145,** 233–240 (2001).

32. Klement, R. & Uffelmann, R. Gitterkonstanten der Alkali-Erdalkaliphosphate. *Naturwissenschaften* **29,** 300–301 (1941).

33. Ohshita, H., Fujiwara, H. & Iwase, M. Electrical conductivities of M3P2O8 (M = Ca, Ba). *Steel Research* **62,** 427–429 (1991).

34. Norby, T. *Electrical Measurements* 2016.

35. Tribollet, M. E.O. B. *Electrochemical Impedance Spectroscopy* (John WIley & Sons Inc., 2008).

36. *Proton Conductors: Solids, Membranes and Gels - Materials and Devices* (ed Colomban, P.) (Cambridge University Press, Cambridge, Sept. 1992).

37. Archie, G. E. The Electrical Resistivity Log as an AId in Determining Some Reservoir Characteristics. *Transactions of the AIME* **146,** 54–62 (1 1942).

38. Pérez-Coll, D., Sánchez-López, E. & Mather, G. C. Influence of porosity on the bulk and grain-boundary electrical properties of Gd-doped ceria. *Solid State Ionics* **181,** 1033 –1042 (2010).

39. Mizusaki, J. *et al.* Simple mathematical model for the electrical conductivity of highly porous ceramics. *Journal of the American Ceramic Society* **79,** 109–113 (1 1996).

40. Fernelius, W. C., Loening, K. & Adams, R. M. Oxoacids and their salts. *Journal of Chemical Education* **50,** 123 (1973).

41. Yu, R. & Jonghe, L. C. D. Proton-Transfer Mechanism in LaPO4. *Journal of Physical Chemistry* **111,** 11003–11007 (2007).

42. A, L. On the Paddle -Wheel Mechanism for Cation Conduction in Lithium Sulphate. *Zeitschrift für Naturforschung A* **50,** 1067–1076 (11 1995).

43. Park, J.-H. Possible origin of the proton conduction mechanism of CsH2PO4 ccrystal at high temperatures. *Physical Review B* **69,** 054104 (2004).

44. Baranov, A. I. *et al.* Fast Proton Transport In Crystal With A Dynamically Disordered Hydrogen Bond Network. *Solid State Ionics* **36,** 279–282 (1989).

45. Klement, R. & Kresse, P. Die Polymorphie der Alkali-Erdalkaliphosphate, -arsenate und -vanadate. **310,** 53–68 (May 1961).

46. Masse, R. & Durif, A. Chemical Preparation and Crystal Structure Refinement of KBaPO4 Monophosphate. *Journal of Solid State Chemistry* **71,** 574–576 (1987).

47. Struck, C. W. & White, J. The unit cell dimensions and crystal structure of KBaPO4. *Acta Crystallographica* **15,** 290 (1961).

48. Nguyen, K., Haugsrud, R. & Norby, T. *Kevin sin master* MA thesis (University of Oslo, 2017).

49. Cooksley, B. & Taylor, H. Crystal structure of monoclinic Na Ca H Si O4. *Acta Crystallographica* **30,** p864–p867.

50. Krüger, G. & Wieker, W. Chemische Untersuchungen von Silicaten. XXXII. Untersuchungen im System BaO-SiO2-H2O. *Zeitschrift für anorganische und allgemeine Chemie* **340,** 277–293 (1965).

51. Fälth, L. & Annehed, H. The crystal structure of Ba2[SiO2(OH(2)]2. *Zeitschrift für Kristallographie* **169,** 219,225 (1984).

52. Chen, Q. & Zhu, T. Synthesis and characterization of single-crystalline BaH2SiO4 nanowires. *Chemical Physics Letters* **375,** 167–170 (2003).

53. Awakumov, G. V., Senna, M. & Kosova, N. V. *Soft Mechanochemical Synthesis. A Basis for New Chemical Technologies* (Springer US, 2001).

54. Apelblat, A. The vapour pressures of saturated aqueous solutions of potassium bromide, ammonium sulfate, copper(II) sulfate, iron(II) sulfate, and manganese(II) dichloride, at temperatures from 283 K to 308 K. *The Journal of Chemical Thermodynamics* **25,** 1513 –1520 (1993).

55. Norby, T. EMF method determination of conductivity contributions from protons and other foreign ions in oxides. *Solid State Ionics* **28,** 1586 –1591 (1988).

56. Manoun, B., Popović, L., Waal, D. D. & Verryn, S. M. C. Rietveld refinements of a new solid solution Ba(3-x)Srx(PO4)2. *Powder Diffraction* **18,** 122–127 (2003).

57. Chen, Q. *et al.* Properties and Crystal Structure of a Novel Silicate Single Crystal BaH2SiO4. *Chinese Journal of Inorganic Chemistry* **18,** 45–50 (2002).

58. Bacon, G. E. & Pease, R. S. A Neutron-Diffraction Study of the Ferroelectric Transition of Potassium Dihydrogen Phosphate. *Proceedings of the Royal Society of London A: Mathematical, Physical and Engineering Sciences* **230,** 359–381 (1955).

59. Podder, J., Ramalingom, S. & Kalkura, S. N. An Investigation on the Lattice Distortion in Urea and KCl Doped KDP Single Crystals by X-ray Diffraction Studies. *Crystal Research and Technology* **36,** 549–556 (2001).

60. Scherrer, B. *et al.* On Proton Conductivity in Porous and Dense Yttria Stabilized Zirconia at Low Temperature. *Advanced Functional Materials* **23,** 1957–1964 (15 2013).

61. Köck, E.-M., Kogler, M., Klötzer, B., Noisternig, M. F. & Penner, S. Structural and Electrochemical Properties of Physisorbed and Chemisorbed Water Layers on the Ceramic Oxides Y2O3, YSZ and ZrO2. *ASC Applied Materials & Interfaces* **8,** 16428–16443 (25 2016).

62. Stub, S., Vøllestad, E., Rørvik, P. M. & Norby, T. *On the interaction of grain boundaries and protonic surface transport in porous oxides* Submitted.

63. Kim, S. *et al.* On the conduction pathway for protons in nanocrystalline yttria-stabilized zirconia. *Phys. Chem. Chem. Phys.* **11,** 3035–3038 (17 2009).

64. Tande, C., Perez-Coll, D. & Mather, G. C. Surface proton conductivity of dense nanocrystalline YSZ. *J. Mater. Chem.* **22,** 11208–11213 (22 2012).

65. Chen, C.-T., Danel, C. E. & Kim, S. On the origin of the blocking effect of grain-boundaries on proton transport in yttrium-doped barium zirconates. *J. Mater. Chem.* **21,** 5435–5442 (14 2011).

66. Guo, X. & Maier, J. Grain Boundary Blocking Effect in Zirconia: A Schottky Barrier Analysis. *Journal of The Electrochemical Society* **148,** E121–E126 (3 2001).

67. Van den Berg, A. J. & Tuinstra, F. The space group and structure of α-K2SO4. *Acta Crystallographica Section B* **34,** 3177–3181 (1978).

68. Hwang, S. L. & Chen, I. W. Grain Size Control of Tetragonal Zirconia Polycrystals Using the Space Charge Concept. *Journal of the American Ceramic Society* **73,** 3269–3277 (1990).

69. Kliewer, K. L. & Koehler, J. S. Space Charge in Ionic Crystals. I. General Approach with Application to NaCl. *Phys. Rev.* **140,** A1226–A1240 (4A 1965).

70. Kjølseth, C. *et al.* Space charge theory applied to the grain boundary impedance of proton conducting BaZr0.9Y0.1O(3-d). *Solid State Ionics* **181,** 268 –275 (2010).

71. Thieme, C. & Rüssel, C. Thermal expansion behavior of SrSiO3 and Sr2SiO4 determined by high-temperature X-ray diffraction and dilatometry. *Journal of Materials Science* **50,** 5533–5539 (2015).

72. Rogers, S. E. & Ubbelohde, A. R. Melting and crystal structure. III. - low-melting acid sulphates. *Transactions of the Faraday Society* **46,** 1051–61 (1950).

73. Badot, J. & Colomban, P. RF-microwave dielectric relaxations and phase transitions in superionic protonic acid sulphates (selenates). *Solid State Ionics* **35,** 143 –149 (1989).

74. Bradley, R. S., Munro, D. C. & Ali, S. I. The migration of protons in solids at high pressures in the presence of an electric field. *Journal of Inorganic and Nuclear Chemistry* **32,** 2513–2520 (1970).

75. Perrino, C. T., Lan, B. & Alsdorf, R. Protonic Conduction in Potassium Dihydrogen Arsenate. *Inorganic Chemistry* **11,** 517–573 (1972).